UNIVERSITÀ DEGLI STUDI DI PERUGIA
Dottorato di Ricerca in Fisica
XVII Ciclo

Anti-proton Flux Detection and Indirect Search for Dark Matter with the AMS-02 Experiment

Dott. **Diego Caraffini**

Tutori:

Dott.sa **Bruna Bertucci**

Dott. **Paolo Zuccon**

Coordinatore del corso di dottorato:
Prof. **Pasquale Sodano**

A.A. 2003/04

Contents

Introduction

The existence a non-luminous matter in the Universe is a well established result of observational cosmology and astrophysics. Since the first half of the past century experiments have been performed to measure the relative contribution of Dark Matter (DM) to the total energy density of the Universe and a lot of theoretical effort was spent to solve the problem of its nature.

While the first issue has seemingly been settled by the recent results on Cosmic Microwave Background measurements, which indicate that DM contributes about 30% of the Universe energy density, the second is still not understood. In fact, the same measurements we just mentioned, forbid that baryonic matter accounts for more than 10% of the matter content of the Universe so the candidates to the role of DM must be found elsewhere.

The DM problem is today one of the most interesting research topics since it implies very close connections between supposedly distant fields of research, such as cosmology and particle physics, and hints to a more comprehensive picture of Nature. Indeed, almost all of the proposed DM models involve the introduction of new physics at the fundamental level, with extensions to the Standard Model of particle physics. At present the favoured candidate is the Lightest Supersimmetric Particle (LSP), that in a significant portion of Super Symmetry parameter space would meet the characteristics required to a good DM candidate.

According to theory, LSPs are stable particles, but they can annihilate producing in the final state ordinary particles, that sum to the fluxes of the various Cosmic Rays (CR) species constituting an excess with respect to the known sources; this excess is small, but it may be observable in the rare components of CR like anti-protons and positrons.

The AMS experiment has been designed to perform high precision measurements of the CR fluxes with the main goals of searching for anti-nuclei, as remnants of primordial anti-matter, and of measuring the faintest components of the cosmic flux, anti-protons, positrons and high energy photons. To fulfil the requirements of large acceptance, long exposure time and excellent particle identification necessary to achieve the intended results, AMS will operate in space as an attached payload of the International Space Station (ISS), being the first full featured particle physics experiment to operate in the Earth orbit.

In this work we performed a detailed Monte Carlo study with the aim to determine the sensitivity of the AMS in the discrimination of DM induced signals in the CR flux, focusing in the challenging anti-proton channel. The arguments addressed in the following chapters are organised along the following lines:

In the first chapter we introduce the fundamental concepts of the standard cosmological model and show how DM influences the evolution of the Universe in different ways depending on its relative abundance and nature. The indirect methods for the determination of DM density are also discussed and a review of the current limits from global fits of the cosmological parameters to recent observations is presented.

In the second chapter we point out the specific characteristics for a viable DM candidate and discuss some of the proposed ones. A particular attention is devoted to the hypothesis of the Lightest Supersimmetric Particle (LSP) that is at present favoured upon both theoretical and experimental considerations; the possible experimental techniques for the detection of the LSP are reviewed in the last part of the chapter together with some of the available experimental results on the subject.

The third chapter describes the apparatus of the AMS experiment, explaining its general conception, detailing the features of the various sub-systems and how they can be used to accurately measure the anti-proton. The inner TRACKER that, among other important tasks, provides the charge sign determination, is described with particular detail.

In the fourth chapter various aspects of the Monte Carlo (MC) used to produce the analysed data are described. In particular we explain the generating strategy adopted to keep the MC production process manageable both in terms of processing time and data storage. We also describe briefly the event reconstruction algorithm that was applied in the second step of the simulation. We conclude with a short description of the data samples we have analysed and of the guidelines of our analysis strategy.

In the fifth chapter we present the detail of the selection of anti-proton events in AMS using the complementary measurements of the sub-detectors described earlier. We first discuss the tracking performances and the selection criteria developed to reject poorly reconstructed tracks. Then we illustrate the use of combined velocity and rigidity measurements to further identify mis-reconstructed protons. Electron rejection based on Transition Radiation Detector, Electromagnetic Calorimeter and velocity measurements are subsequently discussed. We finally present the acceptances for signal and background.

In the sixth chapter we convolute the acceptances obtained with our analysis to the known CR fluxes of electrons, protons and anti-protons to obtain the rates we expect to observe in the absence of DM signal, as well as the projected accuracy of the $\bar{\mathrm{p}}$ flux measurement in the three years operating time of AMS. Then we evaluate the sensitivity that AMS would achieve with our analysis to LSP annihilation signals by comparing the null hypothesis to the signals predicted by a set of benchmark models.

Chapter 1

Physical Motivations

The first evidence of non-luminous matter pervading our Universe, dates to the 30's and comes from the observation that the velocity of galaxies in clusters is not compatible with the gravitational attraction produced only by the luminous matter. Since then, the existence of DM has been firmly established both by astrophysical and cosmological observations, and currently it is believed to contribute with a $\approx 30\%$ to the total mass-energy budget of our Universe.

In this chapter, we will review the observational evidences for DM and how this hints for new physics beyond the standard model of elementary particles.

We will first introduce the basic ideas of the standard cosmological model and the thermal history of the early Universe, discussing the indirect determination of the DM energy density and the existing limits on its baryonic nature, from global fits of the cosmological parameters to a variety of recent observations. We will then review the astrophysical measurements pointing to the existence of DM and allowing an estimate of its density profile in our galaxy.

1.1 The dynamical evolution of the Universe

At the large scales typical for cosmological theories, the dominating force is gravity, hence the natural choice is to describe the evolution of the Universe in the theoretical frame of the General Relativity, which establishes a strict relation between the distribution of energy and the features of space-time.

In this context, the dynamics of the Universe is governed by the Einstein's field equations: [1]

$$\mathcal{R}_{\mu\nu} - \frac{1}{2} g_{\mu\nu} R = 8\pi G T_{\mu\nu} + \Lambda g_{\mu\nu} \tag{1.1}$$

where $g_{\mu\nu}$ is the metric tensor and $\mathcal{R}_{\mu\nu}$ is the corresponding Ricci tensor; $T_{\mu\nu}$ represents the energy-momentum tensor, G the Newton gravitation constant, and Λ is the *cosmological constant*, on which we will come back later. The construction of a cosmological theory based on equation (1.1) requires to specify:

- the metric, i.e. to choose the geometry of the Universe from some *a priori* assumptions on its structure as a whole;

- the energy-momentum tensor, i.e. the different components — and their equation of state — which contribute to the energy budget of the Universe. In this regard, the Λ term can be seen as a contribution to the energy density with peculiar characteristics.

1.1.1 The Robertson-Walker metric

The common hypothesis of modern cosmological models is that the Universe is homogeneous and isotropic, if observed on a sufficiently large scale. This assumption, also known as the *Cosmological Principle*, reflects the experimental observations on isotropy and homogeneity, avoiding at the same time the necessity to grant our observation point with a special status with respect to all other locations in the Universe.

The most general way to describe the homogeneity and isotropy of the Universe is to introduce the *Robertson-Walker-Metric* [2,3,4], in which the invariant line element $\mathrm{d}s$ is given by

$$\mathrm{d}s^2 = \mathrm{d}t^2 - \mathrm{a}^2\left[\frac{\mathrm{d}r^2}{1-kr^2} + r^2(\mathrm{d}\theta^2 + \sin^2\theta\ \mathrm{d}\phi^2)\right] . \tag{1.2}$$

where a is the *scale factor* which determines the physical size of the Universe, r, θ and ϕ are the co-moving coordinates and k is the *curvature*, whose sign determines whether the spatial sections of the Universe are closed ($k > 0$), open ($k < 0$) or flat ($k = 0$). Throughout this chapter we used units such that $c = 1$.

The form of the metric implies a linear dependence of the relative velocity v_r between astrophysical objects and their distance d for a time-dependent scale factor $\mathrm{a} = \mathrm{a}(t)$:

$$v_r = \frac{\dot{a}}{a}d . \tag{1.3}$$

The experimental measurement of this relation in 1929 by E.Hubble [5] represented a major breakthrough in the understanding of the evolution of our Universe: not only it proved the validity of the cosmological principle but, for the first time, also pointed out the expansion of the Universe. Since then, the *Hubble* parameter, which defines the time dependent expansion rate of the Universe:

$$H(t) = \frac{\mathrm{d}\ln\mathrm{a}}{\mathrm{d}t} = \frac{\dot{\mathrm{a}}}{\mathrm{a}} , \tag{1.4}$$

is one of the fundamental cosmological parameters. The current present-day value of the *Hubble* parameter is $H_0 = 100h_0\mathrm{km/s\ Mpc}$,where $h_0 = 0.71^{+0.04}_{-0.03}$ is the so called "normalised" value of H_0 [6].

Related to the scale factor $\mathrm{a}(t)$, it is often more convenient to introduce a directly observable variable, the red-shift z, experimentally defined from the ratio between the emitted light frequency of a source and the one measured by a distant observer:

$$1 + z = \frac{\nu_e}{\nu_o} . \tag{1.5}$$

In the low distance limit, where the space can be safely considered flat, Hubble's law holds and the red-shift can be simply interpreted as the Doppler shift of the emitted radiation due to the recession velocity. At higher distances, the recession velocity definition starts to be fuzzy, curvature effects are not anymore negligible, and the relation between the red-shift and the scale factors at emission and observation time directly descends from the light ray condition :

$$\mathrm{d}s^2 = 0 \rightarrow \int_{t_e}^{t_o} \frac{\mathrm{d}t}{a(t)} = \int_{r_e}^{r_o} \frac{\mathrm{d}r^2}{1-kr^2} \ . \tag{1.6}$$

In both limits, it is found that:

$$1+z = \frac{\nu_e}{\nu_o} = \frac{a(t_e)}{a(t_0)} \ . \tag{1.7}$$

It is also customary to define the parameter q:

$$q = -\frac{\ddot{a}a}{\dot{a}^2} \ , \tag{1.8}$$

which is related to the variation of the expansion rate and is therefore called the deceleration parameter[1].

1.1.2 The Friedmann equations

With equation (1.2) in hand we can evaluate the actual form of the *Ricci*-Tensor and *Ricci*-scalar, that are

$$\begin{cases} \mathcal{R}_{00} = -3\frac{\ddot{\mathrm{a}}}{\mathrm{a}} \ , \\ \mathcal{R}_{ij} = -\left(\frac{\ddot{\mathrm{a}}}{\mathrm{a}} + 2H^2 + 2\frac{k}{\mathrm{a}^2}\right) g_{ij} \ , \end{cases} \tag{1.9}$$

$$\mathcal{R} = -6\left\{\frac{\ddot{\mathrm{a}}}{\mathrm{a}} + 2\left(\frac{\dot{\mathrm{a}}}{\mathrm{a}}\right)^2 + \frac{2k}{\mathrm{a}^2}\right\} \ ,$$

every other component being zero. Here the term H is the Expansion Rate (i.e. *Hubble* parameter).

The energy-momentum tensor is forced by the features of this metric, to be diagonal in order to respect homogeneity and to have equal spatial components to enforce isotropy; the simplest choice is to use the form valid for a perfect fluid:

$$T_{\mu\nu} = (\rho + p)^2 \, u_\mu \ , u_\nu - \rho g_{\mu\nu} \tag{1.10}$$

where u_μ is the four-velocity, ρ the rest density of energy, p the pressure of the matter-fluid and $g_{\mu\nu}$ the metric tensor. The state of the system is completely determined if we assign an equation of state for the fluid that in general can be written as

$$p = w\rho \ , \tag{1.11}$$

where the actual value of w depends on the features of fluid filling the Universe itself. In this context, non relativistic matter will be characterised by a $w = 0$ value, i.e. as a pressure-less gas, while radiation will be described by a $w = 1/3$.

Using the Robertson-Walker metric (1.2) and the perfect fluid energy-momentum tensor (1.10) in the equations of field (1.1), we obtain the *Friedmann-Lemaître* equations, which describe the dynamical evolution of the Universe as [7, 8, 9]:

$$H^2 \equiv \left(\frac{\dot{\mathrm{a}}}{\mathrm{a}}\right)^2 = \frac{8\pi G}{3}\rho - \frac{k}{\mathrm{a}^2} + \frac{\Lambda}{3}, \tag{1.12}$$

---

[1] At the time of definition it was accepted that the expansion would not be accelerated; hence the name “deceleration” parameter and the fact that a negative value means accelerating expansion and vice-versa.

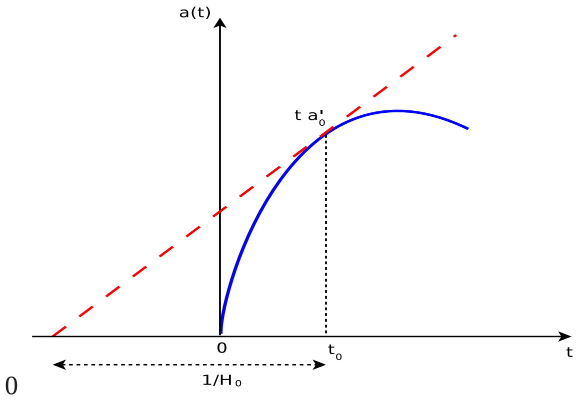

Figure 1.1: *Evolution of* a *with time. Since* $\ddot{\mathrm{a}}$ *must be negative* $\mathrm{a}(t)$ *must intersect the time axis; in addition must be* $t_0 < 1/H_0$.

and

$$\frac{\ddot{\mathrm{a}}}{\mathrm{a}} = -\frac{4\pi G}{3}(\rho + 3p) + \frac{\Lambda}{3}. \tag{1.13}$$

A third equation can be obtained applying the third law of thermodynamics to the perfect fluid expanding adiabatically with the Universe

$$\dot{\rho} = -3\frac{\dot{\mathrm{a}}}{\mathrm{a}}(\rho + p)\ , \tag{1.14}$$

but this is not independent of Eqs. (1.12),(1.13) from which can also be derived.

1.1.3 Cosmological models with Λ=0

If we neglect the cosmological constant Λ, Eqs. (1.12),(1.13) have a simple physical interpretation even in a Newtonian approach. Since the Universe is expanding, as we know observationally, and the $(\rho{+}3p)$ term is positive by definition both for matter and radiation, it follows from equation (1.13) that $\dot{\mathrm{a}}$ must decrease in time as a consequence of the attractive nature of gravity. Moreover, whatever the assumed curvature k, as $t \to 0$ the scale factor tends to vanish, as it is sketched in figure 1.1. In equation (1.12) we can interpret the term $-k/\mathrm{a}^2$ as a “total energy”, so that $(\dot{\mathrm{a}}/\mathrm{a})^2$ would be a “kinetic term” and $-8\pi G\rho/3$ a “potential”. In this classical analogy we see that the evolution of the Universe is governed by the competing effects of the kinetic and potential terms and the sign of their sum determines if the Universe will eventually collapse ($k = 1$) or keep on expanding ($k = 0, -1$); we have recovered the meaning of the curvature factor k of equation (1.2).

While the fate of the Universe is globally determined by its constant curvature, the Hubble parameter and the energy density depend on time or equivalently on the scale factor a. For a detailed description of the dynamical evolution of the Universe is therefore mandatory to account for the different contributions, radiation and/or matter, which build up the energy density, as well as of their different scaling with a. From the equation of state (1.11) and (1.14) it can be easily assessed that, for a given component, we have $\rho \propto \mathrm{a}^{-3(1+w)}$, i.e. $\rho_m \propto \mathrm{a}^{-3}$ and $\rho_{rad} \propto \mathrm{a}^{-4}$ for matter and radiation respectively. To estimate the relative importance of radiation and matter at a given time in the history of the Universe, is therefore customary to refer their values in the Friedman equation to their present day value $\rho_{0,m}, \rho_{0,rad}$:

$$H^2 = \frac{8\pi G}{3}\left[\rho_{0,m}\left(\frac{\mathrm{a}_0}{\mathrm{a}}\right)^3 + \rho_{0,rad}\left(\frac{\mathrm{a}_0}{\mathrm{a}}\right)^4\right] - \frac{k}{\mathrm{a}^2}\ , \tag{1.15}$$

where a_0 corresponds to the present day scale factor.

From the above expression, the main features of the evolution can be easily seen: in the early phase of the Universe ($t \to 0, \mathrm{a} \to 0$) the radiation term clearly dominates over the curvature and matter contributions to the expansion. In the *radiation era* the time dependence of the scale factor and of the expansion rate can be expressed by $\mathrm{a}(t) = t$ and $H(t) = 1/2t$ respectively. As the physical radius increases, matter takes over radiation. The condition which determines the scale factor a_{eq} (or equivalently the red-shift z_{eq}) of the Universe at the matter-radiation equality is simply found as:

$$\frac{\mathrm{a}_{eq}}{\mathrm{a}_0} = \frac{\rho_{0,rad}}{\rho_{0,mat}}\ ;\ 1 + z_{eq} = \frac{\rho_{0,mat}}{\rho_{0,rad}}\ . \tag{1.16}$$

During the *matter era* the time dependence of the scale factor and of the expansion rate can be expressed by $\mathrm{a}(t) = t^{2/3}$ and $H(t) = 2/3t$ respectively. Finally, the curvature term takes over and, depending on its actual value, we get a matter Universe monotonically expanding at an ever-decreasing rate ($k = 0$, the Einstein-de Sitter model), an *empty* expanding Universe ($k = -1$, the Milne model) or an *oscillating* Universe ($k = +1$).

1.1.4 Cosmological models with $\Lambda \neq 0$

Different scenarios in the Universe evolution, are opened by the introduction of the cosmological constant term. In the perfect fluid approximation, the constant Λ in equation (1.1) corresponds to the introduction of an energy density constant in time that is associated with a pressure of equal magnitude but opposite sign:

$$\rho_\Lambda = \frac{\Lambda}{8\pi G}\ , \tag{1.17}$$

$$p_\Lambda = -\rho_\Lambda = -\frac{\Lambda}{8\pi G}\ . \tag{1.18}$$

Originally *Einstein* introduced this term because at the time it was strongly believed that the Universe should be static, but without the Λ term equation (1.1) cannot account for such an hypothesis since it would be an instable solution; on the other hand if $\Lambda > 0$ then the associated pressure would be negative and we could consider it as a kind of “repulsive ” gravity, independent of space-time, that would enforce a static Universe. After Hubble showed that the Universe is expanding, the cosmological constant was rejected. Nowadays Λ has a new physical interpretation after the quantum field theories, which define vacuum as the state with lowest energy, but do not require this value to be zero[2]. Such non-zero vacuum energy can mimic the effect of a cosmological constant such that $\rho_v = \Lambda \times 8\pi G$.

Including the ρ_Λ term in equation (1.15):

$$H^2 = \frac{8\pi G}{3}\left[\rho_{0,m}\left(\frac{\mathrm{a}_0}{\mathrm{a}}\right)^3 + \rho_{0,rad}\left(\frac{\mathrm{a}_0}{\mathrm{a}}\right)^4 + \rho_\Lambda\right] - \frac{k}{\mathrm{a}^2}\ . \tag{1.19}$$

---

[2] It should be noticed that in principle this vacuum energy needs not have $w = -1$ in its equation of state, but for the moment we will stick to that value for simplicity.

It is easy to see that the presence of vacuum energy can by itself change the Universe final evolution.

In the event that $\Lambda < 0$ then, whatever is the value of the curvature of space-time, the final outcome is that the Universe will re-collapse.

On the other hand, a positive contribution of Λ can lead the Universe to quite different evolutions depending on ρ_Λ and k:

- k=0, w=-1 : we get a vacuum energy dominated Universe. The expansion rate becomes a constant $H = \sqrt{\Lambda/3}$ and the physical radius scales exponentially with time as $\mathrm{a}(t) \propto e^{\sqrt{\Lambda/3}}$.
- k=+1, $\Lambda = \Lambda_c$: by asking simultaneously $\dot{\mathrm{a}} = 0, \ddot{\mathrm{a}} = 0$ in equations (1.12), (1.13) can be found the critical Λ value that allows a static Universe at a fixed physical radius R_c. This is the original Einstein cosmological model, discarded by experimental evidence. Other solutions, the Eddington-Lemaitre models, are allowed for $R < R_c$ or $R > R_c$ which respectively tend to the Einstein model or depart from it.
- k=+1, $\Lambda > \Lambda_c$ we get again a vacuum energy dominated Universe.
- k=+1, $\Lambda < \Lambda_c$ we get either oscillating ($0 < \mathrm{a} < \mathrm{a}_{max}$) or bouncing ($\mathrm{a}_{min} < \mathrm{a} < \infty$) models for our Universe.

1.1.5 Cosmological parameters

A compact form of the Friedmann equations which is commonly used to compare cosmological models with observations, is based on the rescaling of all energy densities to the present day value of the *critical density*, ρ_c, defined as the total energy density which would correspond to a *flat* Universe:

$$\rho_c = \frac{3H_0^2}{8\pi G} \approx 9.5 \times 10^{-30}\,\mathrm{g/cm^3}\ . \tag{1.20}$$

The cosmological densities of radiation, matter and vacuum energy are then defined as:

$$\Omega_{rad} = \frac{\rho_{rad}}{\rho_c}\ \ ;\Omega_{mat} = \frac{\rho_{mat}}{\rho_c}\ \ ;\Omega_\Lambda = \frac{\rho_\Lambda}{\rho_c}\ ,$$

and the Friedmann equations (1.12),(1.13) are rewritten as:

$$\frac{k}{\mathrm{a}^2} = H^2\left(\Omega_{mat} + \Omega_{rad} + \Omega_\Lambda - 1\right) = H^2(\Omega_{tot} - 1)\ , \tag{1.21}$$

$$q = \frac{1}{2}\Omega_{mat} + \Omega_{rad} + \frac{(1+3w)}{2}\Omega_\Lambda\ , \tag{1.22}$$

where q is the deceleration parameter and we left a generic w in the contribution of vacuum energy to acceleration, since its value depends in general on the nature of the vacuum energy source. The interesting point is that for $w > -1/3$ the possibility of an accelerated expansion exists and actually there are observational evidences pointing in that direction as we will show shortly.

When referring (1.21) to the present day values of cosmological densities the analogous of (1.15) can be obtained as:

$$H^2 = H_0^2\left[\Omega_{0,mat}\left(\frac{\mathrm{a}_0}{\mathrm{a}}\right)^3 + \Omega_{0,rad}\left(\frac{\mathrm{a}_0}{\mathrm{a}}\right)^4 + \Omega_{0,v} + \Omega_{0,k}\left(\frac{\mathrm{a}_0}{\mathrm{a}}\right)^2\right]. \tag{1.23}$$

1.2 Thermal evolution of the Universe

In the previous sections we have seen how the dynamical evolution of the Universe depends both on the geometry of the underlying space-time structure and on the nature and abundance of the energy density components. To fully define our cosmological model, we have also to enter in the realm of particle physics, to identify the particles constituting the matter, radiation or vacuum energy components, and the fields governing their interactions.

Given the relatively small size and high density of the primeval Universe, we are led to suppose that it evolved maintaining thermal equilibrium, though this may be true only for a limited period of time.

In this condition all the existing particle species interact very fast with each other due to the high temperature (mean energy) of the system. In order to maintain the thermal equilibrium it is necessary that

$$\Gamma_{int} \gg H \tag{1.24}$$

that is to say: the interaction rate Γ_{int} of each particle is large with respect to the Universe expansion rate whose effect is to increase the average distance between particles; this in turn affects the interaction rate since it takes more time for a particle to travel to its neighbour, but while equation (1.24) holds this increase is not appreciable. As soon as equation (1.24) is not met, the considered particle is not able to follow the Universe thermal evolution, just because it cannot interact with other particles fast enough to thermalise; in this case we say that the particle has “decoupled” and will evolve independently.

The overall description of the early Universe is then based on a thermodynamical approach, where different epochs are characterised by different species whose thermal equilibrium is kept by the appropriate elementary interactions.

Table 1.1 summarises the successive phases the Universe went through: the first table entry, for which no involved physics are reported, is also called the Planck era. We do not know what conditions were like during the Planck Era. This lasted from the initial singularity until 10^{-43} seconds after the Big Bang. That moment is referred to as Planck time. At that time the Universe’s size was about 10^{-33} cm across; this is called the Planck length. At this time the quantum wavelength of the universe was larger than the size of the universe itself. The universe has complete symmetry: all four forces we know today were unified. We do not know what happened before this time, because our knowledge of physics breaks down at this point. Our present-day formulation of physics fails in principle to be able to explain what was going on. A quantum theory of gravity is required if we can proceed any farther back toward the beginning.

At the Planck time, symmetry breaks and gravity becomes a distinct force. The other forces are still unified as the GUT (Grand Unified Theory) force. This is the start of the GUT era. Here we have the beginning of Quantum theory and classical general relativity.

1.2.1 Equilibrium Thermodynamics

As long as thermal equilibrium holds it makes sense to define a temperature of the Universe (T) and a phase space equilibrium distribution for the particles according the

Time (s)	Energy (GeV)	Epoque	Involved physics
$< 10^{-43}$	$< 10^{19}$	Quantum gravity	Unknown physics.
$10^{-43} \div 10^{-35}$	$10^{19} - 10^{15}$	GUT	Three interactions unified. Gravitation decoupled.
10^{-34}	10^{14}	GUT phase transition	Grand Unifying theories. BaryonSymmetry. $R \sim 10^{-23}$cm
$10^{-34} \div 10^{-32}$	$10^{14} \div 10^{12}$	Inflation	$R \sim 10^{20}$ cm
10^{-32}			Violation of Matter Antimatter Symmetry. CPViolation.
$10^{-32} \div 10^{-11}$		Normal expansion	Quarks/leptons plasma in thermal equilibrium.
10^{-11}	100	Electroweak phase transition	Standard Model of particle physics. EW interaction.
$10^{-11} \div 10^{-6}$	1	Baryogenesis	$q\bar{q}, ll$ annihilation $n_b/n_\gamma \sim 10^{-10}$
10^{-4}	0.1	QCD phase transition Decoupling of $\nu, \bar{\nu}$	Confinement of quarks into meson and baryons
1	0.001	Nucleosynthesis	Production of light nuclei. Freezeout of e^+e^-. Reheating of photons.
100.000 year		t_{eq}	Universe becomes matter dominated

Table 1.1: *An overview of the evolution stages of the Universe.*

Bose-Einstein or Fermi-Dirac description. The number and energy density (n_i and ρ_i) for a given species are then given in the relativistic limit ($m_i \ll T$):

$$n_i = \begin{cases} 0.122 g_i T^3 & bosons \\ 0.122 \cdot (\frac{3}{4}) g_i T^3 & fermions \end{cases} , \tag{1.25}$$

$$\rho_i = \begin{cases} 0.329 g_i T^3 & bosons \\ 0.329 \cdot (\frac{3}{4}) g_i T^4 & fermions \end{cases} , \tag{1.26}$$

while for non-relativistic matter ($m_i \gg T$)

$$n_i = g_i \left(\frac{m_I t}{2\pi} \right)^{\frac{3}{2}} exp[-(m_i - \mu_i)/T] , \tag{1.27}$$

$$\rho_i = m_i n_i , \tag{1.28}$$

where g_i stands for the number of degrees of freedom for the i^{th} particle.

From the above expressions, we see that the actual contribution to the energy density at a given T is exponentially suppressed for non-relativistic matter: it is a good approximation to neglect them when summing over all species to obtain the total energy density of the early Universe:

$$\rho = \frac{\pi^2}{30} g_*(T) T^4 , \tag{1.29}$$

where $g_*(T)$ is the total number of degrees of freedom at the temperature T obtained as a weighted sum over all the particle species:

$$g_* = \sum_{i=bosons} g_i \left(\frac{T_i}{T} \right)^4 + \frac{7}{8} \sum_{j=fermions} g_j \left(\frac{T_j}{T} \right)^4 . \tag{1.30}$$

Here the $T_{i,j}$ terms are introduced to account for relativistic particles which are not anymore in thermal equilibrium with the rest of the Universe but may still have a thermal distribution corresponding to a different temperature, as it happens for neutrinos after decoupling.

A key point in the thermal evolution of the Universe is the entropy conservation during expansion: equation (1.14) allows to derive for the total entropy in a volume a^3:

$$S = \mathrm{a}^3 \frac{\rho + p}{T} = const . \tag{1.31}$$

The entropy density can be then defined as:

$$s = \frac{S}{\mathrm{a}^3} = \frac{2\pi^2}{45} g_{*s}(T) T^3 , \tag{1.32}$$

where the g_{*s} factor is defined as in equation (1.30)

$$g_{*S} = \sum_{i=bosons} g_i \left(\frac{T_i}{T} \right)^3 + \frac{7}{8} \sum_{j=fermions} g_j \left(\frac{T_j}{T} \right)^3 . \tag{1.33}$$

and the conservation of entropy for particles in thermal equilibrium can be rewritten as:

$$g_{*s} \cdot [\mathrm{a}T]^3 = const \tag{1.34}$$

As long as we are not in the proximity of a phase transition or a particle decoupling g_{*S} is constant and this, establishes a relation between temperature and scale factor,

$$T \propto g_{*S}^{\frac{1}{3}} \, \mathrm{a}^{-1} \ . \tag{1.35}$$

so that the temperature will consistently decrease under adiabatic evolution in an expanding Universe, but it will decrease more slowly when the effective number of relativistic degrees of freedom is diminished.

In fact, depending on the temperature, we expect to have important changes in the number of species which contribute to the energy and entropy density of the early Universe.

In the framework of the EW Standard Model, all fermions, gauge and Higgs bosons are to be accounted at a $T \sim \mathcal{O}(\mathrm{TeV})$, resulting in a $g_* = 106.75$, which drastically reduces to $g_* = 51.25 \div 17.25$ at $T \sim \mathcal{O}(200 \div 400\,\mathrm{MeV})$ due to the quark-gluon confinement in hadrons and π's decoupling. The last change in $g_*, g_{*,s}$ happens at $T \sim \mathcal{O}(\mathrm{MeV})$, when the annihilation process $\mathrm{e}^+\mathrm{e}^- \rightarrow \gamma\gamma$ becomes dominant as electrons and positrons are no more relativistic

The thermodynamical description of the expanding Universe ends with the last interactions between photons and matter in the *recombination* phase, when neutral atoms were formed by nuclei and electrons. Photons are not scattered anymore by free electrons and the Universe becomes transparent.

After this epoch, the total number of non-relativistic particles is frozen and its contribution the energy density will scale with the physical radius of the Universe according to the matter equation of state $\rho \propto \mathrm{a}^{-3}$.

However, for the relativistic species left over — i.e. photons and massless neutrinos — the number and energy density will maintain the thermal equilibrium distribution, with an effective temperature scaling with the physical radius as $T \propto \mathrm{a}^{-1}$.The interesting point is that knowing the temperature and the spectrum it is easy to evaluate the contribution of radiation to the energy density of the Universe.

This was pointed out in 1948 by *Gamow, Alpher, Herman*, who estimated the residual temperature for γ's to be about 5 K [10, 11]. The prediction was confirmed in 1965 by *Penzias* and *Wilson* who observed an isotropic Black Body photon spectrum [12], whose temperature is nowadays measured to be 2.725 ± 0.001 K. This spectrum is commonly referred to as the Cosmic Microwave Background (CMB) and is considered one of the most important confirmations of the Big Bang theory; using the experimental value for T and the black body energy density $\varepsilon = \alpha T^4$, we find that $\Omega_\gamma = (4.9 \pm 0.5) \times 10^{-5}$.

1.2.2 Nucleosynthesis

The prediction of CMB originated in the context of the work on the theory of Big Bang Nucleosyntesis, that is an attempt to predict / explain the observed abundances of light nuclei in the Universe. The Big Bang Nucleosyntesis (BBN) theory is based on the inclusion of an extended nuclear network into an homogeneous and isotropic cosmology, such as that described in the previous sections. The synthesis was affected by conditions in the early Universe at temperatures $T \lesssim 1$ MeV. At higher temperature the weak interactions are still active and the processes

$$\begin{array}{rcl} n + \mathrm{e}^+ & \leftrightarrow & \mathrm{p} + \bar{\nu}_\mathrm{e} \\ n + \nu_\mathrm{e} & \leftrightarrow & \mathrm{p} + \mathrm{e}^- \\ n & \leftrightarrow & \mathrm{p} + \mathrm{e}^- + \bar{\nu}_\mathrm{e} \end{array} \tag{1.36}$$

keep the thermal equilibrium and fix the neutron to proton number density ratio to be $n/\mathrm{p} \simeq e^{-\Delta m/T}$, where Δm is the neutron-proton mass difference ($n/\mathrm{p} \sim 1$).

As the temperature lowers, the weak interaction rate, $\Gamma_{wk} \sim G_F^2 T^5$, falls below the Hubble expansion rate $H \sim \sqrt{g_* G_N} T^2$, and the reactions in equation (1.36) are no longer in equilibrium. At this point $T \sim (g_* G_N / G_F^4)^{1/6} \sim 1\,\mathrm{MeV}$ and we have $(n/\mathrm{p}) \simeq 1/6$. After freezeout the neutrons were free to β decay so the neutron fraction dropped to $\approx 1/7$ by the time nuclear reactions began. The mentioned delay is due to the fact that the nucleosynthesis chain begins with the formation of deuterium in the process:

$$\mathrm{p} + n \leftrightarrow \mathrm{D} + \gamma. \tag{1.37}$$

Photodissociation by the high number density of photons inhibits deuterium production until T drops well below the binding energy of deuterium, $\Delta D = 2.23\,\mathrm{MeV}$. At that temperature, a substantial fraction of photons coming from the tail of the black body spectrum is energetic enough to photo-dissociate the newborn nuclei. When the condition:

$$\eta^{-1} \cdot e^{\Delta D/T} < 1 \tag{1.38}$$

is met at $T \simeq 0.1\,\mathrm{MeV}$, nuclei begin to form without being immediately photodissociated. Here $\eta = n_B/n_\gamma$ is the number density of baryons relative to that of photons, and it is the only free parameter of the theory, since the processes cross-sections are well known and introduced “by hand” in the calculation.

When nucleosynthesis begins, nearly all the surviving neutrons end up bound in the most stable light element $^4\mathrm{He}$, because of the absence of stable nuclei with mass number 5 or 8, which disallows nucleon capture by $^4\mathrm{He}$ or processes involving two $^4\mathrm{He}$ nuclei, while $T + {}^4\mathrm{He} \leftrightarrow \gamma + {}^7\mathrm{Li}$ and $^3\mathrm{He} + {}^4\mathrm{He} \leftrightarrow \gamma + {}^7\mathrm{Be}$ are suppressed by their high Coulomb barriers.

The primordial mass fraction of $^4\mathrm{He}$, conventionally referred to as Y_p , can be estimated by the simple counting argument

$$Y_\mathrm{p} = \frac{2(n/\mathrm{p})}{1 + n/\mathrm{p}} \simeq 0.25\ . \tag{1.39}$$

This is quite independent of actual nuclear reaction rates, which are much more involved in the calculation of the abundances of the other leftover light nuclei such as D, $^3\mathrm{He}$ and $^7\mathrm{Li}$. The abundances, calculated using the Wagoner code[3] [13, 14], are shown in figure 1.2 as a function of $\eta_{10} = \eta \cdot 10^{10}$. The $^4\mathrm{He}$ curve includes small corrections due various effects [15, 16, 17]; the range reflects primarily the 1σ uncertainty in the neutron lifetime. The spread in the curves for D, $^3\mathrm{He}$ and $^7\mathrm{Li}$ corresponds to the 1σ uncertainties in nuclear cross sections.

All the light element abundances can be explained with η_{10} in the range $3.4 \div 6.9$(95% C.L.). Since the photon number density is known to be $m_\gamma = 410.5\,\mathrm{cm}^{-3}$, this is equivalent, to say that the allowed range for the baryon mass density today, $\rho_B = (2.3 \div 4.7) \times 10^{-31}\,\mathrm{g\,cm}^{-3}$, or as the baryonic fraction of the critical density:

---

[3] Publicly available at http://www-thphys.physics.ox.ac.uk/users/SubirSarkar/bbn.html

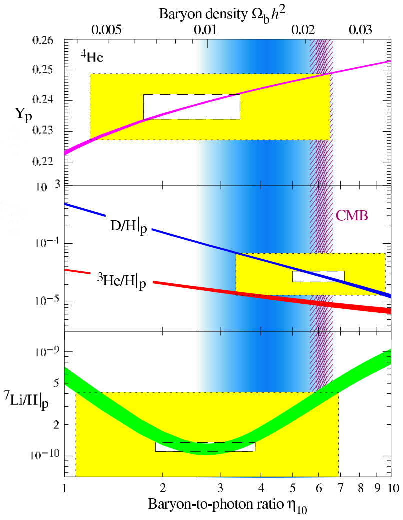

Figure 1.2: *The abundances of ^4He, D, ^3He and ^7Li as predicted by the standard model of bigbang nucleosynthesis. Boxes indicate the observed light element abundances (smaller boxes: 2σ statistical errors; larger boxes: 2σ statistical and systematic errors added in quadrature). The narrow vertical band indicates the CMB measure of the cosmic baryon density.*

$\Omega_{bar} = \rho_B/\rho_{crit} \simeq \eta_{10} h^{-2}/274 = (0.012 \div 0.025) h^{-2}$, where h is the normalised Hubble parameter.

1.2.3 The neutrino decoupling

As pointed out in the previous section, just before the nucleosynthesis of the lightest elements in the early Universe, weak interactions were too slow to keep neutrinos in thermal equilibrium with the plasma via the processes (1.36), so they decoupled. We can estimate the temperature at which decoupling occurred from the weak interaction cross section, $\sigma_W \simeq G_F^2 T^2$ at finite temperature T, where $G_F = 1.2 \cdot 10^5$ GeV^2 is the Fermi constant. The neutrino interaction rate, via W boson exchange in $n + \nu \leftrightarrow \mathrm{p} + \mathrm{e}^-$ and $p + \bar{\nu} \leftrightarrow n + \mathrm{e}^+$, can be written as

$$\Gamma_\nu = n_\nu \left\langle \sigma_W |v| \right\rangle \simeq G_F^2 T^5 \;, \tag{1.40}$$

while the rate of expansion of the Universe at that time ($g_* = 10.75$) was $H \simeq 5.4 T^2/M_P$, where $M_P = 1.22 \cdot 10^{19}$ GeV is the Planck mass. Neutrinos decouple when their interaction rate is slower than the Universe expansion, $\Gamma_\nu \leq H$ or, equivalently, at $T_{\nu\text{-}dec} \leq 0.8$ MeV. Below this temperature, neutrinos are no longer in thermal equilibrium with the rest of the plasma, and their temperature continues to decay inversely proportional to the scale factor of the Universe. After neutrinos decoupled $\mathrm{e}^+\mathrm{e}^-$ annihilation began, leading to an increase of the photon temperature relative to the decoupled neutrinos, usually referred to as re-heating, and as a consequence the temperature of the neutrino background is lower than that of the CMB. The difference can be computed considering that at temperatures above the mass of the electron, $T > m_e = 0.511$ MeV, and below 0.8 MeV, the only particle species contributing to the entropy of the Universe are the photons ($g_\gamma = 2$) and the electron-positron pairs

($g_{e^{\pm}} = 4 \times 7/8$). From equation (1.33) we obtain a total number of degrees of freedom $g_* = 11/2$, while at temperatures $T < m_e$, only photons contribute to the entropy of the Universe, with just $g_* = 2$ degrees of freedom. Therefore, from the conservation of entropy, we find that the ratio of T_γ and T_ν today must be

$$\frac{T_\gamma}{T_\nu} = \left(\frac{11}{4}\right)^{1/3} = 1.401 \longrightarrow T_\nu = 1.945 \text{ K} \tag{1.41}$$

where the experimental value $T_{CMB} = 2.725$ K has been used.

With the knowledge of T_ν, we can compute the energy density associated to the relic ν Fermi-Dirac spectrum to be $\Omega_\nu = 0.68\Omega_\gamma$ considering three species of neutrinos. These considerations apply to the case of massless neutrinos.

1.2.4 Photon decoupling

The last stage of the Universe thermal history is formation of neutral nuclei followed by the decoupling of photons from the plasma.

When the temperature of the Universe is such that only a small fraction of photons have energy greater than $\mathrm{E}_{ion} = 13.6\,\mathrm{eV}$, the hydrogen ionisation energy, recombination may begin; the actual ionisation fraction of electrons in equilibrium with the plasma at a certain temperature X_e^{eq} is given by the relation1.2.3:

$$\frac{1 - X_e^{eq}}{X_e^{eq}} = \frac{4\sqrt{2}\zeta(3)}{\sqrt{\pi}}\eta\left(\frac{T}{m_e}\right)^{3/2} e^{\mathrm{E}_{ion}/T} \,, \tag{1.42}$$

where η is the baryontophoton ratio from nucleosynthesis.

Defining recombination as the time at which $X_e^{eq} \equiv 0.1$, one finds that the recombination temperature is $T_{rec} = 0.3\,\mathrm{eV}/\mathrm{E}_{ion}$, for $\eta_1 0 \simeq 5.2$. Comparing with the present temperature of the microwave background, we deduce the corresponding red-shift at recombination, $(1 + z_{rec}) \simeq 1270$. The process that keeps γs in equilibrium with the plasma of electrons and baryons is elastic Thomson scattering, whose cross section is:

$$\sigma_T = \frac{8\pi\alpha^2}{3m_e^2} = 6.65 \times 10^{-25}\ \mathrm{cm}^2 = 0.665\ \mathrm{b} \,, \tag{1.43}$$

where $\alpha = 1/137.036$ is the dimensionless electromagnetic coupling constant. The mean free path of photons λ_γ in such a plasma can be estimated from the photon interaction rate, $\lambda_\gamma^{-1} \sim \Gamma_\gamma = n_e\sigma_T$. We can estimate the moment at which Thomson scattering can't keep up with the expansion of the Universe by the usual relation $\Gamma_\gamma = H$ at photon decoupling. Using $n_e = X_e\eta n_\gamma$, one can compute the decoupling temperature as $T_{dec} = 0.26\,\mathrm{eV}$, and the corresponding red-shift as $(1 + z_{dec}) \simeq 1100$. This red-shift defines the so called last scattering surface, when photons last scattered off protons and electrons and traveled freely ever since forming the Cosmic Microwave Background.

1.3 Inflation

The standard cosmology, as discussed so far, is not fully satisfying due to some open questions, the most prominent of whom is called the "horizon problem". This arises because there is only a finite amount of time since the Big Bang and a photon can therefore travel only a finite distance in the Universe life-time, thus defining an horizon:

$$\Delta r = \int_{t_{BB}}^{t_0} \frac{\mathrm{d}t}{\mathrm{a}(t)} \ . \tag{1.44}$$

However, if we evaluate the horizon at the time of recombination, we find that it subtends a $\sim 1^\circ$ angle, so that exist different portions of the sky that are not within the horizon of each other and cannot be causally connected. If such two position are not in causal connection, their initial conditions should be independent from each other, nonetheless they have temperature fluctuations of relative amplitude within $\frac{\delta T}{T} \sim 10^{-5}$.

Connected to this is the “flatness problem”, linked to the fact that Friedman equations imply an Universe that is flatter and flatter as we move towards the initial singularity (larger red-shift) as we can see re-expressing Ω in terms of Ω_0 and the red-shift z:

$$\Omega = \frac{\Omega_0(1+z)}{\Omega_0 z + 1} \ . \tag{1.45}$$

Both issues would require a severe fine tuning for the initial conditions of Big Bang cosmology.

Such problems can be overcome if the Universe goes through a phase of non adiabatic exponential expansion called inflation; in this hypothesis the horizon evaluated with equation (1.44) would be far greater, insuring causal and hence thermal contact between all points of the observable Universe at some time just after the temperature falls below the Planck scale; also, the density parameter ω would be driven towards 1.

To produce inflation is common practice to introduce a scalar field ϕ, called *inflaton*, that undergoes a symmetry breaking. If the associated phase transition is such that the field evolves slowly from the symmetric state to the global minimum of the potential, the Universe may have been dominated by vacuum energy, associated with the potential near $\phi \approx 0$. During this slow roll period, the expansion would be of the exponential type described in section 1.1.4. As the field reaches the minimum of the potential, it begins to oscillate, energy is released and this restores the conditions for an hot thermal Universe where radiation dominates and the expansion is no more exponential [18, 19]. This scheme has also the advantage that allows us to predict the CMB anisotropies features as function of the cosmological parameters; in fact due to quantum fluctuations in the scalar field inflation ends at different times in different places and the value of the induced δ_ρ/ρ is related to $\delta T/T$ [18, 20].

1.4 Structure Formation

Despite cosmology is based on the assumption that the Universe is homogeneous on a sufficiently large scale, we face the necessity to account for the actual presence of structures at smaller ones.

The simplest model for the generation of cosmological structures is gravitational instability acting on some small initial fluctuations, whose origin can be explained by the theory of inflation.

As mentioned in section 1.3, such fluctuations should be detected as small CMB anisotropies; in fact such anisotropies were discovered by the COBE satellite in 1992 and they amount to about one part in 10^5.

Defining the density contrast as [18, 21]

$$\delta(\widehat{x},\mathrm{a}) \equiv \frac{\rho(\widehat{x},\mathrm{a})-\bar{\rho}(\mathrm{a})}{\bar{\rho}(\mathrm{a})} = \int \mathrm{d}^3\widehat{k}\delta_k(\mathrm{a})e^{i\widehat{k}\cdot\widehat{x}} \, , \tag{1.46}$$

where $\bar{\rho}(\mathrm{a}) = \rho_0\mathrm{a}^{-3}$ is the average cosmic density, we need a theory that develops a density contrast of amplitude $\delta \sim 10^{-5}$ at the last scattering surface ($z = 1100$) and then lets it grow up to the order of $\delta \sim 10^{-2}$ for galaxies at red-shifts $z \ll 1$, i.e. today. This is a necessary requirement for any consistent theory of structure formation [22].

If the perturbations are adiabatic, i.e. number densities of photons and matter are equally affected, the linear growth law for matter perturbations is simple:

$$\delta \propto \begin{cases} \mathrm{a}(t)^2 & \text{Rad. Dominated Universe,} \\ \mathrm{a}(t) & \text{Matt. Dominated Universe.} \end{cases} \tag{1.47}$$

Nevertheless, the radiation component of the Universe applies a pressure that opposes gravity. In the radiation era this pressure is effective and the result is that perturbations are oscillatory for wavelengths below the horizon length, so that the horizon at the moment of matter-radiation equivalence

$$D_H(z_{eq}) = \frac{2(\sqrt{2}-1)}{(\Omega_{mat}z_{eq})^{1/2}H_0} = \frac{16.0}{\Omega_{mat}h^2}\ \mathrm{Mpc} \tag{1.48}$$

will play a role for structure formation.

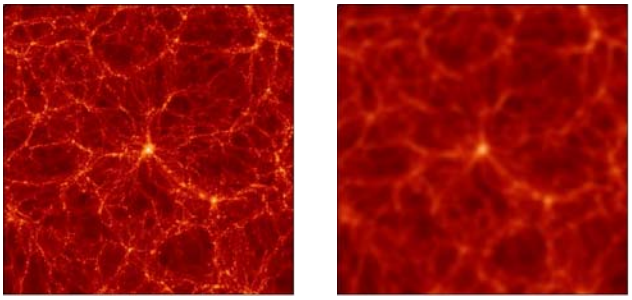

Figure 1.3: *Different structure formation scenarios arise depending on the relative importance of relativistic (hot) or non relativistic (cold) particles in the Universe. In the latter case small scale structures form first and then aggregate into large scale ones (left image) while in the former, large scale structures fragment into small ones at later times (right image); current data and simulations favour the “cold” scenario.*

In addition, the very kind of involved particles can change how the process evolves. Relativistic particles tend to diffuse from one concentration of matter to another, thus transferring energy among them and preventing the growth of structure on small scales, which will be produced only later by fragmentation of larger ones; on the other hand, non-relativistic particles tend to cluster, so that gravitational collapse amplifies the density contrast, linearly in the first place and later on via nonlinear collapse. In the process, over-dense regions decouple from the Hubble expansion to become bound systems, which start attracting each other to form larger bound structures, as exemplified in figure 1.3.

A scenario with dominant relativistic (hot) particles is disfavoured both by observation and numerical simulations, since it implies a number of small scale structure inferior to the observed, so it is commonly accepted that most of the particles in the Universe should have been non relativistic since early times (cold particles).

1.5 Determination of cosmological parameters

In the previous sections we have reviewed the basic aspects of cosmology, showing in particular how the global parameters of the theory influence the structure and history of the Universe and how they evolve in time. This implies that we can track the history of the Universe back in time once measured the present day value of the parameters themselves.

Some of them we have already estimated; for instance in section 1.2.1 we have used the black body energy density of the CMB to evaluate the radiation energy density $\Omega_\gamma = (4.9 \pm 0.5) \times 10^{-5}$ and from the theory of nucleosynthesis (section 1.2.2) we have a tight constrain on the value of baryon density $\Omega_{bar} = 0.024 \div 0.05$

The other parameters[4], namely the expansion rate H_0, the matter density Ω_{mat} and the vacuum (or cosmological constant) density Ω_Λ, can be determined by astronomical and astrophysical observations that fall essentially in three categories:

- measurements based on the observation of gravitational effects on the properties of astronomical objects, to estimate the amount of matter present in the Universe,
- astrophysical measurements of objects on cosmological distances, that can be used to infer the dynamical parameters (H, q) connected to the geometry of the Universe and its expansion history, which depends on the relative importance of matter and vacuum contribution in the energy budget,
- observation of the properties of the perturbations that should have originated in the early universe at the time of inflation. Their subsequent evolution depends on the cosmological parameters, so that from the signatures they left in the matter distribution and CMB are good tools to evaluate the parameters themselves.

1.5.1 Gravitational probes: matter and Dark Matter

An example of method based on astrophysical observations is the measure of the rotation curves of galaxies and clusters. A rotation curve is just the measurement of the orbital velocity of objects belonging to a gravitational system as a function of their distance from the centre of the system itself. Since the binding force is gravitation, a measure of orbital velocity (v) amounts to a measure of the binding mass (M_b) according to the formula one can easily derive from Newton's law:

$$v^2 = \frac{M_b G}{d} \; ; \qquad (1.49)$$

it is then straightforward to obtain the value of the matter density, which is found to be about $\Omega_{mat} \approx 0.27 \div 0.30$.

---

[4] Actually for a thorough parametrisation of the Universe today contains about ten parameters, but we only discuss the global energy densities.

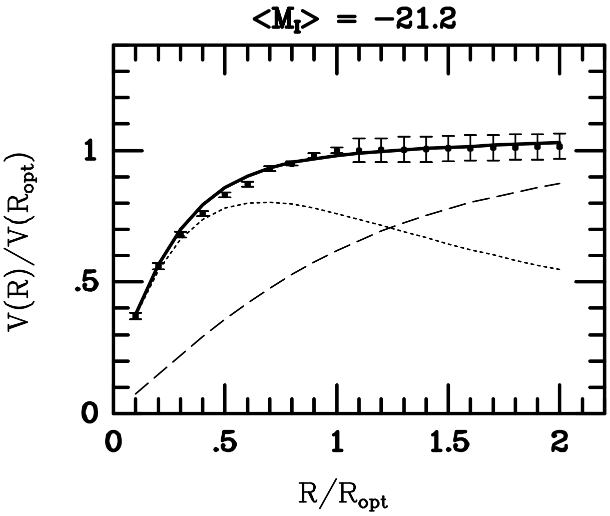

Figure 1.4: *Synthetic rotation curve for galaxies with $\langle M\rangle = -21.2$. The dotted curve shows the disk contribution, whereas the dashed curve shows the halo contribution. The R coordinate is expressed in units of the optical radius of the observed galaxies [26, 27].*

Such measurements were performed in the thirties on galaxy clusters [23], and it turned out that this mass determination was in utter disagreement with what would be expected if galactic masses were estimated on a statistical basis, by means of the average mass and number of stars observed in galaxies, which yielded values smaller by a factor ≈ 10. Later on in the seventies the same behaviour was observed in galaxies measuring the 21 cm emission line of neutral hydrogen, which is still present at a distance from the galactic centre beyond the *optical radius*, where most of light emission ceases [24, 25].

Figure 1.4 shows a typical subset of a recent compilation of rotation curves of spiral galaxies [26, 27], to illustrate the effect. The halo contribution (dashed line) compatible with a mass distribution $\propto r$ was the first direct evidence for the presence of huge amounts of matter that cannot be detected by its light emission and is therefore called Dark Matter (DM).

Since it appears to be the greater part of existing matter, it plays an important role in the Universe's energy balance. It should be noticed too, that BBN consistency requires that baryons are no more than at best 10% of the total amount of matter, so they can not account for DM for more than a negligible fraction.

Another method to determine the mass of a galaxy through its gravitational properties is to measure the lensing effect of its gravitational field on the light coming from sources in its background [28, 29] which substantially confirm the Ω_{mat} value from rotation curves.

1.5.2 Geometrical probes

The geometrical probes essentially consist in the measurements of relationships between quantities connected to the metric curvature k and to the way expansion is going on.

For instance we can consider the relation between distance and red-shift, which is expressed by the Hubble law:

$$d = \frac{z}{H} \ . \tag{1.50}$$

This relation is only valid at low values of the red-shift z; in fact it is only considers the first order of the Taylor expansion of the Hubble parameter as a function of red-shift $H(z)$. If we go to the second order the relation reads:

$$d = \frac{1}{H_0}\left(z + (1 - q_0)z^2\right) \ , \tag{1.51}$$

where q_0 is the present-day value of the deceleration parameter defined in equation (1.8). Measuring the deviation from the linear version of Hubble's law at high red-shifts is then equivalent to a measure of q_0.

As these measurements involve $z > 0.1$, the determination of the distance is best performed using the so called luminosity distance. If we do know the absolute luminosity L of the object, its luminosity distance d_L is defined as the distance at which that L would yield a flux equal to the observed one.

To apply this method it is necessary to have a class of objects for which the absolute luminosity is known in advance within good approximation (standard candles). One such class are the type Ia supernovae, that are essentially white dwarf stars that accrete matter until self gravitation ignites the nuclear reactions that produce the explosion [30]. Although not perfect "standard candles", it has been demonstrated that by correcting for a relation between the light curve shape and the luminosity at maximum brightness, the dispersion of the measured luminosities can be greatly reduced.

Substituting the value of q_0 in terms of Ω_{mat} and Ω_Λ (Ω_{rad} can be safely neglected) from equation (1.21), we obtain to second order in z:

$$d_L H_0 = z + \frac{1}{2}\left(1 - \frac{\Omega_{mat}}{2} + \Omega_\Lambda\right) \ . \tag{1.52}$$

Through equation (1.52), the measurement of q_0 with its uncertainty identifies a region in the $(\Omega_{mat}, \Omega_\Lambda)$ plane, that is shown in figure 1.5. Here the dashed line represents the condition that produces a flat geometry ($k = 0$); the almost horizontal solid curve marks the separation between an ever expanding Universe on the upper part of the diagram and a re-collapsing one on the lower. Up to the 99% C.L. the Ia data are consistent with a cosmology without final re-collapse and rule out the Einstein-de Sitter model (see section 1.1.3).

According to this result the cosmological constant contribution to Ω_{tot} increases with Ω_{mat} and is therefore non zero up to ≈ 1.7 (the upper bound of the 99% C.L. region). If we accept the result $\Omega_{mat} = 0.3$ from gravitational probes ad combine it with this one (thick vertical line on the graph), we find that they point to a flat Universe configuration, such that $\Omega_\Lambda = 0.7$.

1.5.3 Perturbation observation

An important consequence of inflation (section 1.3), is that quantum fluctuations of the inflaton field are stretched by the exponential expansion and generate large-scale perturbations in the metric. These perturbations propagate like waves in the space-time metric, with a frequency spectrum that is approximately scale invariant.

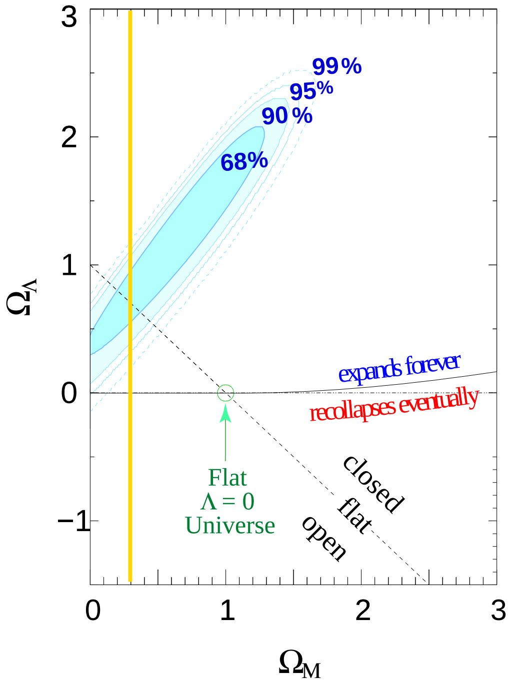

Figure 1.5: *The figure shows the best-fit confidence regions (68% 99% C.L.) in the (Ω_{mat},Ω_Λ) plane, for the high redshift supernovae results. The systematic uncertainty is not shown, and would shift the ellipses vertically.Assuming as correct the value of Ω_{mat} from rotation curve measurements (vertical thick line), we find agreement with the hypothesis of flat universe (dashed line), while the Einstein-de Sitter model (circle) is disfavoured by several standard deviations. In any case, the data point to an expanding universe with no possibility of re-collapse.*

Matter that fell in the troughs of these waves formed the seeds for subsequent structure formation and originated the inhomogeneities in the CMB at the time of the last scattering of photons and matter, thus accurate measurements of the spatial distribution of galaxies or of the anisotropies of CMB, can give considerable insight on the early Universe and allow the determination of its actual cosmological parameters.

The distribution of galaxies in the Universe is connected to structure formation and mainly probes the values of Ω_{mat} and Ω_{bar}. Since the primordial spectrum is approximately represented by a scale-invariant Gaussian random field, the best way to present the results of structure formation is by working with the 2-point correlation function in Fourier space, the so-called power spectrum. If the reprocessed spectrum of inhomogeneities remains Gaussian, the power spectrum will contain all of the information about the galaxy distribution. Non-Gaussian effects are expected to arise from the nonlinear gravitational collapse of structure, and may be important at small scales [21].

The power spectrum measures the degree of inhomogeneity in the mass distribution on different scales. It depends upon the primordial spectrum of inhomogeneities, and on their evolution. The power spectrum measured by the 2dFGRS [31] (see figure 1.6) is well fit by a model with $\Omega_{mat}h = 0.18 \pm 0.02$, that using the latest values for the reduced Hubble parameter is compatible with $\Omega_{mat} = 0.28$ and a baryon fraction $\Omega_{bar}/\Omega_{mat} = 0.17 \pm 0.06$ [32].

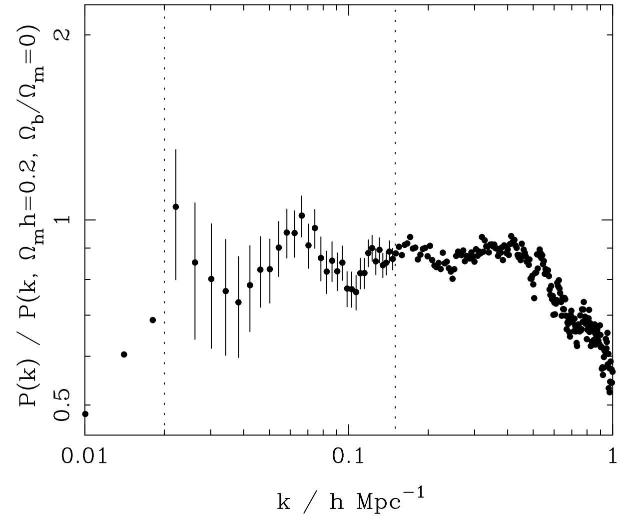

Figure 1.6: *Galaxy power spectrum as measured by 2dFGRS (from [32]).*

The CMB anisotropies are the other important mean of investigation on the metric perturbations; when radiation and matter were still coupled, photons, electrons and protons behaved like a single fluid, whose mass density was supplied by matter, while radiation provided for pressure. In this medium the perturbations raised acoustic oscillations driven by gravity and the normal expansion of the Universe grew the scale of the oscillations until the time of last scattering after recombination. Since then the acoustic waves features were frozen in the newborn Cosmic Microwave Background as a series of harmonic peaks [33, 34], whose shape and position are related to the details of the expansion, and indirectly to the cosmological parameters.

The anisotropies of Cosmic Microwave Background are at the 10^{-5} level, over a wide range of angular scales, and are usually expressed using a spherical harmonic expansion of the observed temperature field:

$$T(\theta, \phi) = \sum_{\ell,m} \alpha_{\ell,m} Y_{\ell,m}(\theta, \phi) \ . \tag{1.53}$$

In the hypothesis that the $\alpha_{\ell,m}$ modes are Gaussian random fields, as several tests seem to confirm [35], then the anisotropies are fully characterised by the two point correlation function between directions $\hat{n}_1$ and $\hat{n}_2$:

$$\langle \frac{\delta T}{T}(\hat{n}_1, \hat{n}_2) \rangle = \sum_{\ell} \frac{2\ell + 1}{4\pi} C_\ell P_\ell(\ \cos(\hat{n}_1 \cdot \hat{n}_2)\ )\ , \tag{1.54}$$

where $C_\ell = \langle |\alpha_{\ell,m}|^2 \rangle$ and P_ℓ are the Legendre polynomials.

Theoretical predictions for different values of the cosmological parameters are shown in figure 1.7; as the oscillations are driven by gravity, the amplitudes of the acoustic peaks are related to the amount of matter in the Universe, hence to Ω_{mat}, Ω_{bar} and the Hubble parameter, so an accurate measure of the first peaks allows to evaluate them. The secondary ones are generally of smaller amplitude because of diffusion against the baryonic matter (Silk damping). [36]

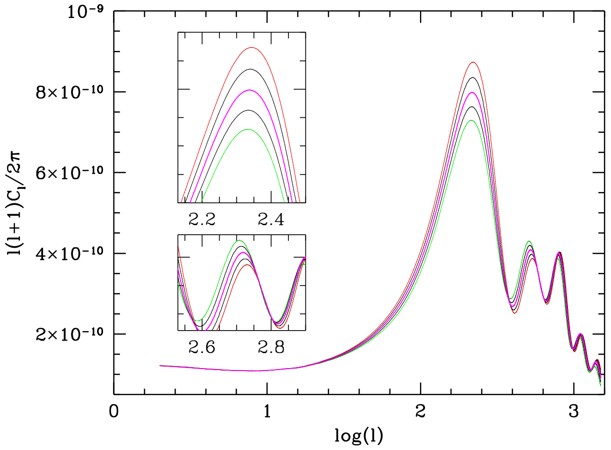

Figure 1.7: *CMB harmonic peaks as predicted using different sets of cosmological parameters. The value of Ω_{bar} is varied while keeping Ω_{mat} constant. We can see how this changes the relative height of the first and second peaks in the two close ups.*

In addition, the scale associated with the main peak can be confidently calculated as a physical length scale, since it is the sound horizon at last scattering. This scale is nowadays observed under an angular scale that depends on the geometry of the Universe. Since the photons travel along geodesics, that are represented as straight lines, inwards or outwards trajectories in the case of a flat, open or closed Universe geometry respectively and the angle subtended by the sound horizon is altered accordingly.

The position of the first peak (ℓ_{peak}) of the correlation function can then be expressed in terms of the total density of the Universe in the form:

$$\ell_{peak} \simeq 220\Omega_{tot}^{-1/2} = 220\,(1-\Omega_k)^{-1/2} \quad . \tag{1.55}$$

From equation (1.55) we see that in terms of multipolar coefficients a larger (smaller) angular scale corresponds to a lower (higher) multipole order in the expansion and that for a flat Universe we should have the peak about $\ell = 220$.

Over the last decade several experiments have investigated the CMB since the first detection by the COBE satellite [37], both balloon-borne (BOOMERANG [38], MAXIMA [39],ARCHEOPS [40]) and ground-based (CBI [41], ACBAR [42] DASI [43],VSA [44]). This activity reached a climax with the results of the WMAP satellite [45], that provides today the most solid and extensive experimental determination of the CMB features, as for the first time the measurement accuracy allows to clearly identify the second peak of the power spectrum and a hint on the third. All these observations support the hypothesis of an inflationary Hot Big Bang, confirm the hypothesis of primordial Gaussian adiabatic perturbations and sets the epoch of recombination at redshift $z = 1100$.

The analysis of WMAP data, either by themselves or complemented with those from the other CMB experiments, produced a number of important results in the field of cos-

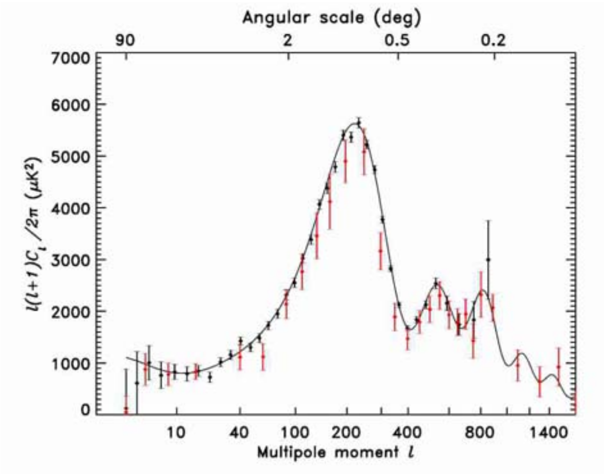

Figure 1.8: *CMB power spectrum as measured by WMAP (black markers) and by previous experiments (red markers). The WMAP error bars are smaller up to $\ell \approx 500$, allowing the identification of the second harmonic peak.*

mological parameters determination. As the evaluation is based on multi-parameter fits to cosmological models, WMAP data alone may be affected by the choice of the "prior" ranges for the various parameters; nonetheless, using the data available from other kinds of observation (e. g. 2dFGRS), it is possible to impose provide stronger constraints on the priors and achieve reliable fit results.

In figure 1.8 is displayed the CMB power spectrum as measured by WMAP (black markers) in comparison to the previous ones (red markers); the solid line is the WMAP best fit. We notice that the first peak is located at just the right position for a flat universe. In fact WMAP finds the value $\Omega_{tot} = 1.02 \pm 0.02$, which is a strong indication for a flat Universe.

For the other parameters, the best fit on WMAP data, favours $\Omega_{mat} \simeq 0.3$, $\Omega_{\Lambda} \simeq 0.7$ and $\Omega_{bar} \simeq 0.04$, well compatible with all of the independent determinations we presented in the previous sections.

Our picture of the Universe is becoming quite definite and is expected to improve as more data are being collected by the working experiments (e.g. WMAP, 2dFGRS) and new ones are in preparation that should allow more accurate measurements, such as the PLANCK project for CMB observation funded by ESA [46]. However the argument is far from exhausted; the nature of vacuum energy and DM, both implied by the measured values of cosmological parameters, and for the latter by the gravitational probes by themselves as briefly pointed out in section 1.5.1.

In the next chapter we will discuss in more detail the features that make a good DM candidate and what kind of measurements can be performed to understand its nature.

Chapter 2

Dark Matter

In the last part of the previous chapter we reviewed various methods to determine the cosmological parameters. These methods test the predictions of independently developed theories, such as gravitation in the case of rotation curves, BBN when we measure the light elements abundance or cosmological models and inflation if we observe the Universe anisotropies.

The remarkable fact is that all those observations point in a common direction: a Hot Big Bang cosmological model that produces by means of an inflationary era a spatially flat Universe, whose dynamics are dominated by vacuum energy, first introduced as Einstein's cosmological constant and often referred to as Dark Energy.

Another interesting point is that the baryon fraction, is definitely a minor contribution to the total matter content of the Universe; the remaining is usually called Dark Matter (DM), because of its extremely weak coupling to photons (if any). Up to now DM is only detected by the effects of its gravitational field (rotation curves, gravitational lensing); the most sophisticated observations too, such as the study of anisotropies using the CMB, can sense its presence because the perturbations are driven by gravity that affects baryons and DM alike.

The nature of DM is yet to be understood, and there are many theoretical speculations and experimental efforts on the subject.

2.1 Dark Matter properties

Under the name of "Dark Matter" can be generically inscribed any non relativistic component of the Universe which does not emit enough light to be detected. This would allow ordinary matter with low emission to account for DM, and indeed the presence of cold hydrogen gas in the halo has been suggested. However such gas should have reached hydrostatic equilibrium during the age of the galaxies and the equation of state combined to the gravitational potential, gives for the temperature [47]:

$$T = \frac{G M_P M(r)}{4k\pi} \simeq 1.3 \times 10^6 \text{ K} , \tag{2.1}$$

where $M(r)$ is the mass contained within the distance r from the centre of the gas cloud, G is the Newton constant of gravitation, k the Boltzmann constant and M_P is the Planck mass. This is not cold gas and would be detectable through X-ray emission.

Other possible sources of ordinary (i.e. baryonic) DM, are the so called MACHOs (Massive Compact Halo Objects), essentially remnants of late stages in star evolution, like white dwarfs, neutron stars and black holes, or forming stars that have not enough mass to ignite the nuclear reactions (brown dwarf/Jupiter-like objects). Searches for these candidates in our galaxy halo have been performed by different collaborations (MACHO [48] , EROS [49], OGLE [50]) using their gravitational lensing effect as a probe. Some tens of MACHOs were found with masses up to $0.1 \div 0.4\ \mathrm{M}_{\odot}$, but they can only account for 20% of the halo mass [51].

Though a part of existing DM is constituted by ordinary baryons, Big Bang Nucleosyntesis Cosmic Microwave Background and Galaxy Red shift Surveys data, show that the baryon contribution to the Universe energy density cannot exceed $\Omega_{bar} \approx 0.04$, while $\Omega_{mat} \simeq 0.3$, so the main constituent of Dark Matter must belong to a non baryonic particle species, whose interaction other than gravitational with ordinary matter is ruled by the weak force, otherwise we would have observed it long ago.

This implies that they fell out of the thermal equilibrium condition of equation (1.24) at some time and now constitute a relic population distributed throughout the Universe.

To ensure that these relic particles survive until the present, without decaying into something that couples to photons, they must also be stable, or at least have a lifetime that is comparable to the age of the Universe.

2.2 Non baryonic Dark Matter

Several candidates to the role of non baryonic DM have been proposed over time, including primordial black holes, (i.e. formed before BBN), massive neutrinos, axions and Weakly Interacting Massive Particles (WIMPs).

Primordial black holes, require particular initial conditions for the cosmological model involved [52], and we will not treat them here, but we will concentrate on the other three.

2.2.1 Neutrinos

Among the known particles, only neutrinos are both weakly interacting and non baryonic; we also know them to be present as a relic background analogous to the CMB as explained in section 1.2.3.

If neutrinos have a mass, as experiments on ν oscillation suggest [53, 54], their contribution to the energy density could be calculated as:

$$\Omega_{\nu} = \frac{\sum m_{\nu}}{94\ \mathrm{eV}} h^{-2} \ , \tag{2.2}$$

These oscillation experiments do not tell us the absolute neutrino masses, but only the squared mass difference between flavours, however the measured values ($\Delta m \sim \mathcal{O}(10^{-3}\mathrm{eV}^2\ )$) suggest a lower limit of $\Omega_{\nu} \approx 0.001$ on the neutrino mass density parameter. If the neutrino masses are significantly bigger than their differences, the contribution to Ω_{tot} could raise, however the results on tritium limits the sum of the masses of active neutrinos in the range $0.05 \div 8.4$ eV, which yields an upper limit of $\Omega_{\nu} \approx 0.18$.

As pointed out in section 1.4, particles that decouple from the primordial thermal bath while still relativistic (hot) like neutrinos do, damps the growth of perturbations so, for a total ν mass as small as 0.1 eV this could have a potentially observable effect on the formation of structure.

Present cosmological observations (WMAP plus 2dFGRS data) have shown no convincing evidence of any effects from either neutrino masses or an otherwise non-standard neutrino sector, and impose more stringent upper limits ($\Omega_\nu < 0.013 \div 0.015$ [45,55]. Moreover, structure formation data rule out the possibility of Hot Dark Matter as the dominant component of Ω_{mat}, so DM particles must be cold ones.

2.2.2 Axions

A possible Cold Dark Matter (CDM) candidate is the *axion*: a particle introduced to solve the Strong CP problem, connected to the CP violating term of the QCD Lagrangian:

$$\mathcal{L}_{CP} = \Theta \frac{g^2}{32\pi^2} G^a_{\mu\nu} \widetilde{G}^{a\mu\nu} \ , \tag{2.3}$$

where $G^a_{\mu\nu}$ and $\widetilde{G}^{a\mu\nu}$ are the gluon field strength and its dual respectively, while Θ is a dimensionless parameter, whose value sets the magnitude of the effective term (2.3) of the Lagrangian.

The axion is a pseudo Nambu-Goldstone boson of the spontaneously broken Peccei-Quinn symmetry [56]. When the symmetry breaks the axions acquire an effective coupling to gluons that cancels the Θ parameter of equation (2.3), thus solving the problem.

Since the axions are not produced thermally in the primordial plasma, they can be counted as CDM whatever their mass. In particular if $m_a \sim 10$ μeV they could be the dominant component of DM. The cosmologically relevant mass range is explored by the experiments based on axion-photon interaction: in particular LLNL [57,58] that currently excludes $m_a = 2.9 \div 3.3$ μeV and CARRACK [59, 60] is being upgraded to probe the range $2 \div 50$ μeV.

2.3 Weakly Interacting Massive Particles

Under the name of WIMPs are classified the particles other than neutrinos and axions that have the characteristics to make a good DM candidate we have met throughout our discussion; namely they are:

- non baryonic,
- long lived with respect to Universe age or stable,
- present as a relic population,
- massive (typically $m_\chi = 10$ GeV $\div$ 1 TeV) hence,
- non relativistic at decoupling after the discussion on structure formation of section 1.4 (CDM) and,
- their cross sections are approximately of order of the weak strength.

The relic energy density of WIMPs can be evaluated as [61]:

$$\Omega_\chi \propto \frac{T_0^3}{{M_P}^3 \langle \sigma_A v \rangle} \simeq \frac{0.1 \text{ pb} \cdot c}{\langle \sigma_A v \rangle} \, , \tag{2.4}$$

where M_P is the Planck mass, c the speed of light, T_0 the present day temperature of CMB,σ_A is the total annihilation cross section of a pair of WIMPs into SM particles and v their relative velocity. The angle brackets $\langle \; \rangle$ denote thermal average. If the cross section is of the order typical for weak interactions, equation (2.4) yields a possibly dominant contribution to Ω_{mat}.

2.3.1 Supersymmetric WIMPs

Particles of this kind appear naturally in the context of Supersymmetric extensions to the Standard Model of particle physics. All SUSY theories are based on the assumption that in nature exists an additional symmetry that connects fermions to boson partners of the same mass and vice versa: this allows for example to solve the scalar mass hierarchy problem, since the contribution of the partner particles to the Higgs mass correction have opposite signs and cancel each other [62]:

$$\delta m_H^2 = \mathcal{O}(\frac{\alpha}{\pi})|m_B^2 - m_F^2| \, . \tag{2.5}$$

When the symmetry is broken at some scale Λ_{SUSY}, the partners masses are no more equal and the cancelation is no more exact, so the Higgs fields mass acquire a radiative correction term of the order of the breaking scale: it follows that $\Lambda_{SUSY} \sim \mathcal{O}(\text{TeV})$.

Even if we consider the minimal Supersymmetric extension to the Standard Model, i.e. the one where only strictly necessary additions are made (for instance two Higgs doublets are required), new interaction channels involving both particles and superpartners are opened. One such channel implies so small a lifetime for the proton that it should have disappeared from the Universe by now.

To overcome this difficulty, a discrete symmetry called *R-parity* was introduced in the theory; the corresponding multiplicative quantum number called R, is defined in terms of the particle spin, lepton number and baryon through the relation $R = (-1)^{3B+L+2S}$, that implies $R = 1$ for ordinary particles and $R = -1$ for the superpartners. If R-parity is a conserved quantity, Supersymmetric particles (also called sparticles), are forbidden to decay into ordinary ones, so the Lightest Supersimmetric Particle (LSP), is bound to be stable for lack of phase space.

Moreover these stable particles cannot carry charge nor colour, otherwise they would bind to ordinary matter producing anomalous isotopic masses [63], which is excluded by quite stringent experimental constraints [64].

The identity of the LSP depends on the parameters of the theory, but the most quoted one is the *neutralino*, linear combination of the $R = -1$ neutral sfermions [63], superpartners of the neutral electroweak gauge bosons W_3 and B and of the two neutral Higgs states, namely the wino $\widetilde{W}$, the bino $\widetilde{B}$, and the $\widetilde{H}_{1,2}$:

$$\chi = \alpha \widetilde{\mathrm{W}}_3 + \beta \widetilde{\mathrm{B}} + \gamma \widetilde{\mathrm{H}}_1^0 + \delta \widetilde{\mathrm{H}}_2^0 \, . \tag{2.6}$$

Depending on the value of the quantity $P = \alpha^2 + \beta^2$ it is further classified as gaugino ($P > 0.9$), higgsino ($P < 0.1$) or mixed [65]. Another property of the neutralino is that $\chi = \bar{\chi}$ i.e. it is a Majorana fermion.

Although the exact nature of neutralino depends on the particular SUSY implementation, it is possible to find for each model a region of the parameter space that is consistent with a relic neutralino density consistent with cosmological observations.

2.4 WIMP Dark Matter Searches

The techniques to search for WIMPs fall essentially in two categories: direct detection, based on the measurement of the interaction of the WIMP with ordinary matter, and indirect detection that looks for the products of WIMP pair annihilation. In both cases the uncertainty in the DM density and velocity distribution affect the calculation of the expected signal rate. In particular, an higher density due to a cusp toward the galactic centre or a clumpy distribution in the halo, as favoured by numerical simulations [66] would increase the annihilation rate allowing indirect detection in a wider range of SUSY models while the velocity distribution uncertainties, though important for annihilation calculations too, mostly affects the direct search experiments [67].

2.4.1 Direct searches

Direct searches essentially look for the recoil of target nuclei due to interaction with the WIMP; natural radioactivity is a major noise source so the typical direct search experiment is performed in underground laboratories and requires the use of materials devoid of radioactive isotopes to a high degree and the weakness of the interaction forces to use large amounts of target material.

The experimental signatures of WIMP detection, that would prove its cosmological origin are the daily and annual modulations of the signal due to the Earth motion.

Several experiments are being performed along these lines with different recoil detection techniques (for a review see [68]) among them the DAMA experiment that uses a 100 kg $\mathrm{NaI(Tl)}$ target in the Gran Sasso laboratory has observed with a statistical significance of 6.3 σ an annually modulated signal with the expected phase [69] over a 7 years observation period attributed to a WIMP signal by the collaboration. However the results of EDELWEISS exclude the DAMA result with a C.L. of 99.8%. Extended versions of current experiments are planned to further investigate on the subject (e.g. LIBRA [68].

2.4.2 Indirect searches

Though WIMPs must be stable, nothing prevents them from annihilating with their antiparticle; indirect searches look for the annihilation products in the CR in order to detect an excess with respect to the abundance predicted by known production processes.

In the case of neutralino particle and antiparticle coincide and may annihilate into quarks ($\chi\chi \to q\bar{q}$), leptons ($\chi\chi \to \ell\bar{\ell}$), gauge bosons ($\chi\chi \to W^+W^-, Z^0Z^0$), Higgs bosons ($\chi\chi \to Z^0H^0_{1,2}, H^0_1H^0_{,}2\ldots$) and gluons ($\chi\chi \to gg$). These in turn decay or hadronise leading to final states containing e^+, $\bar{\mathrm{p}}$, γ and ν [65].

Neutrinos

Neutralinos trapped into the core of celestial objects such as the bulge of the Galaxy, the Sun or even the Earth by gravity [70] would provide a typical signature in the neutrino channel. Among the final annihilation products, only neutrinos would be able to escape and the excess flux would be observed in a precise direction. Current neutrino experiments have put limits to the ν_μ flux due to this mechanism that tend to exclude the portion of parameter space favoured by DAMA ([71] and more recently [72]).

Gammas

The most distinctive feature of the γ-ray spectrum that can be observed as a consequence of neutralino annihilation is certainly the presence of sharp spectral lines. The loop-induced annihilation processes $\chi\chi \rightarrow \gamma\gamma$ and $\chi\chi \rightarrow Z\gamma$ [73] should produce mono-energetic photons, since the neutralinos involved in the process may be considered almost at rest. The energy of the photons is then calculated to be $\mathrm{E}_\gamma = m_\chi$ and $\mathrm{E}_\gamma = m_\chi \left(1 - m_Z^2/4m_\chi^2\right)$ respectively.

The rates of these processes are difficult to estimate because of uncertainties in the supersymmetric parameters, cross sections and halo density profile. However, in contrast to the other proposed detection methods they have the virtue of giving a direct measurement of the neutralino mass.

In practice the monochromatic spectral lines will suffer a smearing due to red-shift that can turn them in features of the continuum annihilation spectrum. As red-shift only stretches the observed wavelength of the photons, the smear is asymmetric and looks like a cutoff at about the value of the neutralino mass (for $\chi\chi \rightarrow \gamma\gamma$) [74].

A second signature may be found in the continuum γ-ray spectrum, though less dramatic, in the form of a smooth bump at about one tenth of the neutralino mass. This signal is very low if compared with the flux measured by EGRET [75] (about 5 orders of magnitude), though there is the possibility that the bulk of EGRET flux may be due to unresolved AGN. In this case AMS, the GLAST [76] satellite or one of the air Čerenkov telescopes (e.g. VERITAS) [77], that will explore a quite complementary energy range would have good chances to pick this kind of signal. Moreover it is possible that clumpy distributions of DM enhance the signal itself.

Anti-deuterons

Anti-deuterons form when an anti-proton and an anti-neutron produced in spallation processes in the Inter Stellar Medium (ISM) merge. The two anti-nucleons must be at rest with respect to each other in order for fusion to take place, however, for kinematic reasons, a spallation reaction creates very few low-energy particles and low-energy secondary anti-deuterons are even further suppressed. The corresponding interstellar flux reaches at maximum $(2 \div 5) \times 10^8\ \mathrm{m}^{-2}\mathrm{s}^{-1}\mathrm{sr}^{-1}\mathrm{GeV}^{-1}$ for a kinetic energy of $4\ \mathrm{GeV}$ [78].

On the other hand, supersymmetric $\bar{\mathrm{D}}$ are produced practically at rest with respect to the Galaxy since in neutralino annihilation, anti-nucleons are predominantly produced with low energies. This feature is further enhanced by their subsequent fusion into anti-deuterons. Below a few $\mathrm{GeV/n}$, secondary anti-deuterons are quite suppressed with respect to their supersymmetric produced counterparts. This makes CR anti-deuterons a possible probe of supersymmetric DM capable to explore a significant portion of the supersymmetric parameter space.

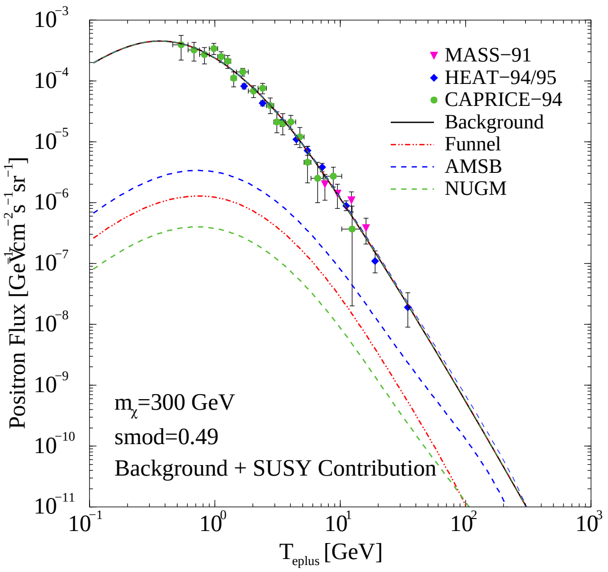

Figure 2.1: *The solar modulated positron flux, as a function of the positrons kinetic energy T_{eplus}. The black line corresponds to the calculated background, while the three coloured lines to the signal for three particular* SUSY *models (further discussed in the following) at a mass $m_\chi = 300$ GeV [84]. The positron data from* MASS *[85],* HEAT *[86] and* CAPRICE *[87] are also shown.*

Positrons

The CR also have a leptonic component made of electrons and positrons. The spectra of these particles have specific features, that rise from the complete lack of hadronic interaction and the heavy energy losses due to EM interaction. In fact the dominant process that electrons and positrons undergo while propagating in the ISM, is Bremsstrahlung, with contributions from ionisation interactions with the ISM itself under a few GeV and inverse Compton scattering with the CMB at higher energies. The the net effect of those interactions is to decrease the electrons energy, so they concentrate at low energies and the spectrum is therefore much steeper than for any CR nucleus [79].

Past experiments have measured the combined $\mathrm{e}^{\pm}$ energy spectrum up to the TeV region [80, 81, 82, 83], showing that their intensity is about 1% of the proton one at 10 GeV and then decreases with energy according to a power law $\mathrm{E}^{-\alpha}$ with index $\alpha > 3.0$, higher than the $\alpha \approx 2.7$ valid for protons.

The bulk of electrons is of primary origin, however exists a secondary population of both electrons and positrons, that are produced in the interaction of Cosmic Rays with the ISM through the pion decay chain $\pi \rightarrow \mu \rightarrow \mathrm{e}^-$. The measured value of the positron fraction $\mathrm{e}^+/(\mathrm{e}^+ + \mathrm{e}^-)$ is of order 0.1 in the $1 \div 10$ GeV region.

An additional component of secondary positrons may be the result of the decay chains or hadronisations due to χ annihilation products. The actual shape of the spectrum depends on the preferred decay mode of neutralino. If most of the times χ annihilates to $q\bar{q}$, the subsequent jets will broaden the energy spectrum of the final e^+s; if on the other hand the preferred annihilation channel is to W^+W^-, the positron spectrum will feature a couple of peaks: the first corresponding to $m_\chi/2$, produced by direct $W^+ \rightarrow \mathrm{e}^+$ decay, and the second — at lower energy and wider — from W decay into other leptons ($W^+ \to \tau^+(\mu^+) \to \mathrm{e}^-$) and a contribution from the quark jets too ($W^+ \to \ldots \to \pi^+ \to \mathrm{e}^+$) [88].

Among the best results achieved by balloon-borne experiments are those of CAPRICE that determined the absolute positron flux in the interval $0.4 \div 50$ GeV [87, 89] and HEAT, that operated in the range $1.2 \div 100$ GeV in two successive flights [90, 86, 91]. which are shown in figure 2.1 along with three possible Super Symmetry (SUSY) positron spectra [84]. Measurements with higher statistics and over a wider energy range are required to better check the CR propagation models and to further investigate the existence of a primary neutralino-induced e^+ component.

Anti-protons

The primary CR are mainly constituted by protons ($\sim 90\%$) and helium nuclei ($\sim 9\%$), with lesser components of heavier nuclei, electrons, positrons and anti-protons [92]. In particular, anti-protons are expected to be of secondary origin, i.e. produced in collision processes of the type $\mathrm{pp} \to \bar{\mathrm{p}}X$ in the ISM.

The first reports of the detection of CR anti-protons were published in 1979 by Golden and Bogomolov [93,94]. Shortly after these measurements, Buffington, Schindler & Pennypacker [95, 96] measured an unexpected large flux of $\bar{\mathrm{p}}$ in the few hundred MeV kinetic energy range.

Subsequent measurements made at these low energies failed to verify this claim (PBAR [97, 98] and LEAP [99] experiments). The observed fluxes were approximately one decade below the Buffington level, and were near or below the lower limit of sensitivity for these instruments.

In fact, the typical theoretical spectrum for $\bar{\mathrm{p}}$ production in the ISM features a peak at about 2 GeV (see figure 2.2), that drops off on either side due to the process threshold at low energies ($\mathrm{E} \geq 7m_p$) and to the steepness of the proton spectrum [100] at high ones. On the other hand, in neutralino annihilation events, the interacting particles are almost at rest and the produced anti-protons come from hadronisation of those particles that were directly produced in the interaction. As such, SUSY $\bar{\mathrm{p}}$ were expected to carry only a fraction of the total involved energy thus producing a detectable deformation in the $\bar{\mathrm{p}}$ spectrum at low energy (figure 2.2).

A new generation of experiments was then designed, with greater sensitivity and enhanced particle identification capabilities, that started to get more accurate measurements in the nineties; in particular the balloon-borne experiments BESS and CAPRICE, and space experiments such as PAMELA [101] and AMS [102].

Since the first flight in July 1993 [103] to the one performed during the recent solar minimum period [104, 105], BESS has identified hundreds of anti-protons in the range $0.18 \div 4.20$ GeV; CAPRICE on the other hand performed measurements at energies both lower [106] and higher [107] than ~ 5 GeV up to ~ 50 GeV (with modifications of the experimental apparatus between flights).

These experiments detected the distinctive peak at 2 GeV, thus confirming the secondary origin of most cosmic anti-protons, but the errors on the measurements (shown in figure 2.3) are still too large in order to disentangle the primary (DM) anti-protons from the secondary ones (spallation processes).

The evaluation of the DM induced contribution to the anti-proton flux is at present a field of active theoretical research that presents several difficulties on both aspects of background characterisation and signal modelisation.

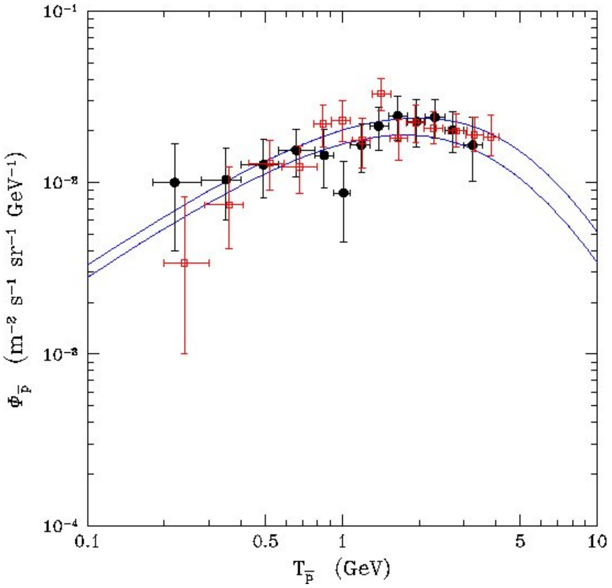

Figure 2.2: *This plot from [108] shows the envelope of the* TOA *anti-proton spectra generated with the sets of diffusion parameters consistent with* $\mathrm{B/C}$ *ratio data in the framework of the Leaky Box propagation model. Data points are taken from* BESS *95+97 [109, 105] (filled circles) and from* BESS*98 [104] (empty squares).*

On the side of the background, the principal problem is represented by the limited knowledge of the CR propagation mechanism, that determines the details of the $\bar{\mathrm{p}}$ producing interactions between primary protons, hence their spectral features.

For instance it has been suggested [110] that, in p-nucleus interaction, the production of $\bar{\mathrm{p}}$ is possible even when the impinging p has energy below the threshold of the process due to collective nuclear effects. This would enhance the low energy region of the spectrum (even more so if the produced $\bar{\mathrm{p}}$ loses energy in escaping the target nucleus).

The consequent flattening of the low energy spectrum would then drown the χ annihilation signal and the anti-proton flux and $\mathrm{p}/\bar{\mathrm{p}}$ ratio resulting from experiments would be consistent with secondary production during CR propagation through the Galaxy. In figure 2.2 the result of a semi-analytical calculation is shown along with the uncertainties due to the propagation model.

More accurate measurements of the secondary CR fluxes are necessary to refine these models. Apart from a direct observation of $\bar{\mathrm{p}}$ and e^+ fluxes, most useful information may be gathered independently from the determination of the abundances of spallation products relative to that of the original nuclei (e.g. $\mathrm{B/C}$) and from the unstable to stable isotope fraction of elements (e.g. $^{10}\mathrm{Be}/^{9}\mathrm{Be}$), that are critically influenced by the actual propagation mechanism.

On the other hand, the signal itself is not univocally determined, since different SUSY breaking mechanisms produce neutralinos with different weights of the bino ($\widetilde{\mathrm{B}}$), wino ($\widetilde{\mathrm{W}}$) and higgsino ($\widetilde{\mathrm{H}}^0$) components which implies different annihilation cross sections an branching ratios. Even within models of the same class, different choices of the various parameters would produce neutralinos of different masses, which also

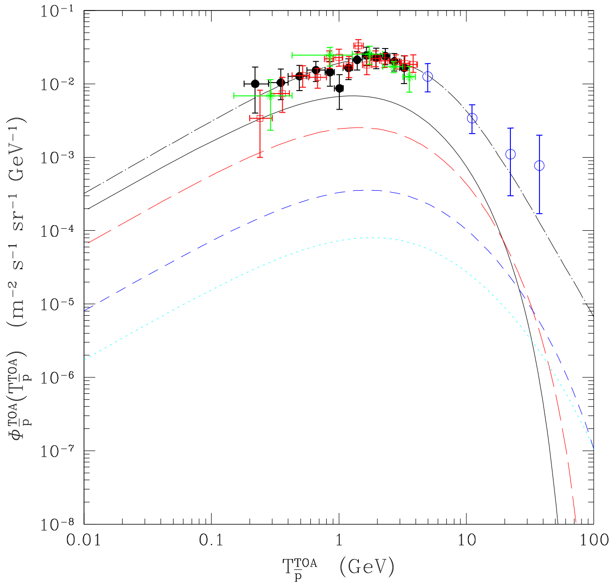

Figure 2.3: *Primary* TOA *anti-proton fluxes as a function of the anti-proton kinetic energy, in the e*MSSM *from Ref. [111]. The solid line refers to* $m_\chi = 60$ GeV, *the long-dashed line to* $m_\chi = 300$ GeV, *the dotted line to* $m_\chi = 500$ GeV. *The astrophysical parameters correspond to a median choice. Solar modulation is calculated for a period of minimal solar activity. The upper dot-dashed curve corresponds to the anti-proton secondary flux taken from references [112, 113]. The markers are results from* BESS 1995-97 *(full circles [104]),* BESS 1998 *(open squares [114]),* CAPRICE *(empty circles [107]) and the precursor flight of* AMS *(stars [115]: see also section 3.1).*

alters the signal spectrum. In figure 2.3 SUSY induced $\bar{p}$ fluxes are reported for different values of m_χ.

Moreover, the actual density profile of DM in the Galaxy is not fully understood at present. Different assumptions on the density profile may lead to significant variations of the corresponding signal flux. For instance a cuspy χ distribution towards the galactic centre could enhance the SUSY $\bar{p}$ flux by $\sim 30\%$. Such enhanced fluxes can then be observed even at energies above a few GeVas a $\sim 10\%$ contribution to the total flux. Such a signal is however comparable to the uncertainties introduced by the propagation models [108] used in the calculation.

Although a comprehensive analysis of the problem is unfeasible, given the number of involved parameters, it is possible to develop a consistent picture of both signal and background by applying a set of conservative assumptions and then coherently developing the calculations.

An example of this procedure are the Top of Atmosphere (TOA) signals reported in figure 2.4 [84]. The coloured lines correspond to three SUSY scenarios characterised by different Super Symmetry breaking mechanisms. On the same plot are also reported the available experimental data from BESS [104] and CAPRICE-98 [107].

All three models are instances of minimal supersymmetric extensions of the Standard Model. In particular both the *Funnel* [84] and *Non Universal Gaugino Mass* (NUGM) [116, 117] models involve supergravity, although the latter allows for the non universality of the gaugino mass, in term of which all other SUSY particle masses are deter-

Model	Bino fraction	Wino fraction	Higgsino fraction
Funnel	>99.6%	< 0.05%	< 0.05%
AMSB	<0.02%	> 98% for $m_\chi > 100$ GeV	> 2% for $m_\chi > 100$ GeV
NUGM	<0.01%	< 0.2%	99.8%

Table 2.1: *The lightest neutralino composition for the three* SUSY *models from reference [84] in term of the bino, wino and higgsino fractions.*

mined; the *Anomaly Mediated Symmetry Breaking* (AMSB) model [118, 119] implements a different scheme based on scale anomalies in the so called hidden sector of the theory.

The three schemes produce neutralino realisations in which one of the components is largely dominant over the other as detailed in table 2.1, and are therefore suitable to be used as benchmarks to evaluate the visibility of SUSY signals.

The fluxes were obtained by simulating the production process with the `Pythia` [120] MC package giving as input the corresponding cross sections; the SUSY parameters were chosen respecting the present constraints from accelerator data and the displayed curves in figure 2.4 refer to the specific case of neutralino mass $m_\chi = 300$ GeV.

Neutralino density distribution in the galaxy was described by the so-called Burkert profile [121]:

$$\rho_B(r)\frac{\rho_B^0}{(1+r/a)(1+(r/a)^2)}\ , \tag{2.7}$$

with the length scale parameter $a = 11.7$ kpc, that assumes a quite conservative density towards the galactic centre.

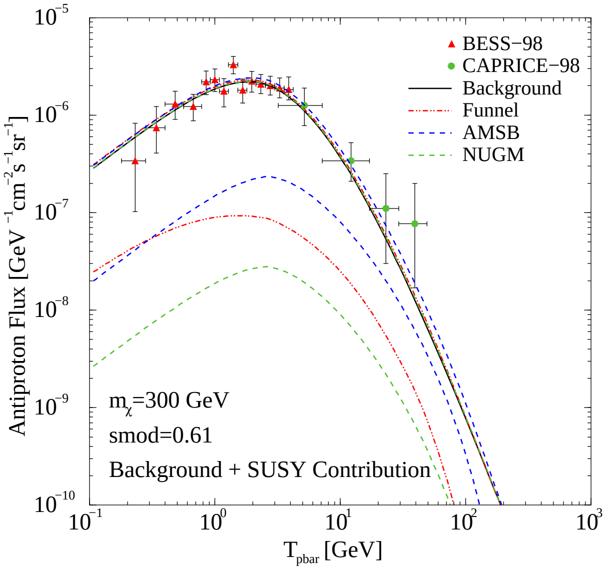

Figure 2.4: *The Solar modulated anti-proton flux, as a function of kinetic energy. The black line corresponds to the calculated background, the three coloured thick lines to the total signal for the three* SUSY *models at mass* $m_\chi = 300$ GeV*. The thin lines correspond to the* SUSY *contributions alone. The data from* BESS *[104] and* CAPRICE-98 *[107] are also shown.*

The resulting cosmic spectra were then propagated to the Top of Atmosphere by means of the `Galprop` code [122], including the effects of solar modulation implementing the one parameter model based on the analytical force-field approximation by Gleeson & Axford [123] for a spherically symmetric model.

To determine the capabilities of AMS to detect an eventual DM induced excess in the anti-proton flux, we decided to use these three models as references because they are consistent with respect to each other thus allowing to obtain results that are directly comparable even for different SUSY scenarios.

In our work we focus on the study of the anti-proton flux, however AMS is able to perform precision measurements on other channels too (e^+, $\bar{D}$, γ), and combining information from all of them, will increase the significance of any result. Moreover the measurements of cosmic nuclei that AMS will perform, can provide tight constraints for the development of more realistic propagation models, thus reducing some of the uncertainties that affect any calculation on the subject.

In the next chapter, we give a description of the AMS experimental setup, whose characteristics we exploited in the course of this work.

Chapter 3

The AMS experiment

Large acceptance, long exposure time, excellent particle identification and accurate rigidity and charge measurements are the mandatory requirements for any space borne experiment in order to extend the current knowledge of the CR flux composition and energy spectrum. The Alpha Magnetic Spectrometer (AMS) has been designed to fulfil all these requirements, with the main goals of searching for anti-nuclei, as remnants of primordial anti-matter, and of measuring the faintest components of the cosmic flux, anti-protons, positrons and high energy photons, as indirect signatures of DM. The precise measurements of the various particle and ion spectra, as well as of their relative abundance and isotopic composition that AMS can perform, will be of prime importance to further refine the present CR acceleration and propagation models.

The AMS experiment will operate in space, as an attached payload of the ISS, along a 52° orbit at ~ 400 km of altitude. The mission is foreseen to start in 2007[1] and to last for a minimum of three years.

In the following, we will first introduce the general concept of the instrument, then reviewing its components with particular emphasis on their characteristics which are more relevant in the anti-proton signal detection.

3.1 The overall concept

The AMS detector has been conceived as a state of the art particle physics experiment, where redundant measurements of the particle characteristics are performed by means of different sub-systems. A schematic view of the AMS detector is shown in figure 3.1. From the top to the bottom of the instrument, its main elements are:

- A twenty layers Transition Radiation Detector (TRD) to clearly identify relativistic particles.
- Four layers of scintillators (TOF system) which perform the time of flight and $\mathrm{d}E/\mathrm{d}x$ measurements. The fast response of this detector is also used as input for the charged particle trigger.
- A superconducting magnet, which provides a dipolar field of 0.86 T, for a bending power of $BL^2 = 0.86\ \mathrm{Tm}^2$.

---

[1] The exact launch date will depend on the restart of the Shuttle program after the Columbia accident in 2002

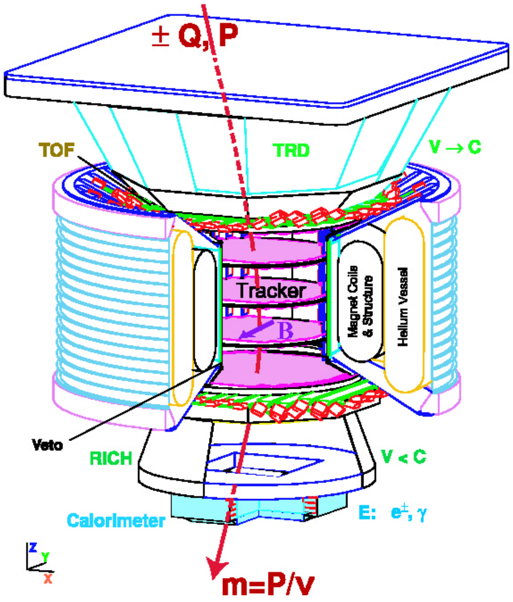

Figure 3.1: *Schematic view of the* AMS*-02 detector*

- Eight layers of double side silicon microstrip detectors (TRACKER) providing accurate measurement of the particle trajectory in both bending and non bending coordinates. The $\mathrm{dE}/\mathrm{d}x$ measurement in Si will be used to identify particles charges up to Iron.

- Anticoincidence counters (ACC), used as veto, which ensure that only particles passing through the magnet aperture will be accepted.

- A Ring Imaging Čerenkov (RICH), which measures the velocity and the charge (|Z|) of particles. The foreseen accuracy of this independent velocity measurement will enable AMS to unambiguously determine the particle mass for proton and nuclei up to tens of GeV in kinetic energy per nucleon.

- A 3-D sampling Electromagnetic Calorimeter (ECAL) made out of 16.7 X_0 of lead and scintillating fibres to accurately measure the energy of the electromagnetic component of the cosmic radiation. Based on the different energy deposit, the expected $\mathrm{e/p}$ separation of $\sim 10^4$ is expected up to the TeV energy range.

Already from this schematic description the guiding concept of multiple independent measurements of the particle properties can be appreciated. The particle absolute charge ($|Z|$) is independently measured four times in the TOF, up to eight times in the silicon TRACKER and by a different physical principle also in the RICH. The particle velocity is measured, with different accuracy, in the TOF and RICH detectors and at the same time the TRD response depends on the particle boost factor γ. The rigidity measurement in TRACKER and the energy deposit in ECAL (or TRD) can be combined to cross-calibrate the response of the two detectors and improve $\mathrm{e/p}$ separation.

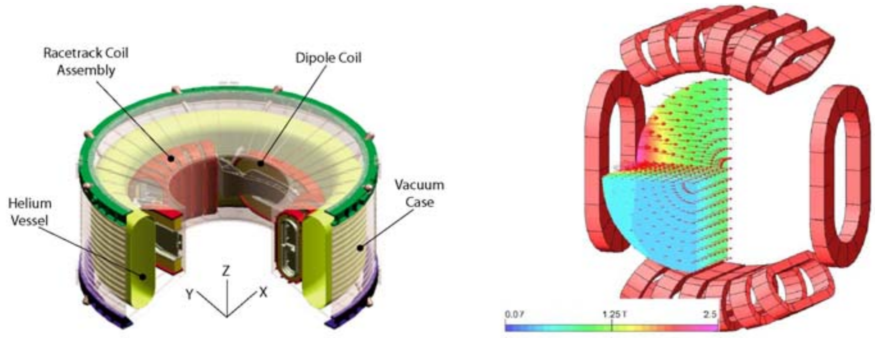

Figure 3.2: *Schematic views of the magnet system. On the left, the general layout of the components is shown. The coil arrangement and the field map representation are reported on the right*

However, the particle charge sign — which is the crucial quantity in the matter / anti-matter separation — is uniquely assigned from the TOF measurement of the particle arrival direction and the bending sign in the magnetic field, as reconstructed in the tracking device. The magnet and tracking systems are in this concern the real core of the AMS instrument, and much effort has been put in their design to get a stable and performing system, also considering the extreme conditions of space environment. To ensure that the detector can withstand the tremendous mechanical stress of the launch, the large orbital temperature changes from -65 to 40 °C and the intense radiation background, a prototype performed an engineering flight on the Space Shuttle prior to the installation on ISS. This mission will be referred to as AMS-01 in the following [102, 115, 124].

3.2 The magnet

The magnet system, as shown in figure 3.2, consists of 14 coils of niobium titanium (NbTi) filaments, which work in the superconducting regime as long as the temperature is kept below 4.0 K: a copper / alluminium coating is used to facilitate the cooling of the filaments [125, 126], which greatly reduces the probability of quenching events.

The coils are arranged around the inner cylinder of the vacuum tank in such a way that the generated dipole field is oriented perpendicular to the detector axis. More precisely, the single pair of large coils generates the 0.86 T magnetic dipole field, while the twelve smaller coils, besides contributing to the dipole definition, act as the return yoke, controlling the stray field intensity. The containment of the magnet field is an important safety issue since the stray field would interact with the geomagnetic one, therefore applying to the ISS a torque.

The magnet operates at a temperature of 1.8 K, cooled by a cryogenic system based on the employment as cryogenic fluid of 2500 litres of helium in superfluid regime, which is stored inside a dedicated toroidal vessel. The whole system is enclosed by a quadruple thermal shield and a vacuum tank, to limit thermal conduction from the outside.

Because of the parasitic heat loads, the helium will gradually boil away throughout the lifetime of the experiment, and as it will be used up, the magnet will warm up

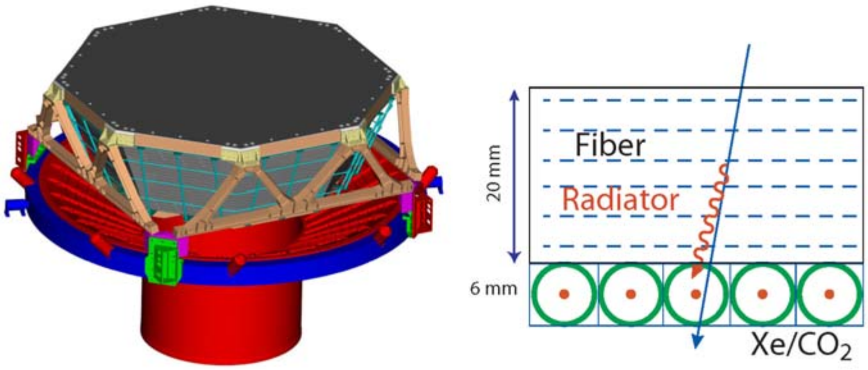

Figure 3.3: *Schematic view of the* TRD *on top of the magnetic case (left) and operating principle of the* AMS TRD *detector (right)*

and will be no longer operable: to increase the duration of the experiment, the He vapours are extracted from the vessel by a special zero-gravity passive phase separator (PPS) [127] and reused to refrigerate the thermal shields: this allows to achieve a design operating time of 3 to 5 years for the magnet system and the experiment as a whole.

The magnet will be launched at the operating temperature, with the vessel full of superfluid helium, but with no current circulating in the coils. It will be charged only after the successful installation of the experiment on the ISS.

3.3 The Transition Radiation Detector

Transition radiation is the electromagnetic radiation emitted when charged particles transverse the boundary between two media with different dielectric properties [128]. Even if the probability for a particle to emit a TR photon at a single interface is relatively small ($\mathcal{O}(10^{-2})$) the use of a multi layer structure can significantly enhance the photon yield and result in a detectable signal.

In AMS, TR photons are generated in twenty layers of fleece radiator (polypropylene / polyethylene) interleaved with straw tubes which detect their signal. The detection principle, as well as the TRD structure on top of the magnet vacuum case, are presented in figure 3.3.

The use of the fleece radiator enhances the single layer emission since the impinging particle goes through the several fibres that constitute the fleece itself, thus actually trespassing many dielectric interfaces in the single radiator module. Another improvement with respect to more classical designs is represented by the straw tubes being homogeneously distributed among the radiator, removing the necessity of an external detector for the emitted photons. Furthermore, the constituent modules (In total 328, each containing 16 straw tubes) are supported by a conical octagonal aluminium-honeycomb / carbon-fibre structure, such that the lower and upper four layers are oriented parallel to the AMS-02 magnetic field while the middle 12 layers run perpendicular to provide the detector with 3D tracking capabilities.

To verify the e/p separation performances of the AMS TRD, system a full 20 layer prototype has been exposed to the CERN T9, X7 and H6 beam lines to record electrons,

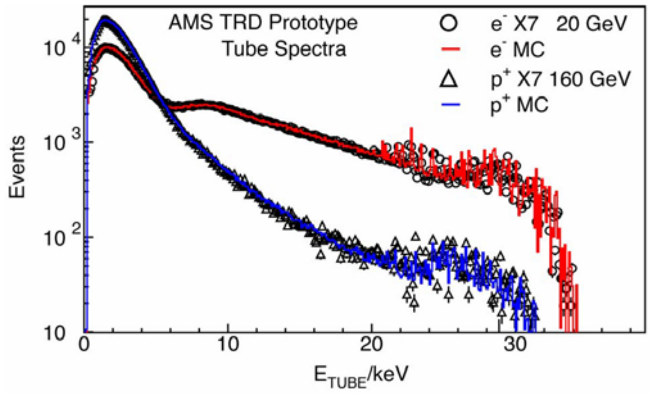

Figure 3.4: Single track energy spectra as measured for electrons and protons in a TRD *tube. The larger energy deposit, due to the* TR *photons, is clearly evident for electrons.*

muons and pions up to energies of $100\ \mathrm{GeV}$ and protons at energies up to $250\ \mathrm{GeV}$ [129]. The energy spectra measured for all wires in isolated track events are reported in figure 3.4: for both protons and electrons the $\mathrm{dE}/\,\mathrm{d}x$ peak at $\sim 2\ \mathrm{keV}$ is clearly seen. However, for electrons the signal enhancement above $\sim 6\ \mathrm{keV}$ due to the radiated photon is evident. These results have been used in order to tune the Monte Carlo description of the detector response.

3.4 The Time of Flight

The Time of Flight (TOF) system design is based on the experience gained with the AMS-01 detector [130]; as in the former case it is composed of four approximately circular planes of $12\ \mathrm{cm}$ wide and $1\ \mathrm{cm}$ thick scintillator paddles, one pair of planes above the magnet (the upper TOF) and the other pair below (the lower TOF). Each plane has a sensitive area of $\sim 1.2\ \mathrm{m}^2$ and, within each plane, the paddles are partially overlapped to avoid geometrical inefficiencies. Adjacent planes are disposed so that their paddles run in mutually perpendicular directions, as shown in figure 3.5. This arrangement has been chosen in order to optimise background rejection at trigger level and to help in offline track reconstruction, providing an estimate of the positions where the particle enters and leaves the volume occupied by the inner TRACKER. Each paddle is instrumented with two or three Photomultiplier Tubes (PMTs) at each end. The main modification with respect to AMS-01 concerns the readout light guides, that had to be curved in order to align the PMTs to the stray magnetic field, which in the proximity of the TOF system is still intense enough to influence the PMT performance significantly.

The TOF system features a very fast and reliable response to the energy loss of charged particles, well suited to provide the general data acquisition system with the fast trigger signal, used as reference time for the event. The overlapping and crossed paddle geometry allows a spatial granularity of about $12 \times 12\ \mathrm{cm}^2$, with a $\sim 100\%$ efficiency and a gate of $50\ \mathrm{ns}$ for trigger purposes.

The design resolution in the time of flight measurement is $\sim 120\ \mathrm{ps}$, with a capability of discrimination between downward / upward going particles at the level of 10^{-9}.

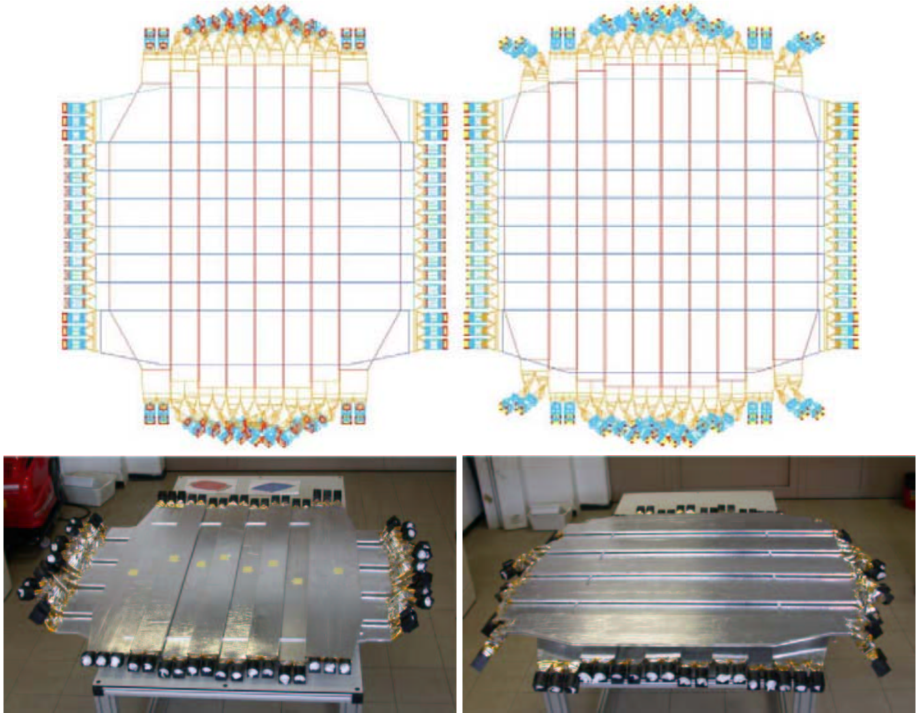

Figure 3.5: Top Panel: Schematic design of the upper (left) and lower (right) TOF planes. Bottom Panel: Assembled paddles on the upper (left) and lower (right) TOF planes

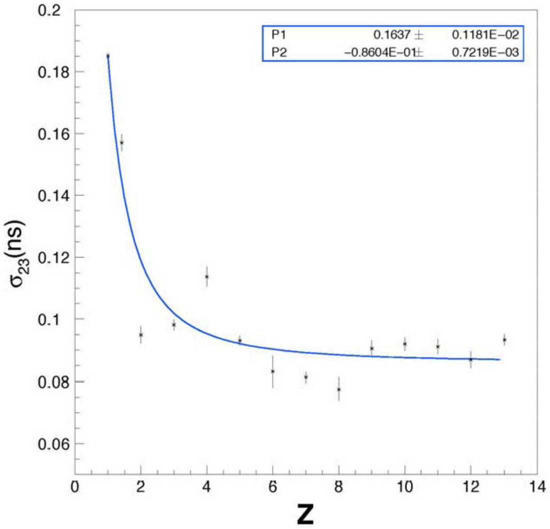

Figure 3.6: Time of flight resolution as a function of the ion charge for a pair of TOF counters as measured during beam test.

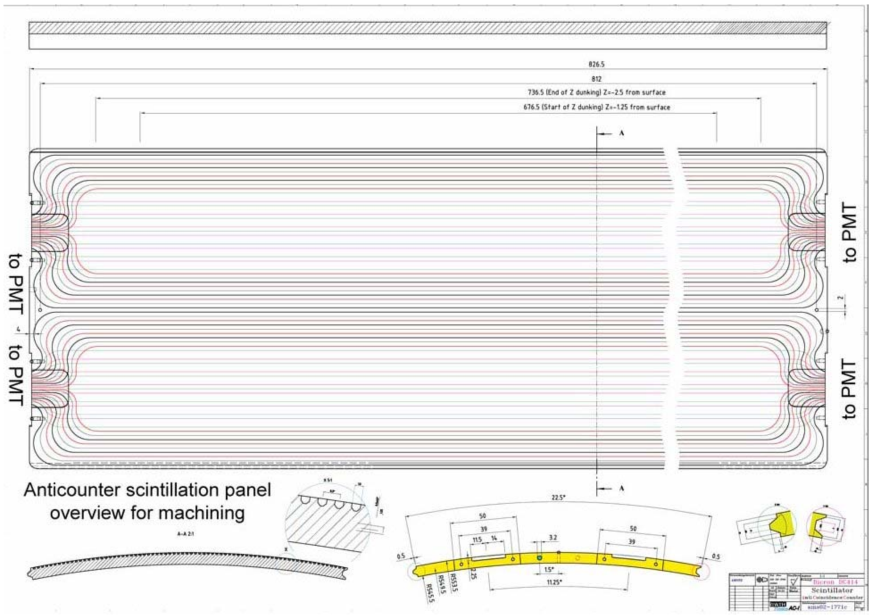

Figure 3.7: *Anti-counter scintillation panel drawing. The edges are dovetailed to ensure that no dead space is left.*

The TOF counters were tested in ion beams at CERN in 2002 and 2003. The time of flight measurements between counter pairs resulting from the beam test are in good agreement with the expected ones for ions with $|Z| \geqslant 2$, while for $|Z| = 1$ species we observe a performance degradation due to the use of the curved light guides: the TOF resolution is shown in figure 3.6 as a function of the impinging ion charge.

3.5 The Anticoincidence counters

The ACC system consists of 16 scintillation panels (BICRON BC414) of $8\ \mathrm{mm}$ thickness that cover completely the side wall of the tracking volume. Each paddle is $220\ \mathrm{mm}$ wide, and are placed side to side by means of dovetail joints to completely avoid geometrical inefficiencies. A technical drawing of a paddle is shown in figure 3.7. Since the ACC will be located inside the magnetic field, the readout PMTs cannot be placed in direct contact with the paddles; a wavelength-shifting fibres system is used instead to route the scintillation signals out of the tracking volume, where the PMTs are oriented along the residual stray field lines ($\sim 1.2\ \mathrm{kG}$).

The fibres, of $1\ \mathrm{mm}$ diameter, are embedded inside grooves milled into the scintillation panels and are collected into two output ports of 37 fibres each at both ends of the counters: a detail of the fibres output can be seen in figure 3.8. Just out of the tracking volume, the wavelength-shifter fibres are matched to clear fibres that route the collected photoelectrons to the PMT located near the outer end of the magnet vacuum vessel, as shown in figure 3.9.

This sub-detector is necessary to ensure that no particles enter the tracking volume from the sides; in such cases the hits due to the laterally impinging particles are likely

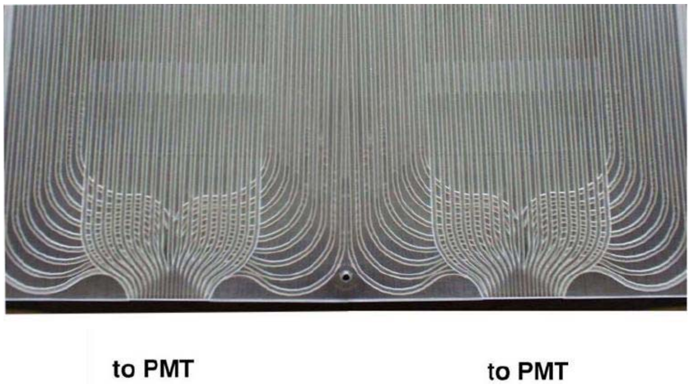

Figure 3.8: *Detail of a finished* ACC *panel end: the two readout groups of wavelength-shifter fibres can be seen clearly.*

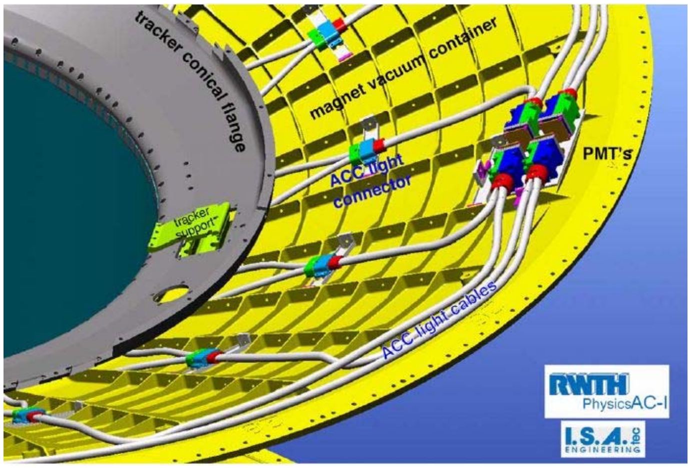

Figure 3.9: ACC *light transport system, from the fibres embedded in the panels, through the couplings to the* PMTs *located on the outer rim of the vacuum case.*

to produce both a wrong measurement of the charge and a defective track reconstruction. The ACC signals are therefore included as veto into the trigger logic.

The performance of the ACC system has also been tested under a 10 GeV proton beam at CERN in 2003, showing no inefficiencies in a sample of 350,000 events: with such performance on the part of the ACC it is reasonable that signals will not be simulated by laterally entering particles.

3.6 The Ring Imaging Čerenkov Detector

Designed to give an independent and more accurate measurement of the particles velocities, the RICH is placed on the lower part of the spectrometer, between the lower TOF and the Electromagnetic Calorimeter.

As shown in the schematic view of its main structural components presented in figure 3.10,the RICH has a truncated conical shape with $60(67)$ cm upper(lower) radius and an height of 47 cm. On the top is located a supporting plate that holds a 3 cm thick layer of dielectric material (radiator) while the lower plane supports an array of 680 light guides and PMTs, as well as the front-end electronic board.

The radiator is made out of tiles of two different materials: in the external part are used tiles of *silica aerogel*, while a central square area of 34×34 cm^2 is equipped with NaF ones 0.5 cm thick. The aerogel is a mixture of $m(SiO^2)$ and $2m(H^2O)$, with m an integer, and has a porous structure with bubbles, most of them of small size compared to optical wavelengths. The refractive index is an average between the ones of air and the mixture and can therefore be tuned to the needs of the detector (n=1.03÷1.05). The NaF that constitutes the central blocks of the radiator, has an higher refractive index (n=1.336) and gives a wider Čerenkov cone. This allows to leave a 64×64 cm^2 zone in the detection plane where no PMTs are present to let particles go unaffected to the ECAL; in fact the interaction of the impinging particles with the PMT would deteriorate the performance of the ECAL, whereas the thin layer of radiator does not constitute a concern.

A charged particle coming from above first crosses the radiator, creating a cone of Čerenkov radiation. Most of the photons go directly to the photon detectors on the lower plane. The other photons are reflected on the lateral surface of the cone and also directed to the photon detectors. At the lower plane, the photon detectors have light guides attached to the PMTs. From the spatial coordinates of the photomultiplier pixels, and the direction of the incoming particle, the Čerenkov cone is reconstructed and the velocity of the particle determined. Upward going particles do not leave signal in the RICH, and thus can be unambiguously discriminated.

In order to validate the detector design, the performance of a RICH prototype has been tested with cosmic muons and with an ion beam at CERN [131, 132, 133]. In figure 3.11 the measured velocity resolution as a function of the ion charge is shown.

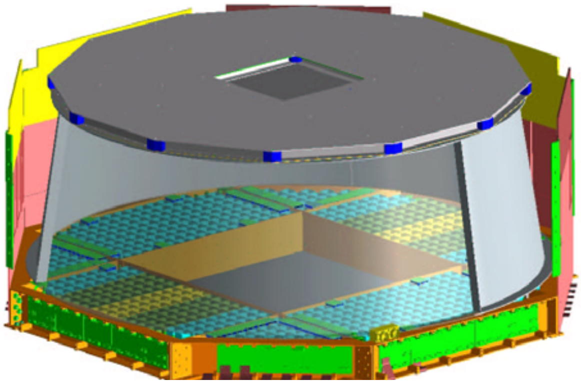

Figure 3.10: *The main structural components of the* RICH *detector*

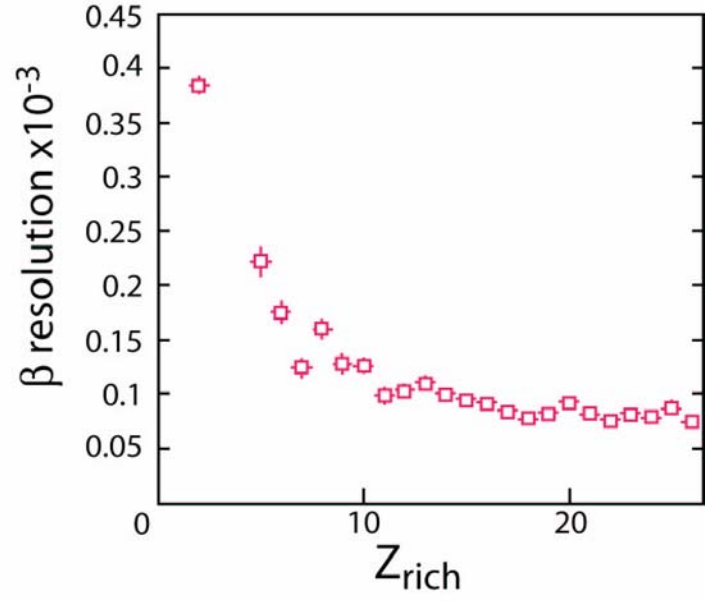

Figure 3.11: *Dependence of the velocity resolution on the charge of the nuclei as obtained with* RICH *prototype in a beam test*

3.7 The Electromagnetic Calorimeter

The Electromagnetic Calorimeter is a fine grained lead-scintillating fibre sampling calorimeter designed to perform a precise 3-D imaging of the longitudinal and lateral shower development [134,135], providing high (10^6) electron / hadron discrimination in combination with the other AMS-02 detectors and good energy resolution. The calorimeter also provides a standalone photon trigger capability to AMS.

The calorimeter is composed from superlayers, each 18.5 mm thick and made of 11 grooved lead foils interleaved with scintillating fibres and glued together with epoxy: both the foil thickness and fibre diameter amount to 1 mm. The resulting composite structure, shown in figure 3.12, has an active area of $648 \times 648\ \mathrm{mm}^2$ and a thickness of 166.5 mm, that corresponds to ~ 17 radiation lengths, for a total weight of 496 kg.

Since in each superlayer, fibres run in one direction only, the detector imaging capability is obtained by stacking superlayers with fibres alternatively parallel to the x-axis (4 layers) and y-axis (5 layers), as shown in the lower part of figure 3.12.

Each superlayer is read out by 36 four anode PMTs, arranged alternatively on the two opposite ends in order to read out each fibre without any dead zone in the detection geometry. The effective readout granularity is not given by the distance between two neighbouring fibres, because each PMT collects the information from a group of 35 fibres, that form a readout cell (put in evidence in figure 3.12) of size $9 \times 9\ \mathrm{mm}^2$ that is half the superlayer thickness.

To realistically assess the ECAL performances and validate the concept design, a qualification model of the ECAL has been exposed to the CERN SPS beam line H6A with muons, 120 GeV protons and anti-protons and $\mathrm{e}^{\pm}$ with energies in the range $3 \div 180$ GeV.

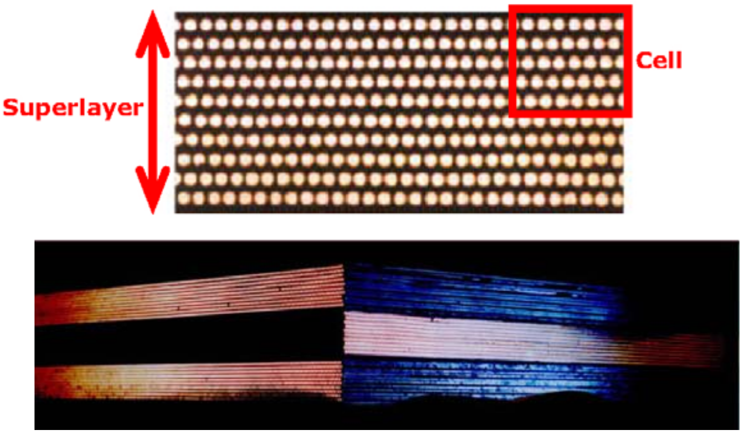

Figure 3.12: *Top: Cross section of the* ECAL *lead-fibre-glue composite structure, Bottom: Three assembled superlayers*

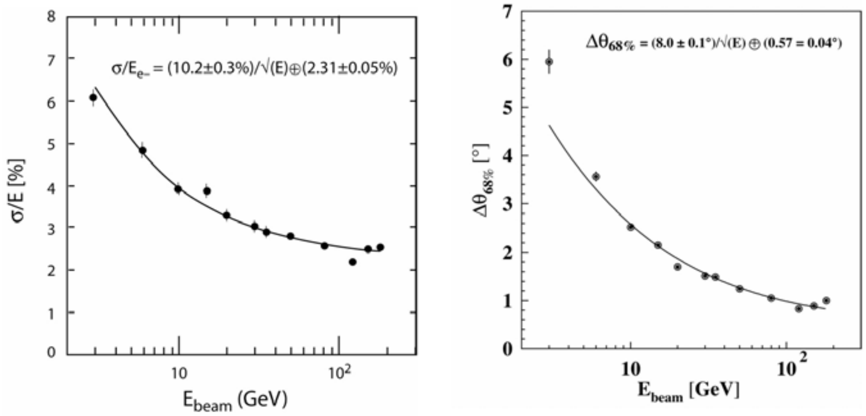

Figure 3.13: *Fractional uncertainty in the energy (left) and incident particle direction (right) measurements of* ECAL *for different electron beam energies. The curves corresponds to the fitted parametrisation.*

The shower shape (lateral and longitudinal shower development) and energy leakage analysis have been carried on the beam test data as a function of the beam energy, for different geometry of the interactions and nature of the incident particles. As a result, the effective radiation length, the energy and angular resolution as well as the electron / hadron discrimination have been estimated to behave according to the ECAL design. In figure 3.13 the measured angular and energy resolutions for electrons are presented as a function of the particle energy.

3.8 The Silicon Tracker

The AMS-01 silicon TRACKER [136, 137, 138] was the first application in space of the high precision silicon technology developed for position measurements in accelerator experiments [139, 140]. The high modularity, the low voltage levels (< 100 V) and the gas-free operation of the device are well suited to operation in space. The 1998 shuttle test flight demonstrated both the successful adaptation of the technology to the space environment and the feasibility of large area detectors.

The TRACKER is built of $41.360 \times 72.045 \times 0.300$ mm^3 double sided micro strip sensors. In figure 3.14 the schematic of one sensor layout is shown; it consists of a high resistivity n-type bulk, with p^+ and n^+ strip implantations running in orthogonal directions on the opposite faces of the sensor, with an inter-strip implantation (readout) pitch of $27.5\,(110)$ µm and $104\,(208)$ µm for the p and n side respectively. The finer pitch p-side strips are used to measure the bending coordinate corresponding the y axis in AMS reference frame, while the orthogonal n-side strips measure the x coordinate.

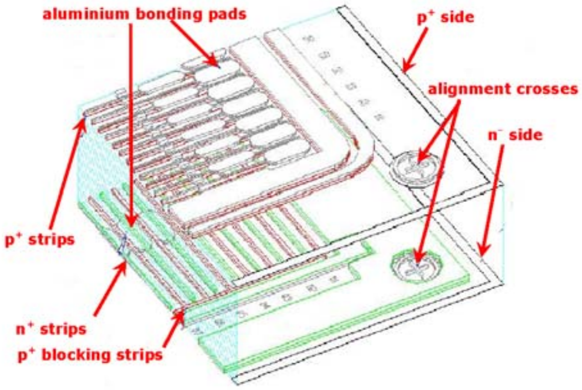

Figure 3.14: *Layout of the double-sided micro strip sensor*

The ionisation loss of singly charged particles traversing the fully depleted, reverse-biased 300 µm sensor, is described by a Landau distribution, with the peak signal given by the specific $\mathrm{dE}/\mathrm{d}x$ of the particle in silicon as resulting from the *Bethe-Bloch* parametrisation. This results in a peak energy loss for a minimum ionising particle which corresponds to the generation of ~ 22000 hole electron pairs in the silicon. Due to the reverse bias applied to the sensor using the punch-through mechanism, the holes (electrons) drift rapidly ($10 - 25$ ns) to the p (n) surfaces where the accumulated charges on the readout strips is fed to the front-end electronics. The particle position is determined by the relative signal levels observed at the readout strip positions. At the single sensor level, the position resolution is determined by the sampling pitch and the signal-to-noise performance.

The silicon sensors are grouped together, for readout and biasing, in modules (called *ladders*) of different lengths to match the cylindrical geometry of the TRACKER. In figure 3.15 the principal components of a ladder (left) and a pair of assembled ladders (lower right) are shown. The p strips are running through the entire length of the ladder.

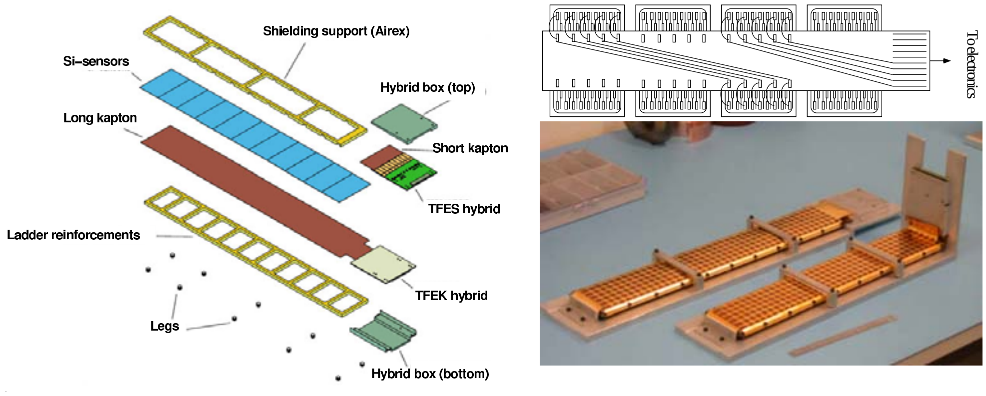

Figure 3.15: *Left: the principal components of the silicon ladder. Upper right: bonding scheme for the n-side strips. Lower right: two ladders ready to be mounted on the support plane .*

To minimise the amount of material in the sensitive region of the detector and reduce the geometric inefficiencies, the front-end electronics (the hybrids) is located at the end of the ladder, and a metalized kapton cable is used to route the n-side signals to the ladder end. The bonding scheme necessary to read out all of the sensors on their n-side, is also displayed in the upper right part of figure 3.15: this kind of connection introduces an ambiguity on the determination of the x coordinate that must be solved during the reconstruction phase using the spatial information provided by the TOF system.

The silicon sensors of each ladder are held by a 5 mm thick foam support that is glued to the n-side kapton cable; the exposed surface of the foam is covered with a 100 μm thick layer of carbon fibre. Small aluminium frames are glued to the carbon fibre surface and are provided with screw fixation holes to attach the ladder on the mechanical structure of a plane.

Figure 3.16 shows a sketch of the plane geometry inside the tracking volume (left) as well as the photograph of one plane after completion of ladder mounting (right). The two outermost planes, placed just above(below) the magnet structure, are equipped with a single layer of ladders. The three innermost planes, are equipped with double layers of ladders, for a total of eight measurements along the particle trajectory. Such configuration, based on the experience with the AMS-01 flight, minimises the uncertainties on rigidity measurements due to interactions in the detector material.

The maximum combined strip length in the silicon for a single readout channel is

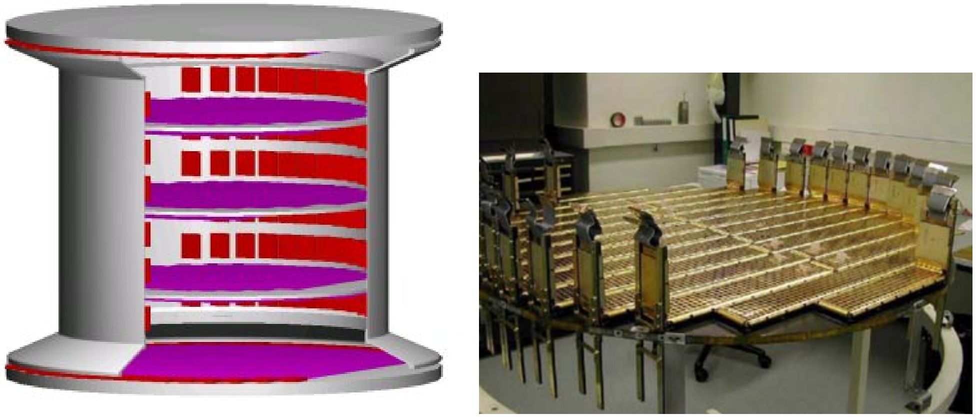

Figure 3.16: *Geometry of the* TRACKER *planes (left). Plane number 2 completely equipped with ladders (right)*

$60\,\mathrm{cm}$, corresponding to the 15 sensors used in the central ladders of the outermost planes. The relatively large input capacitance ($30-180\,\mathrm{pF}$), as well as the need for a high dynamic range[2], led to the development of a new front-end readout chip based on the low-noise Viking design, the VA-hdr [141].

Each of the 64 channels of the VA chip consists of a charge sensitive amplifier, a Gaussian shaper and a sample and hold stage. An analog multiplexer, shift register and buffer are incorporated in the chip for sequential data output at a maximum clock frequency of $\sim 10\,\mathrm{MHz}$. The strips of the silicon sensors are AC-coupled to the VA via $700\,\mathrm{pF}$ capacitor chips. Both the VA and the capacitors are housed on the hybrid Tracker Front End board.

Each ladder is read out by 16 (10p +6n) VA for a total of $196,608$ readout channels, corresponding to $\sim 3\,\mathrm{Mbit}$ raw data per event. Data compression is therefore mandatory in order to keep manageable the event size for the acquisition. This task is performed by a set of Tracker Data Reduction (TRD) boards, each of whom processes the signal sequentially read from one ladder. Calibration runs are regularly performed to monitor the average signal level of each channel in absence of energy deposit (pedestal) and its spread (noise). A compression algorithm running on the TRD Digital Signal Processor is used to select channels where the pedestal subtracted signal level is greater than three times its characteristic noise. Neighbour channels are also readout in order to allow a more accurate position measurement.

Critical issues in the design, construction and operation of the TRACKER are the mechanical and thermal stability of the instrument. A position measurement at the $10(30)\,\mu\mathrm{m}$ level, relies on a knowledge of the single sensor position inside the TRACKER of the same order. This is insured *ab origine* by the precision of the jigs used to hold the sensors during the assembly, and the precision of the sensor cut. During fabrication, the sensor positions on the ladders and of ladders on a plane, are recorded with a 3D semiautomatic measuring machine using special crosses marked at the sensor surface as a reference (see details in figure 3.14). The results for the sensor alignment on 125

---

[2] Energy loss in silicon is proportional to Z^2, so that a dynamic range up to $\sim$ 1000 the proton signal is needed

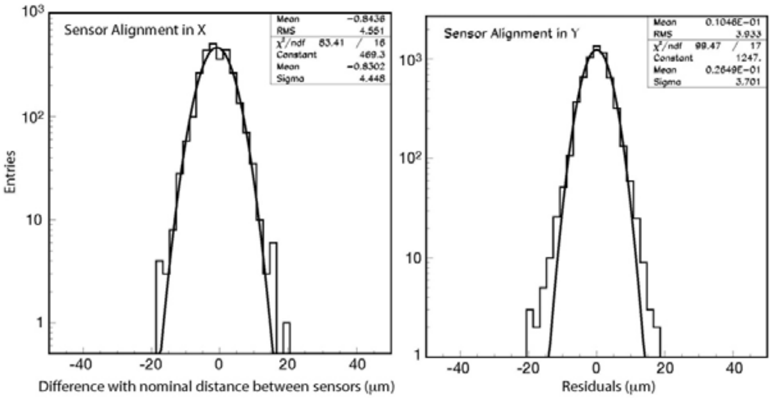

Figure 3.17: *Assembly precision of 125 ladders: distribution of the measured differences of the distance between adjacent sensors and the nominal distance (left) and the residual distribution of the sensors positions about the line fits defining the ladder axis parallel to the magnetic field (right)*

(out of the total 192) ladders are reported in figure 3.17.

The mechanical structure of the planes and the cylindrical shell which constitutes the TRACKER support are both made of carbon fibre, which insures a mechanical stability of the TRACKER at the $15\ \mu\mathrm{m}$ level even in front of vibrations during detector deployment and the tremendous amount of mechanical stress during the launch. Moreover, based on the experience of the AMS-01 mission, thermal excursions due to orbital attitude changes can influence the system alignment up to tens of microns. A laser alignment system is therefore implemented, which allows a continuous long term monitoring of relative displacements of the TRACKER planes.

Temperature variations along the orbit can also reflect on the intrinsic noise of the sensors, changing the efficiency in the minimum ionising particle signal detection and/or leading to spurious hits in the system. Moreover, since the TRACKER is embedded in the magnet system, which has to be efficiently and stably kept at a low temperature, a thermal control of the TRACKER is also needed to exhaust — out of the magnet system — the heat produced by the detector, mainly in its readout electronics.

In fact, even if the hybrids are mounted on carbon fibre-metal cooling bars, which conductively evacuate the heat generated inside the magnet, this is not enough for the magnet thermal needs. An active cooling system for the TRACKER, based on a two-phase mechanically pumped loop is being developed. The cooling liquid, $\mathrm{CO_2}$ at about $80\ \mathrm{bar}$ pressure, is circulated by a pump. It enters the TRACKER volume at a temperature just below the boiling point, and passes by thermal bars on the outermost and innermost planes, where the heat from front-end hybrids is collected in series. At each input, a small fraction of the fluid is evaporated. The presence of two loops, on the upper and lower plane of the TRACKER, allows an homogeneous cooling of the TRACKER with a minimum amount of material in the tracking volume. In figure 3.18 the locations of the principal elements of the TRACKER thermal control system are shown (top) as well as the details and the prototypes of evaporator rings (bottom).

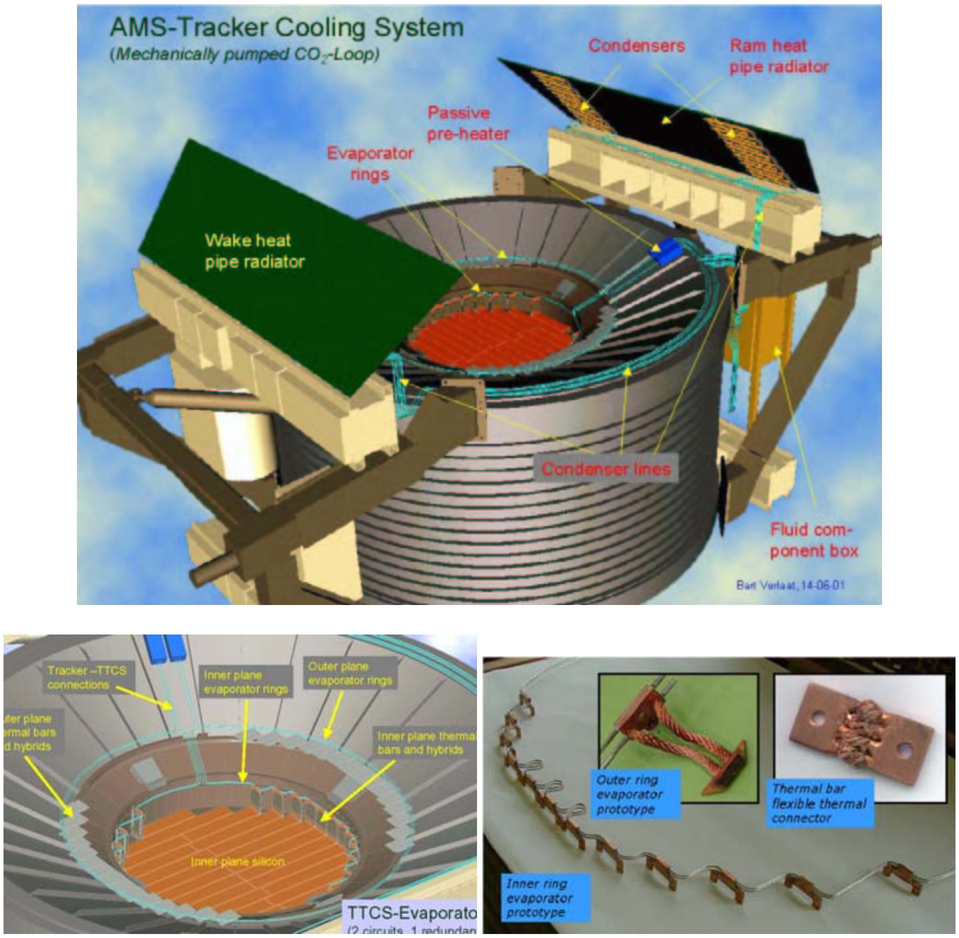

Figure 3.18: *Top: Locations of the principal elements of the* TRACKER *thermal control system. Bottom left: Evaporator installation details. Bottom right: Evaporator prototypes*

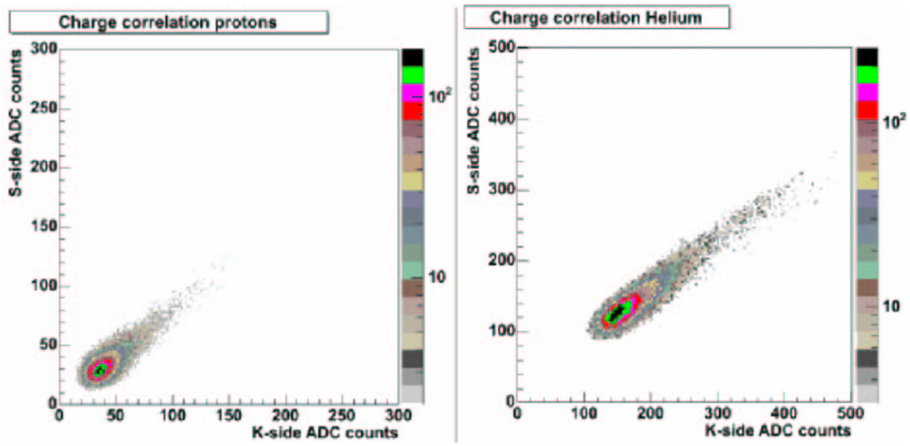

Figure 3.19: *Total cluster energy as measured on the p and K sides of the same ladder for protons (left) and helium (right) nuclei*

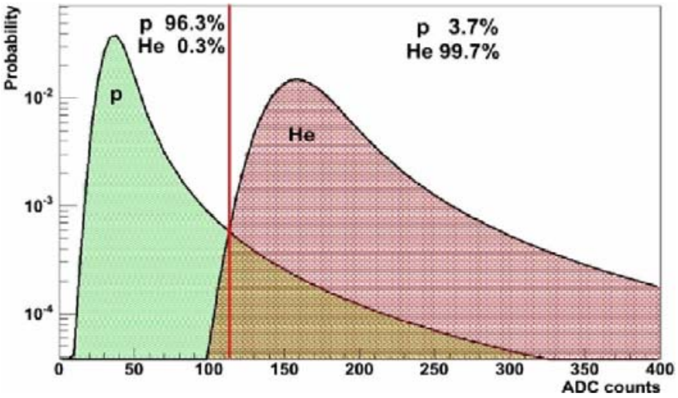

Figure 3.20: *Probability density functions for proton and helium signals on a ladder p-side.*

3.8.1 Charge determination with the Si TRACKER

The TRACKER capability to measure the particle $|Z|$ through its ionisation energy loss, allows the identification of the various nuclei species found in the Cosmic Rayss. Due to the quadratic dependence on the charge of $\mathrm{dE}/\mathrm{d}x$, the readout electronics must have an appropriate dynamic range to measure the charge of nuclei beyond carbon. The VA-hdr chip has been chosen in the front-end readout in order to get an extended range in the energy loss measurement, while keeping a good signal to noise ratio for minimum ionising particles.

Ion beams have been used to verify the ladder performances and study their response to different nuclei. In figure 3.19 the total cluster energy measured on the p and n-side of the same ladder, is shown for $Z = 1$ and $Z = 2$ particles. A good correlation between the signals is evident; furthermore the distributions related to the two Z values are well separated, allowing a quite accurate distinction between $Z = 1$ and $Z = 2$

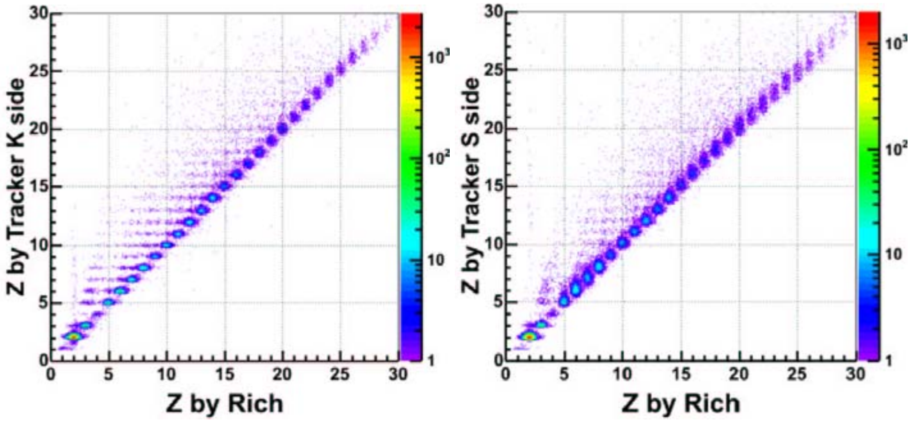

Figure 3.21: *Comparison of charge (Z) measurements by* TRACKER *and* RICH*, as obtained in beam test*

species already with a single ladder measurement. Since the ionisation energy release is ruled by the Landau distribution it is unlikely that He nuclei may be mistaken for lower charge species, however there is still the possibility to make the opposite error. This would be an undesired background for the primordial anti-He nuclei search.

In figure 3.20 are shown the probability density functions of the energy release in ADC counts measured in the test beam for both protons and He nuclei; using the value marked by the red vertical line in figure 3.20 as an identification criterion would allow only 0.3% of the He nuclei to contaminate the lower charge distribution which on the contrary is overlapping the helium one by almost 4%. However these two distributions refer to a single charge measurements, whereas the TRACKER provides up to eight independent determinations for each particle. A Monte Carlo study on the p/He separation capability of the AMS apparatus was performed over a generated sample of 10^8 protons and 10^8 He nuclei.

Using all the eight measurements, no helium was mistaken for a proton over the whole sample, yielding a separation power of $\sim 10^{-8}$. It should be noticed that while the TRACKER may miss some measurement due to inefficiencies, the charge is also independently measured at least three times by the TOF— due to the trigger condition that we discuss in the next chapter — and another may also be available from the RICH; these additional measurements can be used to improve the resolution of the TRACKER itself.

In fact, the charge measured by the different sub-systems where also compared during the test beams: in figure 3.21 are reported as examples the correlation plots among the charge measured in the p (left) and n (right) side of a ladder the one determined using a RICH prototype exposed to the same beam.

There is a clear correlation between the ladder and RICH measurements up to very high ion charges: the off-diagonal points are due to the spallation products of the beam ions in the material between the TRACKER and RICH prototype. From these plots we can also see how AMS is able to distinguish ion charges up to the iron one ($Z = 26$).

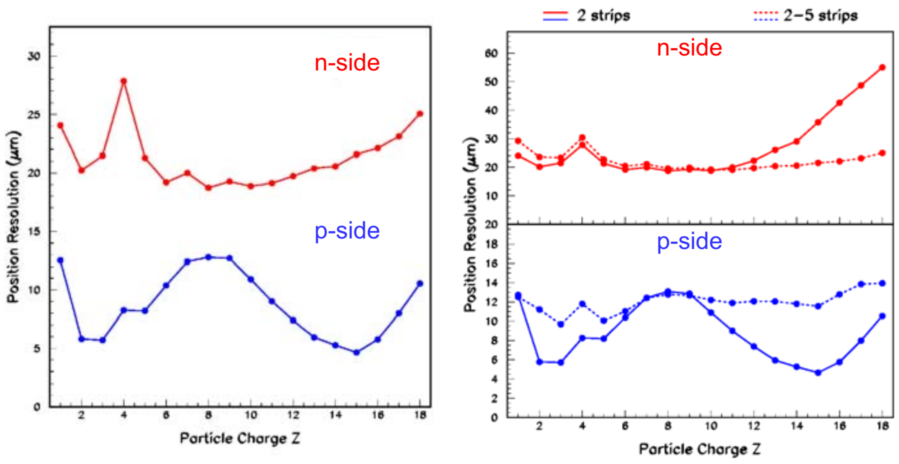

Figure 3.22: *Resolution of the position measurement as a function of the ion charge in the bending (p-side) and non bending (n-side) coordinates. In the right panel, the same distributions are presented for different algorithms used in the definition of the reconstructed coordinate.*

3.8.2 Spatial resolution with the Si TRACKER

Besides measuring the particle charge modulus, the TRACKER performs the essential task of measuring the particle trajectory in the magnetic field, in order to determine from its radius of curvature the rigidity defined as $\mathrm{R} = \mathrm{P}/Z$; this allows to recover the particle momentum and mass when combined with the measures of $|Z|$ and β. The spatial resolution of the TRACKER is a crucial parameter for the detector since a smaller value of resolution would allow a more accurate measurement of the rigidity over a wider range. The beam tests carried out to determine the charge measurement capabilities of the spectrometer, have also been used in order to study the position measurement accuracy for different ions species. The results are presented in figure 3.22 where the position resolution in the two coordinates is shown as a function of the ion charge.

The spatial resolution is in the range $6 \div 13$ μm for the p-side and ~ 21 μm for the n-side. This difference is essentially due to the larger implantation width and readout pitch of the n-side strips, as well as to the fact that the charge collection mechanism on the n-side is not ruled by the same capacitive coupling of the p-side; moreover the n-side is generally more noisy since its reference potential is the floating high voltage level of the bias (~ 80 V).

The spatial resolution plots reported in the right panel of figure 3.22 show how different algorithms for the evaluation of the particle impact position may influence the value of spatial resolution: on either the p and n side using more neighbouring strips for the calculation, produces a resolution that is more uniform over the different ion charges, however on the p-side this means that the average value increases to ~ 11 μm. In any case, the achieved spatial resolution allows for a maximum detectable rigidity of order $\mathcal{O}$(TV).

In figure 3.23 is shown the tracker rigidity resolution we evaluated from the official AMS Monte Carlo data, applying the selection criteria that we describe in detail in chapter 5. The resolution is better than 2% in the range $1 \div 40$ GeV; out of this interval

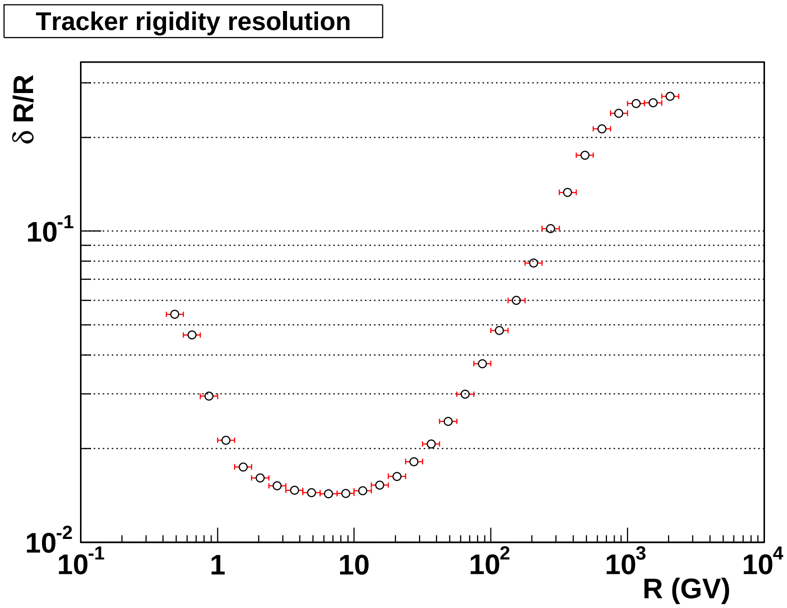

Figure 3.23: Tracker rigidity resolution as evaluated from the official MC *data applying the analysis that will be described in chapter 5.*

the resolution worsens, due to Coulomb scattering towards low momenta and to the finite value of spatial resolution for high ones.

Chapter 4

The Monte Carlo Simulation

The AMS-02 detector response to the passage of charged CR is evaluated by means of a simulation program, based on the GEANT package [142]. Mechanical drawings and measurements during the assembly are used to describe in details the detector geometry. The GEANT package is then used to simulate the energy deposit and interactions of incident particles within the different detectors. Physical signals are then converted in the equivalent experimental signals and the event reconstruction proceeds as it would do for real data. The final output of the full simulation is a compressed data file, using the ROOT framework [143]. It contains the original Monte Carlo record of the generated particle, the kinematical parameters of the particle reconstructed in the different sub-detectors, as well as the relevant sub-detector signals registered in the event.

In this chapter, we will review the different topics of the AMS Monte Carlo simulation which are more relevant for our study. Large samples of Monte Carlo events are needed for an accurate estimate of the AMS acceptance. However, due to the isotropic distribution of cosmic rays and the steep decay of their flux with energy, an efficient generation strategy and an early suppression of uninteresting events is mandatory to keep manageable the sample to analyse. We will first address this topic, as well as our implementation of a *trigger* logic in the simulation which reproduces the effects of the charged particle trigger foreseen in the AMS data taking.

We will then discuss the global event reconstruction in AMS with particular emphasis on the track fitting procedures which mostly influence the resolution in the rigidity measurement and the charge sign assignment.

We will conclude with a short description of the produced Monte Carlo samples and a discussion on the software tools developed to perform our study, currently released as a ready to use package to the AMS Collaboration.

4.1 The event generation

As a general procedure, the first step in the simulation consists in the random generation of the particle momentum according to the expected energy and spatial distribution for the physics channel under study. For our analysis we need to produce signal (anti-protons) and background (protons and electrons) particle fluxes impinging isotropically over the full detector and with the energy spectra of Cosmic Rays. However to sample with significant statistics the full energy spectrum observable with AMS, the generation process has to be carefully planned in order to prevent the total number of events to grow beyond a manageable size. The possible optimisations are connected with the choice of the spectrum to be generated and of the generation volume.

4.1.1 Probe spectrum and energy range

The CR differential energy spectra are generally described by a power law with indexes < -2.5. This would imply that to generate a significant statistics at energies above $\mathcal{O}(100\ \mathrm{GeV})$, according to its natural shape, the corresponding number of events generated in the low energy part should be several orders of magnitude larger. With this approach the total number of generated events can easily grow out of scale. However the detector response may be studied with a *probe spectrum* and the results for a different input spectrum obtained just weighting the events accordingly. The chosen *probe spectrum* follows an inverse law with energy $\mathrm{d}N/\,\mathrm{dE} \propto \mathrm{E}^{-1}$: this provides an enhancement in the event production at high energies, while keeping a larger statistical weight for the low energy part of the spectrum.

As a further optimisation of the process, the generation range was split into three sub-ranges, namely $0.5 \div 10\ \mathrm{GeV}$, $10 \div 200\ \mathrm{GeV}$ and $200 \div 1789\ \mathrm{GeV}$, where the MC production took place separately.

In our analysis, we have considered the data produced over the whole energy range $0.5 \div 1789\ \mathrm{GeV}$, studying separately the three energy intervals and combining the results according to the different statistical weights of the three samples. In the following we will always refer to these combined results.

4.1.2 The generation volume

Along with the energy spectrum, it is also necessary to simulate the isotropic spatial distribution of the CR fluxes.

This is easily obtained enclosing AMS in a volume (V) and choosing a random point on the surface of V. From that point, representing a surface element $\mathrm{d}\widehat{\sigma}$, particles are generated with an energy according to the *probe spectrum* and direction isotropically distributed towards the interior of the generation volume (i.e. covering a 2π solid angle).

The choice of the volume is arbitrary, so a cube both concentric and coaxial with AMS was used. The acceptance of one face of the cube is easily evaluated as:

$$\mathrm{A}_0(\mathrm{P}) = \frac{N(\mathrm{P})}{\Delta t \phi(\mathrm{P})} = \int_{S,\Omega} \mathrm{d}\widehat{\sigma} \cdot \mathrm{d}\widehat{\Omega} = \ell^2 \int_{\Omega} \sin\theta\cos\theta\ \mathrm{d}\theta\ \mathrm{d}\phi = -\frac{\pi\ell^2}{2}\int_0^{\pi} \mathrm{d}\cos^2\theta = \pi\ell^2 \tag{4.1}$$

where $N(\mathrm{P})$ is the number of particles with momentum P that enter the square in the time interval Δt due to the generated flux ϕ; ℓ is the cube edge length. From the third member of equation (4.1) follows that $\mathrm{A}_0(\mathrm{P})$ contains a dependence from the trajectories inclination that goes like $\sin\theta\cos\theta$, so the particle directions must be generated according to that distribution.

The acceptance of AMS is obtained multiplying that of the cube by the detection efficiency $\eta = N_{\mathrm{AMS}}/N_{gen}$, estimated as the ratio between detected and generated particles. AMS has a field of view (FOV) of about 45° around the zenith direction. Particle that are out of theFOV would hit the sides of the detector, either stopping in the large amount of material to traverse (magnet, He vessel etc.) or hitting the ACC system; these particles do not trigger AMS and can be safely ignored. As particles that enter

AMS from the bottom must traverse the structure of the ISS, they do not contain any interesting signal and are therefore rejected a priori, so they do not contribute to the detector acceptance too.

The cube edge can be set in such a way that its top plane covers the entire FOV of AMS; in this case only a fraction η_{top} of particles generated in the top plane of the cube will be accepted by the detector. It follows that we can further optimise the simulation by generating particles at the top plane of the cube only and obtain AMS acceptance as:

$$\mathrm{A}_{\mathrm{AMS}}(\mathrm{P}) = \mathrm{A}_0(\mathrm{P}) \times \frac{N_{\mathrm{AMS}}(\mathrm{P})}{N_{gen}(\mathrm{P})} = \pi\ell^2 \times \frac{N_{\mathrm{AMS}}(\mathrm{P})}{N_{top}(\mathrm{P})} = \pi\ell^2\eta_{top}\ . \tag{4.2}$$

The cube edge was set to $\ell = 3.9$ m, which is the dimension required to have the top plane FOV matching the one of AMS, thus achieving the maximum generation efficiency. From now on we will use the cube top plane acceptance $\mathrm{A}_0 = \pi\ell^2 = 47.78\ \mathrm{m}^2\mathrm{sr}$ as the base for the subsequent calculations.

4.2 Trigger simulation

In the previous section we have mentioned the number of detected particles (N_{AMS}). This notion relies on the Monte Carlo ability to determine whether a particle crossed the detector or not, however the criterion cannot be simply a geometrical one, because the point of MC is to reproduce as closely as possible the response of the simulated detector. In real operation the decision to store data depends on pre-set trigger conditions, that can only take into account the signals produced in the various subsystems by the impinging particle. In order to correctly interpret the MC data the trigger logic must be simulated too.

As a matter of fact, only events which satisfied certain criteria were stored on disk. This can be considered as the simulation of a very loose trigger, called *unbiased* trigger, which requires that at least three TOF planes out of four carry signals compatible with a charged particle (also referred to as *fast* trigger or TOFZ1 in the following discussion); in addition, events with a significant energy deposition signal in the ECAL are stored anyway.

The application of this loose criterion restricts data storage to just ≈ 2.6÷ 5.8% of the total generated sample depending on the sub-range and the particle species (for details see table 4.1). This corresponds on average to a detector acceptance of ≈ 1.2\1.8 m^2sr (0.5-10 GeV), ≈ 2.2\2.4 m^2sr (10-200 GeV) and ≈ 2.6\2.8 m^2sr $(200 \div 1789\ \mathrm{GeV})$ respectively for protons \electrons.

The request of signal in ECAL is mainly intended to allow the use of the calorimeter as a standalone detector. For the purposes of our work this operation mode is of no interest, so we will consider only events which fulfil the TOFZ1 condition.

The *unbiased* trigger acceptance is almost equal to the geometric one and operating the detector with such a trigger would allow to collect a maximum of statistics. Although during the mission a fraction of the events will be acquired with such a trigger for efficiency studies, the *unbiased* trigger would accept plenty of events marginally measured in the detector — therefore of negligible interest for physics studies — which would saturate the Data Acquisition (DAQ) of the experiment.

The average event size and the bandwidth for data retransmission to Earth limit the average DAQ rate for AMS to ~ 2 kHz, with a maximum peak rate of 2.5 kHz. A thorough simulation of flux levels during the AMS mission and the study of the corresponding acquisition rates for different trigger configurations [144, 145] have shown that the TOFZ1 condition is likely to exceed peak values of $3\,\mathrm{kHz}$. In order to allow proper operation of the experiment, the hardware implementation of the trigger logic will be required to:

a) keep the acquisition rate below $2.4 \div 2.5\,\mathrm{kHz}$, corresponding to about 75% of live time,

b) feature an almost uniform selection efficiency for properly reconstructed events of 95% or better over the whole measurable rigidity range,

c) be efficient with respect to all the species AMS will study (e, p, He, heavier nuclei and corresponding antiparticles).

The acceptance after the request of TOFZ1 is displayed in figure 4.1 as a function of generated momentum by the black circles, both for protons (on the left) and electrons (on the right). We notice the decrease of acceptance below about $10\,\mathrm{GeV}$ that is a common feature for both protons and electrons, though for the former it is steeper towards $1\,\mathrm{GeV}$. The presence of this cut-off is due to the spectrometer magnetic field, which bends the trajectories of low momentum particles to the extent that they do not reach the lower TOF.

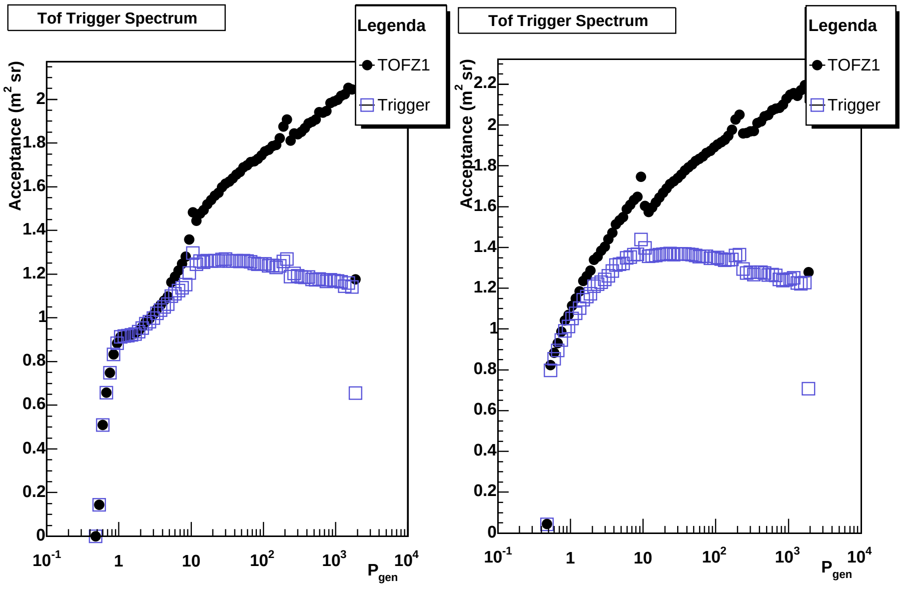

Figure 4.1: *Geometric acceptance of the detector after the simulation of different trigger logics, both for* p *(left panel) and* e^- *(right panel). The black filled circles refer to the* TOFZ1 *condition, the empty blue squares refer to the full request of equation* (4.3)*:*

4.2.1 Building the Trigger

The first thing to consider in the design of the trigger is that the TRACKER is built to measure the momentum of particles traveling in the top–plane bottom–plane direction and particles entering from the sides can confuse the reconstruction program, so we will need some condition involving the anti coincidence counters that surround the silicon TRACKER to reject those cases. The actual requirement must take into account other conditions that can influence the choice of the acceptable pattern, so we define the notation $\text{ACC}(max) =$ Number of ACC hits $\leq max$.

In the case of incident ion for instance ($Z \geq 2$), it is likely to have production of secondary particles, such as knock out electrons from the material upstream the TOF, that can cross the anti counter. In this case a reasonable constrain is that the ion itself does not come from the sides, and this can be checked imposing a condition on the energy released in the TOF planes, since the hits of a $Z \geq 2$ ion, should deposit at least four times the energy of a MIP proton [1].

If we observe in the TOF an energy deposition compatible with $Z \geq 2$ (namely $\text{E}_{dep} > 4 \div 10$ MeV) it is likely that an ion has traversed the detector in the right direction so we do not need additional conditions on the anti counters.

The condition recommended in [145] is then

$$\text{TOFZ2} = \text{TOFZ1} \wedge (\text{E}_{dep} > 7.5\ \text{GeV}).$$

If the ion condition is not met, we still require the TOFZ1, but now the anti coincidence becomes important and we must also distinguish two cases: with and without signal in the ECAL. The reason is that some of the particles from the beginning of the EM showers propagate back to the TRACKER (backsplash) and can hit the anti counters, so we cannot simply ask for ACC(0), since it would reject a great part of electron events that interact in ECAL, as is shown in figure 4.2. Proton also would be rejected in this way, but they are much less likely to interact in ECAL, and are mostly selected by other means.

To decide if an event contains a significant signal in ECAL we verify that the total energy deposited in the calorimeter is greater than a threshold. In general we can define $\text{ECAL}(\text{E}_{min}) = \text{E}_{tot} \geq \text{E}_{min}$: to produce the plots in figure 4.2 we used $\text{ECAL}(1.5\ \text{GeV})$.

To keep an high efficiency we chose the ACC() parameter in such a way that more than 95% of the well reconstructed electrons survives, which means we will use ACC(5) and ACC(2) if ECAL (1.5 GeV) is met or unfulfilled respectively.

Putting all together, the trigger we intend to simulate in our analysis is

$$\text{TOFZ1} \wedge ((\text{ECAL}(1.5\ \text{GeV}) \wedge \text{ACC}(5)) \vee (\neg\text{ECAL}(1.5\ \text{GeV}) \wedge \text{ACC}(2))) \vee \text{TOFZ2} \tag{4.3}$$

The simulation of reference [145], using a slightly different trigger “setup”, obtained rates below the critical threshold for almost all the period up to 2007 (figure 4.3). Our implementation is slightly more permissive in the article of protons, which come mainly from events without ECAL, but this should not be a problem, given that the regions where the rate exceeds the threshold are characterised by $\theta_M \simeq 1.15$, which is a marginal fraction of the AMS orbit envelope shown in figure 4.4 and a more restrictive trigger condition can be scheduled for the short time intervals in which AMS crosses them (just like for the South Atlantic Anomaly).

The effect of our trigger simulation is shown in figure 4.1 by the empty markers. We can notice that our trigger requests are mostly effective as the energy of the incident particle increases, discarding events where the incident protons are interacting in the detector material. Above the low energy threshold, an average acceptance of about

---

[1] This part of the trigger is not a concern for our purposes, but it is detailed for completeness.

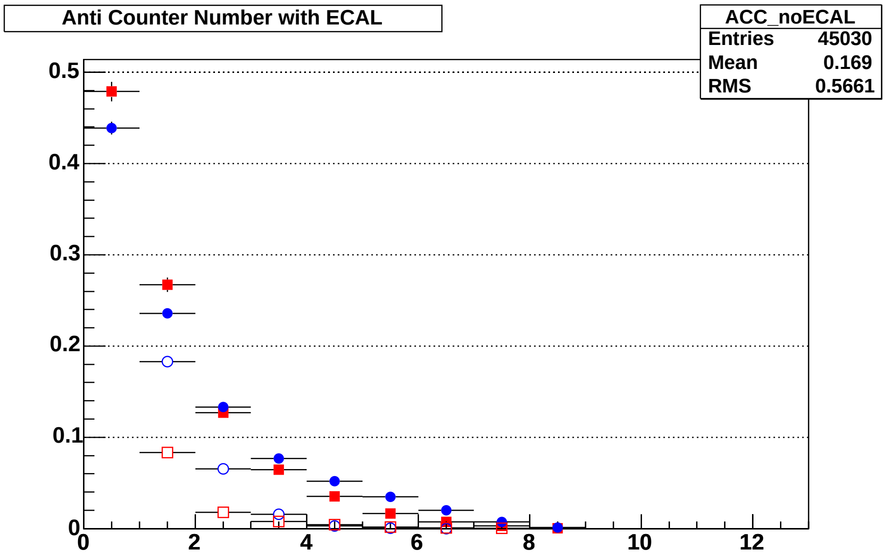

Figure 4.2: *Number of anti Coincidence Counter hits in for electrons and protons that do not enter the* ECAL *(empty circles and squares resp.) and for those traversing* ECAL*. (solid circles and squares)*

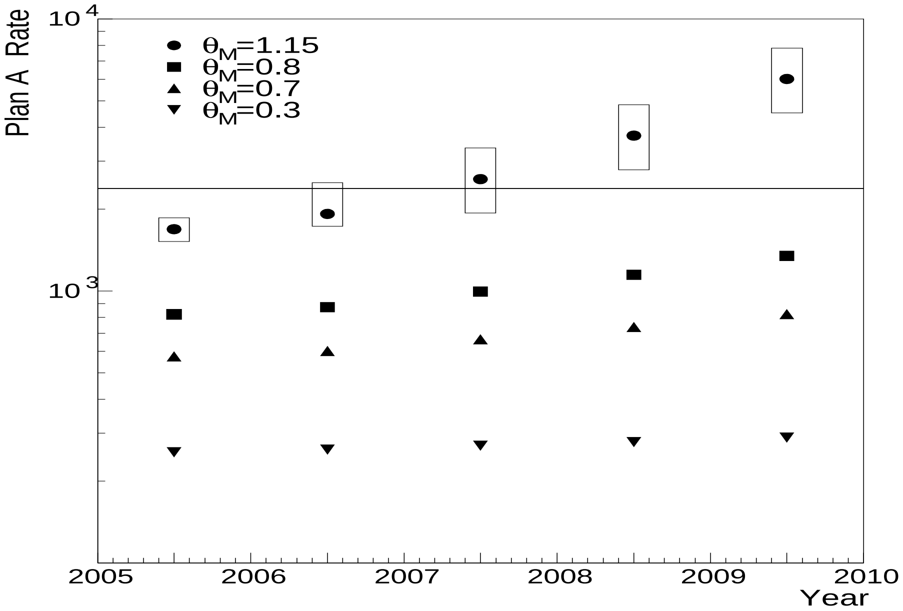

Figure 4.3: *Simulated trigger rates of the AMS02 experiment during the period 2005÷2010. The markers refer to different values of the geomagnetic coordinate* θ_M *as explained on the plot itself. From [145]*

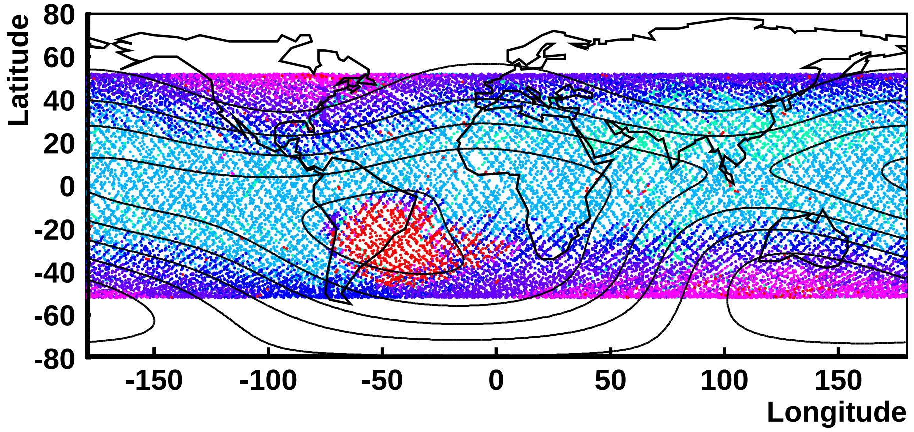

Figure 4.4: *AMS orbit envelope: the values of θ_M are colour coded on the plot.*

$1\ \mathrm{m}^2\mathrm{sr}$ is anyhow kept by our trigger condition. The actual trigger of AMS is at present under active development along the lines we followed for our offline implementation so we do not expect major differences in the performance: we will therefore assume that our trigger "setup" represents a conservative starting point for the analysis that will be detailed in the next chapter.

4.3 Event reconstruction

Each generated event that is accepted by the *unbiased* trigger, before being stored on disk, is fed to the event reconstruction algorithm and analysed just as a real one.

Each sub-detector is first treated as a stand-alone system and its raw data are searched to identify simple patterns (e.g. groups of nearby read-out channels above a threshold). When a pattern is found, it is stored internally in a C++ object containing all the relevant information carried by the pattern itself. Those objects are used in turn to identify higher level patterns, specific to the particular detector, that carry additional information and so on. In this way data are organised into hierarchical structures that allow to easily recover the low level information used to evaluate the characteristics of the top level objects. These object hierarchies are eventually stored on disk using the ROOT `TTree` data structure, which contain the full MC data along with the results of the reconstruction.

When the first phase of the reconstruction is completed, the top level structures from each sub-detector, namely – `TRDTrackR` from the TRD, `TrTrackR` from the TRACKER, `RichRingR` from the RICH and `EcalShowerR` from the ECAL– are further combined into the highest level structure of the reconstruction, the `ParticleR`. To build the `ParticleR`, the spatial information of each candidate data structure is extrapolated towards the other detectors and a geometrical matching is performed, and the other available informations are also checked against huge inconsistencies and are possibly refitted using the additional information now available from the other detectors. Finally a `BetaR` object, containing the velocity of the particle is built using the TOF information and the length of the `TrTrackR`, while from the analysis of the signal

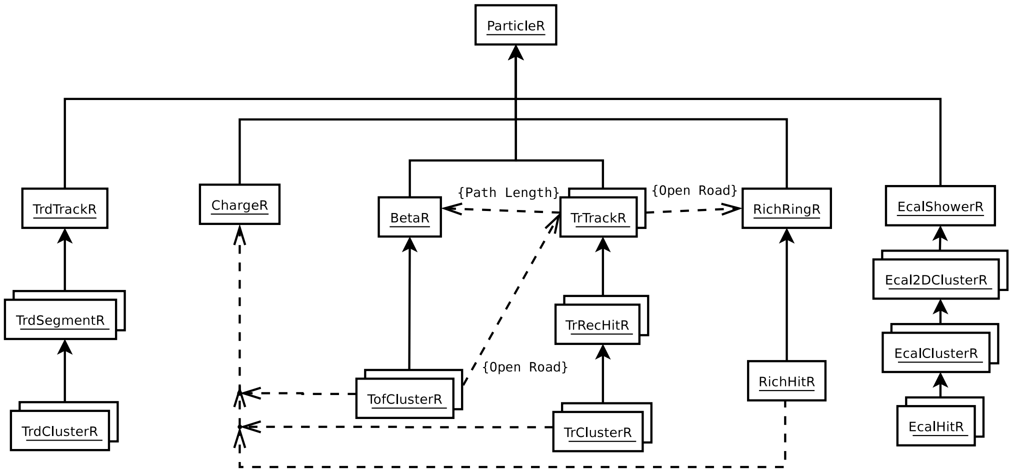

Figure 4.5: *Simplified scheme of the* C++ *objects hierarchies that describe the reconstructed event. These hierarchies are exactly mirrored in the* ROOT *output file.*

amplitudes measured in the RICH, TRACKER and TOF the particle charge modulus is recovered and stored in a `ChargeR` object. A partial picture of the relationships between the various objects is portrayed in figure 4.5.

Actually, the inner TRACKER is the sub-detector with the best spatial resolution, so it is mainly the extrapolation of its `TrTrackR` that drives the geometrical matching of trajectories. Since this sub-detector plays a crucial role in several aspects of event reconstruction, in particular for the particle charge sign determination, we are now going to explain in more detail the reconstruction algorithm for this particular subsystem.

4.3.1 Track fitting

The starting point of track reconstruction, is the identification in the ladder of *clusters*[2] of adjacent strips whose signal to noise ratio exceeds a threshold value . Since the two sides of a ladder are characterised by different values of the noise, the S/N thresholds will necessarily depend on the scanned side, but we will not delve here in the details of cluster finding algorithms.

The spatial information carried by clusters is bi-dimensional as p-side cluster measure the bending coordinate (y in AMS coordinate system) and n-side clusters the non bending one (x), while the third coordinate is given by the z position of the layer to which the ladder belongs. To have three-dimensional measurements, necessary for an accurate track fitting in a non homogeneous magnetic field, p-clusters and n-clusters are arranged in pairs, called either *hits* or *3-hits*[3].

In principle clusters from different sides of the same ladder may be matched according to their signal amplitude, however at the start of the MC production, this was not implemented and all possible combinations were considered [146]. Due to the

---

[2] The corresponding C++ class used for storage is `TrClusterR`.

[3] Stored as `TrRecHitR` objects.

ladders layout, the position of n-clusters has an intrinsic ambiguity along the x coordinate, so for each pair of clusters we must actually create from six to eight 3-hits with the same y position and equally spaced x (~ 8 cm).

To determine which 3-hits form a track efficiently, the track finding algorithm uses information from the TOF. The impact positions on the TOF planes are known with accuracy of $\mathcal{O}(\mathrm{cm})$ so, combining the upper and lower TOF planes impact coordinates, it is possible to evaluate a rough straight line estimate of the particle trajectory in the (x,z) plane and define a so called *road* around it. In this way only 3-hits that lie within the road need to be considered by the track finding algorithm. For each open road, all possible combinations of the contained 3-hits are then probed.

The (x,z) and (y,z) projections of the track candidates are separately fitted with respectively a straight line and a circle. These fits are very inaccurate, however they allow to reject with a minimal computational effort the candidates that are plainly not aligned just imposing very loose cuts on the χ^2 values from the just mentioned two fits. Finally the survived candidates are fitted using a 5×5 matrix inversion method taking into account the magnetic field distribution to resolve the last ambiguities. In this case the track is accepted if $\chi^2 < 100$.

If in some of the TRACKER planes no n-cluster is available, but a p-cluster is present, a fake n-cluster is created according to the TOF estimated trajectory; this is an attempt to use the information provided by the p-side that is known to be more accurate.

The algorithm just described, allows for the identification of more than one track per event and indeed, if fake clusters were introduced or the n-side ambiguity was not completely resolved, it is found that multi track events are more likely.

From the reconstructed tracks fits we can obtain the value of the particle rigidity $\mathrm{R} = \mathrm{P}/\mathrm{q}$ that determines the curvature of the track itself. There are actually three methods to evaluate R:

- the already mentioned 5×5 matrix inversion method, used for track identification because of its speed of execution, that can considered the standard algorithm and is often referred to as the *Fast Fit*;
- a method based on the use of the GEANE [147] package, that is integrated with GEANT and can access directly the geometry and material definition of the simulation;
- an alternative fitting method called *Path Integral* [148] method, based on the propagation of a particle with in the magnetic field from a TRACKER plane to the next one: the trajectory parameters are evaluated by a χ^2 fit of the observed positions to the ones evaluated in the propagation.

The last two methods, with different approaches, take into account the effect of the interaction of the particles with the material of the detector to improve the accuracy of the particle rigidity measurement.

In Figures 4.6 and 4.7 are shown the results of a test performed applying the three fitting algorithms on a sample of MC data in correspondence to three reference rigidities: 1 GeV, 10 GeV and 100 GeV. We notice that the GEANE algorithm performance tends to be worse than the other two at both high and low momenta. On the other hand the *Path Integral* algorithm achieves a better performance at higher momenta, while at low ones it does not seem to improve on the results of the *Fast Fit*.

The two algorithms are under active development to improve their performance: for instance in *Path integral* algorithm at the time was not implemented a realistic de-

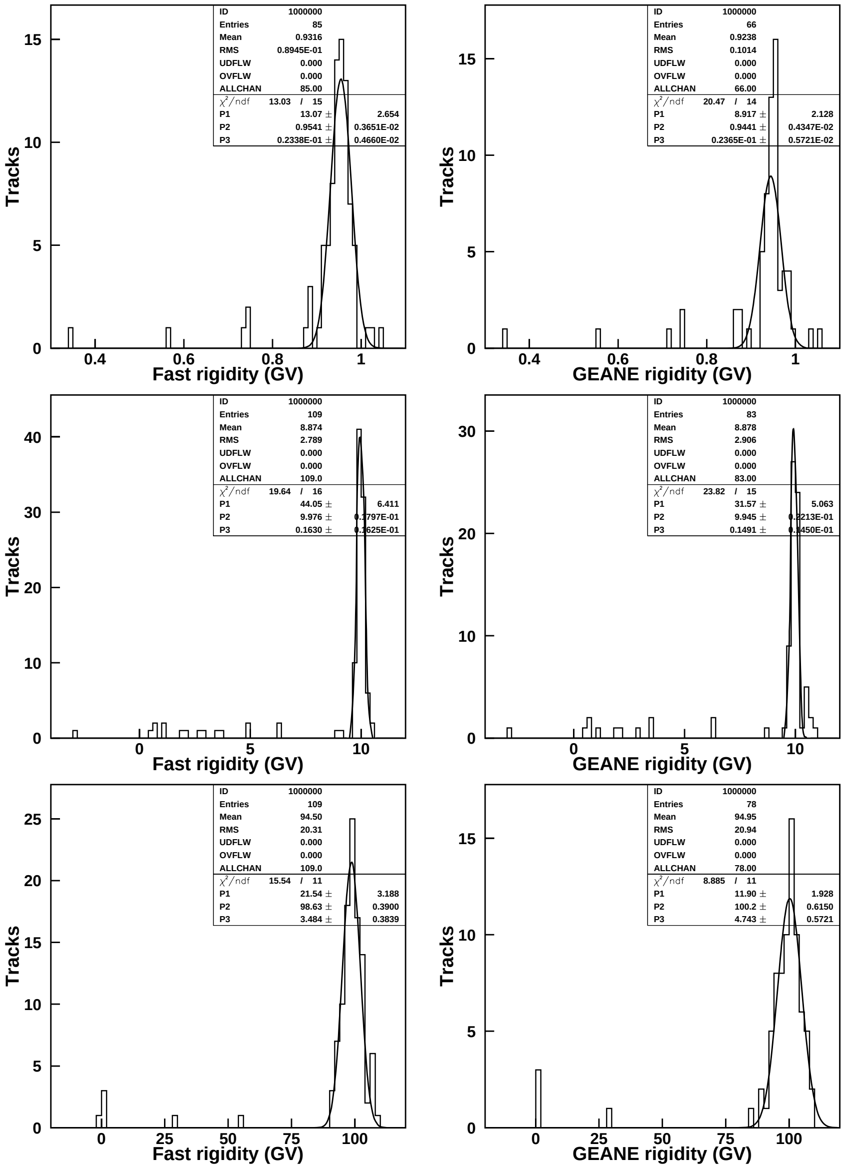

Figure 4.6: *Comparison between the rigidities measured by use of Fast Fit (on the left column) and* GEANE *Fit (right column). The generated rigidities are from top to bottom* 1 GeV,10 GeV *and* 100 GeV.

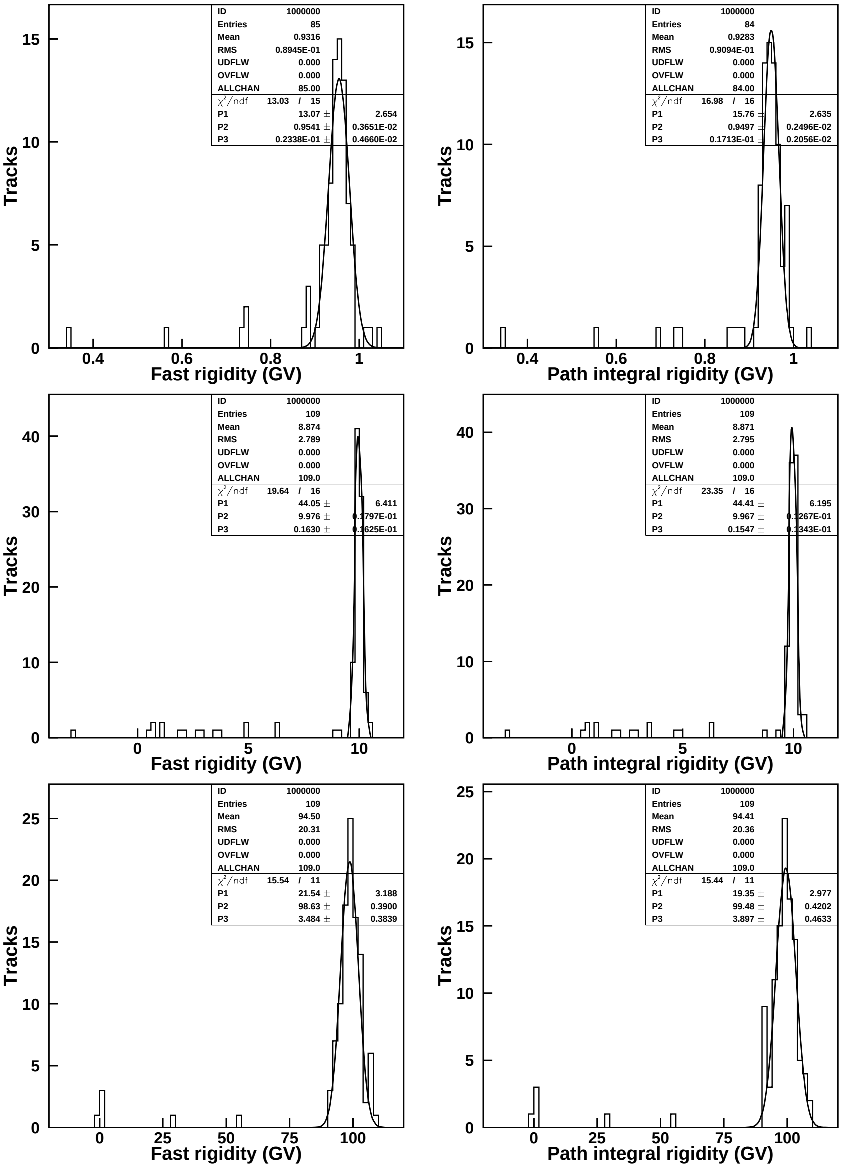

Figure 4.7: *Comparison between the rigidities measured by use of Fast Fit (on the left column) and Path Integral Fit (right column). The generated rigidities are from top to bottom* $1\ \mathrm{GeV}$,$10\ \mathrm{GeV}$ *and* $100\ \mathrm{GeV}$.

scription of the magnetic field inside AMS and it is known that the error on the propagation of particles in a magnetic field depends on the value of the field itself along the path and is in general more severe for low energy particles. The approximation on the $\overrightarrow{B}$ field introduced an additional source of uncertainty that may account for the observed behaviour of the method.

4.4 The AMS Monte Carlo production

In order to study the performances and capabilities of AMS, the Monte Carlo described in the previous sections has been used on a large scale production campaign, in which many groups participating to the collaboration were involved from February to August 2004 with about twenty production sites in Europe, China and USA. In Italy the production initially took place in the INFN sections of Milano, Siena, Bologna and Perugia, then it was transferred to the INFN National Centre for Telematics and Informatics (CNAF).

To suit a wide range of studies various samples were produced for all particle species that AMS can observe, both over the whole measurable momentum range and / or at specified energy. For the purpose of this work the relevant samples are those containing anti-protons, electrons and protons, the former being the signal and the latter two the sources of background. The available samples of the relevant species that were generated with the continuum spectrum described in section 4.1.1 amount to about 105×10^6 evt. for anti-protons, 2.2×10^9 evt. for protons and 300×10^6 evt. for electrons.

It can be noticed how the produced statistics for anti-proton events is much reduced with respect to the proton sample. This would lead to larger uncertainties in our assessment of detector acceptances for the anti-proton signal with respect to the background study. However, taking into account that, at the energies of our interest, the detector response is basically the same for p and $\bar{\mathrm{p}}$, we made use of the proton events to study the detector response also to $\bar{\mathrm{p}}$, the protons with wrong charge assignment being representative of the background and the correctly reconstructed ones being assumed as our signal.

A first selection was tuned to accept a maximum of correctly reconstructed protons while rejecting a maximum of wrongly reconstructed ones. The same selection was then applied to the e^- sample, and further criteria identified to minimise the acceptance for this background, The two selections were applied simultaneously to the proton and electron samples as it would happen for real data.

A detailed account of the analysed samples statistics can be found in table 4.1, which reports the number of events that were generated, those stored on disk and finally the number of the stored events that fulfilled a minimum set of requirements (pre-selection) which ensure that they can be analysed at all. The pre-selection criteria will be discussed in section 5.1.

4.5 The Analysis Software

Since the data are stored in ROOT trees, the analysis program that implements the selection has been developed within the object oriented ROOT framework, taking full advantage of its features. A typical analysis consists in a set of selection criteria (or

	Range	Gener.	Stored		Pre–sel.		Overall
	(GeV)	10^6 Evt.	10^6 Evt.	Ratio	10^6 Evt.	Ratio	Ratio
Protons	0.5–10	997.0	25.3	0.0253	7.4	0.293	7.434×10^{-3}
	10–200	929.0	42.7	0.0460	8.0	0.188	8.641×10^{-3}
	200–1789	370.0	20.0	0.0541	3.2	0.162	8.781×10^{-3}
Electrons	0.5–10	200.0	7.0	0.0351	1.7	0.237	8.308×10^{-3}
	10–200	76.0	3.9	0.0499	0.75	0.197	9.808×10^{-3}
	200–1789	9.4	0.54	0.0580	0.085	0.156	9.020×10^{-3}

Table 4.1: *Synthetic table of the statistics used in the analysis at different levels. The table reports generated events, events stored on disk and events that satisfy the preselection condition in units of* 10^6 *events, and the corresponding reduction ratios with respect to the previous level; the last column contains the overall reduction ratio between generation and preselection.*

cuts for short) that are applied in turn to the data; to have a synthetic representation of the information contained in the events that fulfil the selection criteria, they are then used to fill a set of histograms. Bearing in mind the task to perform, we designed the program in such a way that allows easy introduction of extensions and an fair degree of flexibility. This has been achieved with the definition of two C++ classes: the histogram manager class `DHF` and the cut manager class `DCut`.

The task of `DHF` is to allow the booking, filling and storage of histograms in an ordered way with a minimum of effort on the part of the user. Each `DHF` object contains a set of histograms internally stored in a `TObjectArray`, which is a ROOT pre-defined container class that allows to easily retrieve its elements, either by a numerical index or by the name string that is associated to each one. The choice and booking of the histograms is the user responsibility, as well as the definition of the sequence of commands necessary to fill them. The structure of the class ensures that at any point of the analysis program it is possible to fill all of the relevant histograms with one single instruction.

The `DHF` also contains a `TDirectory` object to which newly created histograms are also assigned by default: the user can optionally create a whole hierarchy of nested `TDirectory`-es to order the histograms neatly. The order to save in a ROOT-file the top level `TDirectory` causes the whole hierarchy to be saved recursively. If there are more instances of `DHF` objects, they can be saved in the same file, provided that the names of the respective `TDirectory`-es are all different. Different instances of this class may, of course, be filled according to different criteria.

The management of the criteria is the task of `DCut`, which implements a powerful and flexible interface to an external cut library. The interface is based on a text *data-card* that contains in each line the name of one of the cuts implemented in the library, followed by numerical flags and a list of up to ten parameters. An optional momentum range in which to apply the cut may be provided after the parameter list, otherwise the range defaults to $[-\infty, +\infty]$. The cut names are used to retrieve the corresponding implementation from the library, that has a structure similar to that of `DHF`, but it contains references to functions instead of histograms.

Each event is tested by `DCut` against all the configured cuts following the order in which they appear in the data-card. The outcomes of the checks are used to keep track of the number of events that survive the cut, either applied as *first-cut* or according to their position in the sequence (*positional* mode). Successive cuts are combined by the

AND logical operator. These values are then available to the user without the need to apply them again: it is also possible to know the result of the whole cut chain with the exclusion of one of the criteria (*exclude* mode).

Numerical flags in the datacards are used to specify whether or not a `DHF` object must be allocated in association to a particular configured cut and the filling mode (first-cut, positional or exclude). In this way the relevant informations can be gathered in correspondence to different cut levels in one run.

In a typical analysis session the user needs only to edit the data-card to set the parameters, filling mode and evaluation order of the existing selection criteria; whenever new quantities need to be considered, the user has only to define the relevant histograms and add the code that instruct the `DHF` class on how to fill it properly. As the two classes take over the burden of cut and histogram management, the user can concentrate on the definition of the selection criteria and the actual analysis. New criteria are added to `DCut` defining a function with a standard argument list that performs the necessary checks; this function is inserted as a new entry in the cut library at compile time and its parameters are thereafter configurable through the data-card without the need of further recompilation.

In the next chapter we will describe in detail the selection criteria we applied to the data and the achieved reduction of the backgrounds.

Chapter 5

The anti-proton selection

We have discussed in chapter 2 the possible DM signatures in the anti-proton CR flux. From the experimental point of view, the first challenge is to efficiently detect the faint anti-proton signal, whether of primary or secondary origin, in the overwhelming background of ordinary CR fluxes.

We already discussed in 3.8.1 how the charge identification in AMS is reliable, meaning that $Z > 1$ species do not constitute a noticeable source of noise in the measurement of the anti-proton spectrum. Among the $Z = 1$ particles positrons are a minor component of the CR flux and the fraction of mis-reconstructed ones, that would constitute a background to our signal, is still lower, so we need only consider the contributions of electrons and protons.

The background in the anti-proton channel originates essentially from errors in the measurement of the charge sign (e.g.. $\mathrm{p} \longrightarrow \bar{\mathrm{p}}$) or of the mass of the particles (e.g. $\mathrm{e}^- \longrightarrow \bar{\mathrm{p}}$). The first source of background (charge confusion) is related to the fact that the charge sign is measured from the bending of the particle trajectory in the TRACKER. At low momentum, multiple scattering may alter the helicoid trajectory of the particles so much as to fake a bend in the opposite direction. On the other hand, as momentum increases the magnetic field bends the trajectory less and less, so that statistical fluctuations in the TRACKER hits positions can steer the fitting algorithm towards the wrong charge sign. Conversely, if we consider a less severe error in the determination of momentum, it is still possible for a negative particle to have its mass measured with a value very close to that of an anti-proton, which accounts for the second background we mentioned.

Given that the $\bar{\mathrm{p}}/\mathrm{p}$ ratio is about $10^{-5} \div 10^{-4}$ at momenta in the range observed with AMS, in order to discriminate signals as faint as the ones described in chapter 2 it is essential that less than one p out of $10^{6\div7}$ is assigned the wrong charge sign. Analogously the e/p ratio is of order $10^{-3} \div 10^{-2}$, which means we need to achieve an electron rejection power of at least $10^{-4} \div 10^{-5}$

There is also an instrumental background to consider that arises when the impinging proton interacts with the detector's material; the products of such interactions are subsequently measured in the downstream sub-detectors leading to inaccurate event reconstruction. These secondaries may also be true negative particles and as such mistaken for anti-protons.

In this chapter we will present in detail the selection of anti-proton events in AMS, taking advantage of the complementary measurements of the different sub-detectors.

We will first discuss the tracking performances and the selection criteria developed to reject poorly reconstructed tracks. We will then illustrate the use of combined velocity and rigidity measurements to further identify mis-reconstructed protons. Electron rejection based on TRD, ECAL and velocity measurements will be then discussed. We will finally present the acceptances for signal and background

5.1 Pre-selection of the events

As discussed previously (see chapter 4), the AMS event reconstruction as well as the trigger logic apply quite loose criteria in the definition of a *particle* to avoid possible biases for different event topologies. As a consequence, the MC samples contain a large fraction of particles with no track associated in the TRACKER or marginally measured in the TRD, which are of no use for our study.

We therefore applied a preliminary selection imposing on the reconstructed particles the minimal set of requirements which ensures that they are suitable for subsequent analysis; namely we ask that

- the particle must come with an associated track object, which implies a rigidity measurement,
- a velocity measurement must be available to resolve the ambiguity due to the direction of the particle's motion and we ask it to be positive,
- the charge modulus has been determined, so that we can recover the particle's momentum combining it to the rigidity. We also ask that $Z = 1$, though in the whole sample only 1 particle was assigned a $Z \neq 1$

When these conditions are met the particle has been reasonably reconstructed and we conventionally qualify it in the following as a "normal" particle. An event is acceptable for analysis only if it contains normal particles: the distribution of the number of normal particles per event is presented in figure 5.1 for the whole MC sample and normalised to 1. Events containing normal particles are about $1/4$ of the total, and among them only a few permille contain more than one normal particle (etched areas in figure 5.1). We decided to accept only events containing exactly one normal particle to have cleaner events at a negligible price in term of efficiency.

At this stage we also bore in mind the issue of particle identification; although we can exploit the combined TRACKER / TOF information to partially reduce the electron contamination at low momenta to some degree, we still need some other means to perform the particle identification in the higher energy parts of the spectrum. To achieve this goal, we also require our normal particle to have an associated TRD track. This additional request introduces in our analysis a reduction of the acceptance of about 20% over the full energy range. In figure 5.2 are shown the efficiencies of the *OneNormal* and *OneNormalTRD* requests with respect to the trigger level as a function of the particle rigidity (blue squares and green circles respectively).

5.2 Track selection

While the charge modulus of a particle is redundantly determined in AMS from the reconstruction of the energy deposit in several sub-detector, the charge sign assignment relies uniquely on the measurement of the bending direction of the track in the

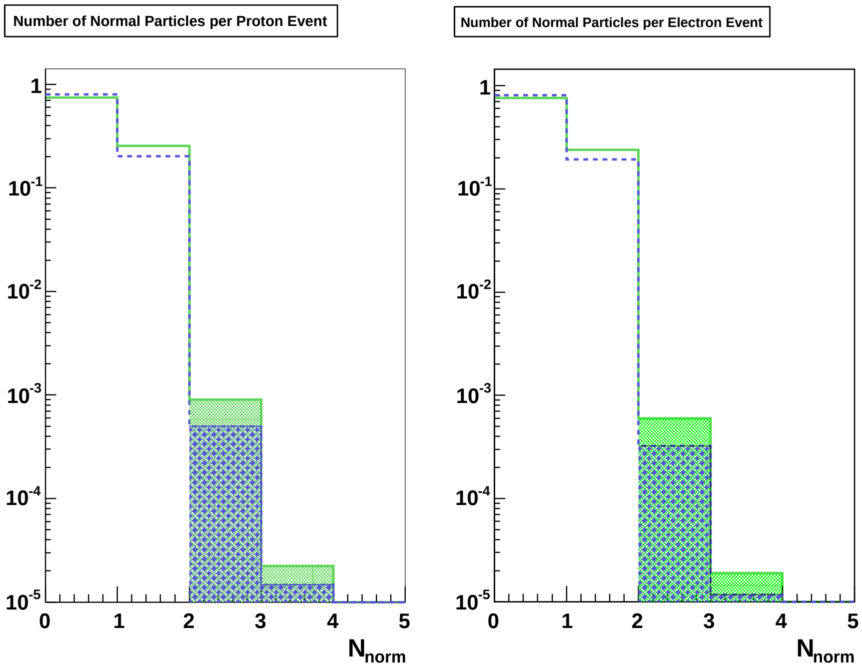

Figure 5.1: Normalised distributions of the number of normal particles per event is displayed by the green solid line; if we add the request of TRD *signal, we obtain the distribution shown by the blue dashed line. The events with more than one normal particle (etched areas) represent only about* 0.3% *of those with exactly one.*

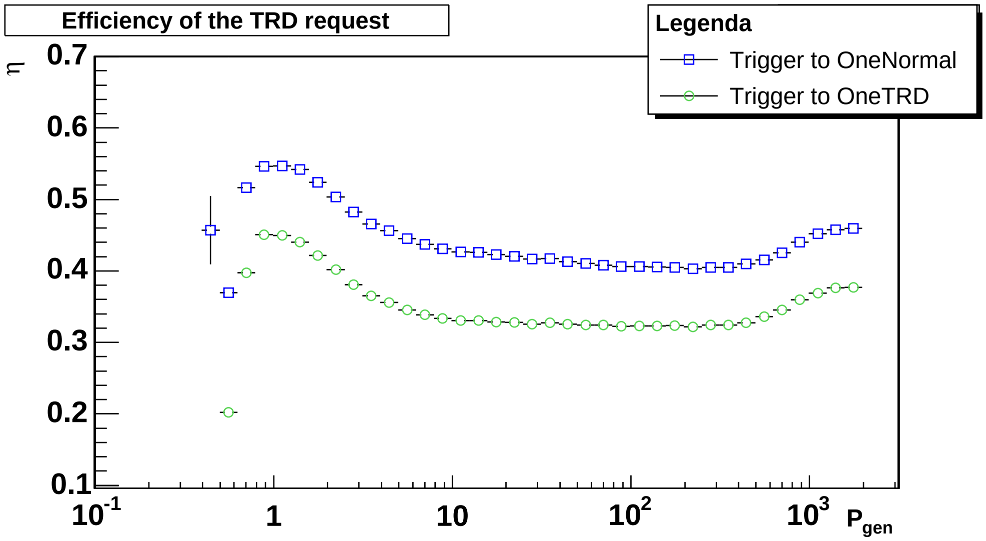

Figure 5.2: Efficiency of the OneNormal (blue squares) and OneNormalTRD (green circles) selection condition as a function of generated momentum, with respect to the trigger level. The black crosses report instead the efficiency of the OneNormalTRD condition with respect to OneNormal.

magnetic field. A positive (negative) rigidity is assigned to particles whose tracks have experienced a clockwise (anticlockwise) bending around the magnetic field direction, using the time of flight measurement to solve the two-fold ambiguity on the particle's arrival direction.

In figure 5.3, it is shown the velocity distribution from the TOF for protons impinging in AMS from the top. No particle is measured with the wrong sign of β, so the level of mis-reconstruction in the incident direction is less than $\sim 10^{-6}$ for both electrons and protons.

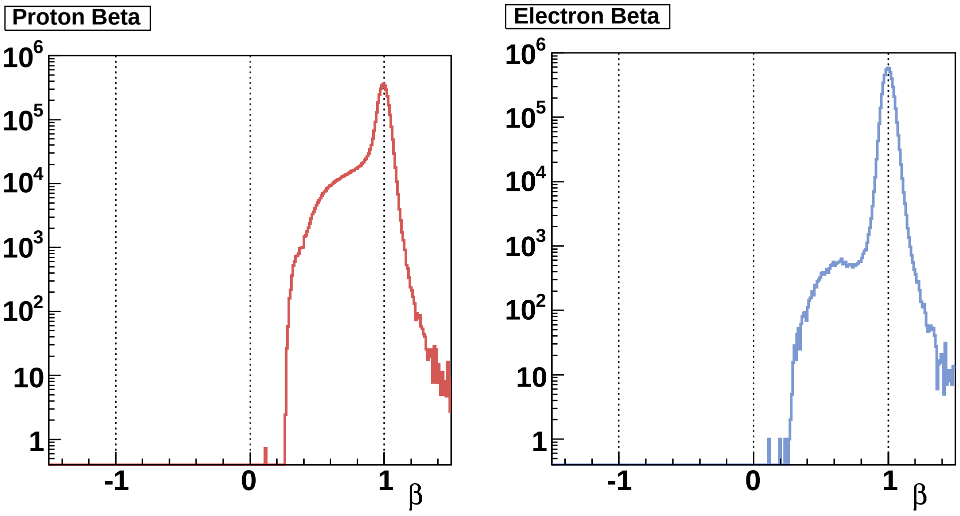

Figure 5.3: *Distribution of reconstructed β for protons (left plot) and electrons (right plot) impinging in* AMS *from the top; no particles have been reconstructed as coming from the wrong direction over a sample of four million for both particle species.*

The only handle to control the amount of charge confusion and keep it at the level needed for anti-proton selection relies on strict requirements on the quality of the track reconstruction.

5.2.1 Proton momentum resolution

The basic goal of our study is to define a set of criteria, based on the features of the reconstructed event, which allows the rejection of poorly measured tracks. To identify the quantities most sensitive to mis-reconstruction, the first step has been to split our MC sample – where the kinematical parameters are exactly known – into streams of events with different accuracy of the reconstruction. The distribution of several experimental quantities in the different streams have been compared to identify the most useful for our selection.

The relative momentum resolution, i.e. the relative deviation of the reconstructed from the generated momentum of the particle:

$$\delta \mathrm{P} = \frac{\mathrm{P}_{gen} - \mathrm{P}_{rec}}{\mathrm{P}_{gen}} \tag{5.1}$$

has been chosen as the basic criterion to classify the reconstruction quality. Since the momentum resolution is expected to depend on the momentum itself, the classification will be momentum dependent as well.

In figure 5.4 is displayed the scatter plot of δP vs the generated momentum P_{gen}. Our definition is such that a particle has $\delta\mathrm{P} > 1$ whenever its charge sign is wrongly determined (plotted as red squares); in such cases we label the particle (proton) as "*Neg*". To further identify protons whose momentum has been poorly reconstructed, although with a correct charge sign, we studied the average behaviour of δP as a function of P_{gen} for the proton data. The result of this study—performed excluding *a priori* the *Neg* protons—is also shown in figure 5.4, superimposed to the scatter plot.

We notice that for momenta above few hundred GeV the resolution is deteriorated because the particle path starts to be too rigid and the spatial resolution of the track measurement limits the capacity to determine its curvature; as a consequence both the average and the spread of δP increase, meaning that the reconstructed value tends to be lower than the generated one. At low momenta ($\mathrm{P}_{gen} \simeq 2$ GeV) the spread does not grow so much, but due to the higher energy loss by ionisation that low velocity protons undergo through the detectors material, the measured curvature does not correspond to the generated momentum, but rather to one that is on the average up to 20÷40% less than P_{gen}.

Particles that were reconstructed with a value of δP that differ from the expected value less than the corresponding spread are therefore labelled as "*Good*" particles whereas the ones that neither *Good* or *Neg* are tagged "*Bad*"; the green and blue data points in the scatter plot of figure 5.4 refer to these last two categories respectively.

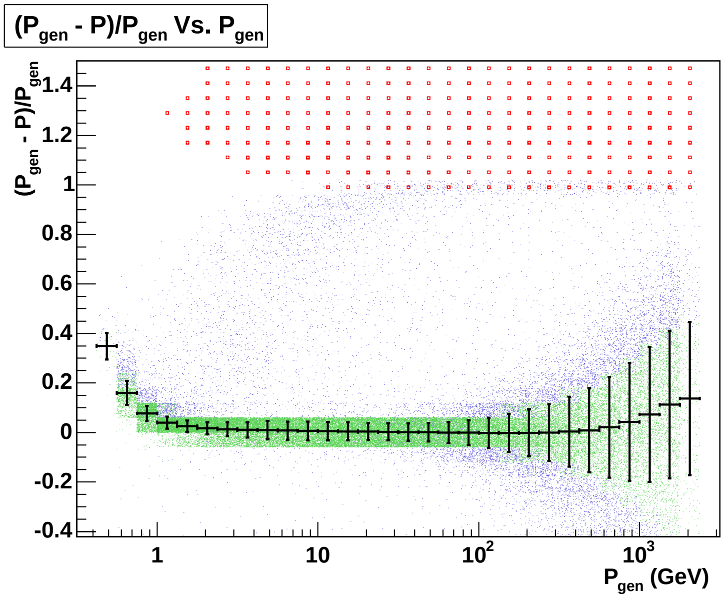

Figure 5.4: *In the present figure are shown the three categories of particles, identified using the profile histogram which is reported in this plot too (black markers with error bars). Green refers to Good particles, whose* $(\mathrm{P}_{gen}-\mathrm{P}_{rec})/\mathrm{P}_{gen}$ *is within the errors of the profile, while blue refers to Bad particles; the particles with wrong charge sign (Neg) are represented as red boxes to give them more evidence.*

5.2.2 Number of hits per track

As a starting point we consider some simple conditions that are reasonably connected with the quality of the tracks, such as the distribution of the number of hits used to build the track associated to the particle. As a general remark, the accuracy to the fitted track parameters improves with the number of hits reconstructed in the TRACKER along the particles trajectory. This is not only a trivial consequence of the increased number of points used to determine the trajectory, but is also related to the larger span of the track sampling and the possibility to disentangle abrupt changes in the track curvature due to scattering in the detector material. A track with associated hits on all eight planes of the TRACKER, is effectively reconstructed in the $106\ \mathrm{cm}$ of the full TRACKER depth, while if one or both of the outer planes hits is not used, the lever arm of the measurement is reduced of $\sim 20\%$ or $\sim 40\%$ respectively. Conversely, if one or two hits are missing from inner planes it is more difficult to disentangle scattering effects.

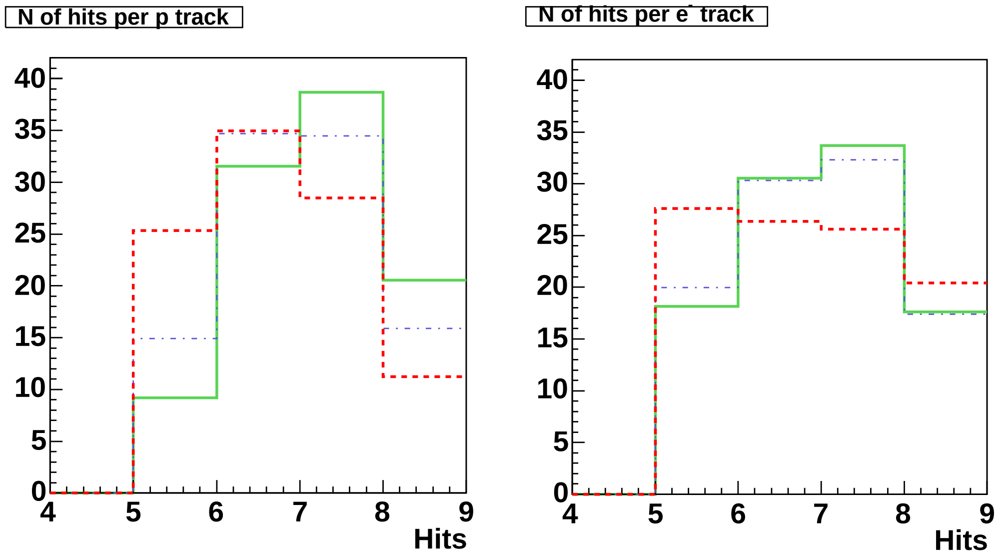

Figure 5.5: Distributions of the number of hits per track. Left panel refers to protons, right panel to electrons. the distributions are normalised to 100. The different line styles represent the particle categories: green solid for Good, blue dash-dotted for Bad and red dashed for Neg.

Figure 5.5 shows the distribution of the number of hits used to reconstruct a track for both protons (on the left) and electrons (on the right). The distributions are normalised to 100 and have been plotted separately for the three categories of particles defined in section 5.2.1. In particular, the green solid line refers to *Good* particles, the blue dash-dotted one to *Bad* particles and the dashed red line to *Neg* particles. We will retain these conventions throughout the chapter whenever we will compare distributions related to particles belonging to the different categories.

As expected the wrong signed particles' distribution is slightly shifted towards low hit numbers. Cutting out tracks below six hits corresponds to the rejection of 9.2%, 15% and 25% of *Good*, *Bad* and *Neg* protons respectively. This cut is not only effective in reducing the proton contamination, but it generally improves the quality of the tracks,

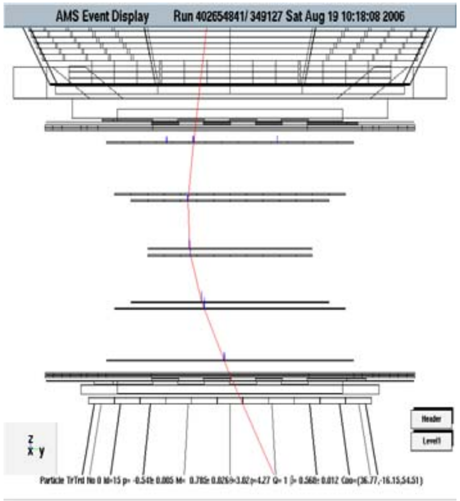

Particle TrTrd No 0 Id=15 p= -0.54± 0.005 M= 0.785± 0.026 θ=3.02 φ=4.27 Q= 1 β= 0.568± 0.012 Coo=(36.77,-16.15,54.51)

Figure 5.6: *Example of event with change of trajectory for a mis-assigned charge particle. The kinks happen at the third and/or fifth layer.*

eliminating the configurations with shorter span. Moreover, having more hits allows for a better performance of the following cut, that is intended to detect kinks in the track trajectory due to Coulomb scattering, so we impose the condition $N_{Hits} > 5$.

5.2.3 Two Halves comparison

As mentioned above, a source of mis-reconstruction of the charge sign is the Coulomb scattering. Although the AMS TRACKER is very transparent to particles, it is possible for a single interaction in the honeycomb planes that support the ladders to alter the trajectory so much as to fake a bend in the wrong direction.

We can end in this situation even without a real scattering event. The algorithm that builds the track can be confused by spurious hits and fluctuations in the measurement of the hits' positions, or it may not be able to fully resolve the n-side ambiguity due to the bonding scheme of the Si ladders. This is particularly true as the momentum increases and the trajectories become more rigid.

As an example we present in figure 5.6 the event display for a reconstructed particle that has this behaviour.

To detect such situations we perform a consistency check on the reconstructed rigidity, by splitting the track in two sub-tracks, each one containing half of the hits that form the complete one. Using the two half-tracks we can measure independently the radius of the trajectory in the upper and lower section of the TRACKER. Whether the track's kink is due to a real scattering, a fluctuation or a mis-assigned hit, only one section will be affected by it and the two results will be different. Of course the rigidity resolution of half-tracks will be worse than that of a complete one, since the span is necessarily lower, and at times it may be necessary to share the middle track hit between the two halves, just to have enough points to fit the trajectory parameters.

In a clean event, the two rigidity determinations should be compatible once the finite resolution effects are taken into account. Large discrepancies between the two halves fitted momenta are therefore an hint for an abrupt change in the particles' trajectory. As a track quality indicator we have used the ratio $\mathcal{R}_{LU} = \mathrm{R}_{Low}/\mathrm{R}_{Up}$, where $\mathrm{R}_{Low}, \mathrm{R}_{Up}$ correspond to the rigidity determined using the lower and upper half track respectively.

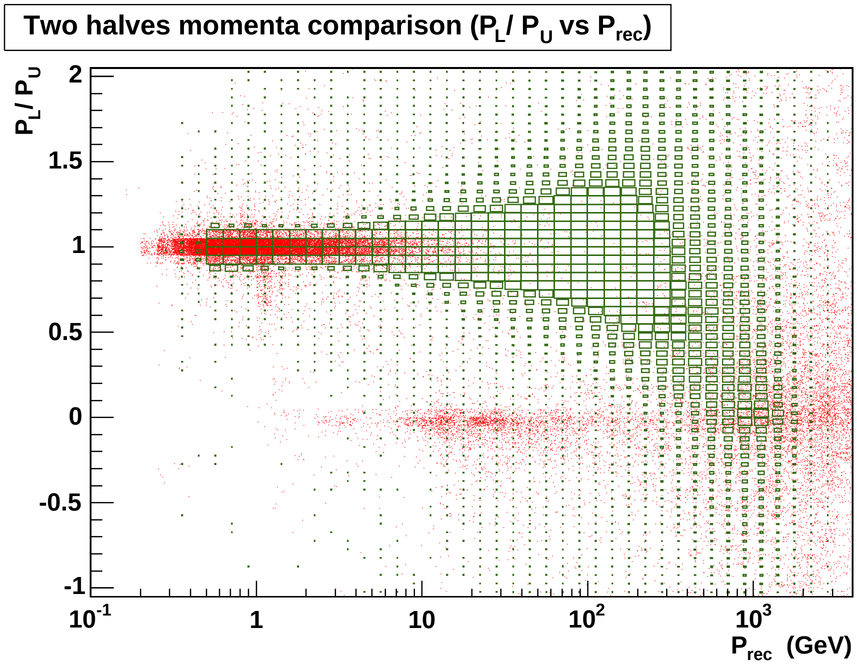

Figure 5.7: *Distribution of* $\mathcal{R}_{LU}$ *for Good and Neg particles versus* P_{rec} *(green boxes and red markers respectively). The number of particles with large deviations from the expected value of one steadily increases starting from* $\mathrm{P}_{rec} = 1$ GeV, *until over* 300 GeV, *where a substantial fraction of well reconstructed particles too is affected. Particles with wrong sign mainly cluster around zero.*

In figure 5.7 the $\mathcal{R}_{LU}$ distribution as a function of reconstructed momentum is shown for all tracks. A relevant deviation from unity an a larger spread of $\mathcal{R}_{LU}$ can be clearly seen, even for good tracks, at the higher momenta. Conversely, at low energy, even *Neg* tracks result having a good $\mathcal{R}_{LU}$.

To perform a track selection based on $\mathcal{R}_{LU}$, the momentum dependence of this quantity has to be taken into account. We identified a set of momentum intervals such that the $\mathcal{R}_{LU}$ had an homogeneous behaviour within each, the selection cuts were then separately tuned in different intervals.

In figure 5.8 are presented the distributions of $\mathcal{R}_{LU}$ for *Good* and *Neg* protons in the different intervals of reconstructed momentum.

Above 10 GeV the greater part of *Neg* protons clusters around $\mathcal{R}_{LU} = 0$, well distinguished from the bulk of the consistent p tracks up to the limit of about $250 \div 300$ GeV, after which *Good* protons show large inconsistencies too. *Bad* protons too feature the bump at $\mathcal{R}_{LU} = 0$, but the bulk of the sample clusters at $\mathcal{R}_{LU} = 1$, though the distribution is less peaked than in the case of *Good* protons.

In figure 5.9 the cumulative version of the previous distributions are reported, as well as the one for *Bad* protons. These plots actually display the fraction of events

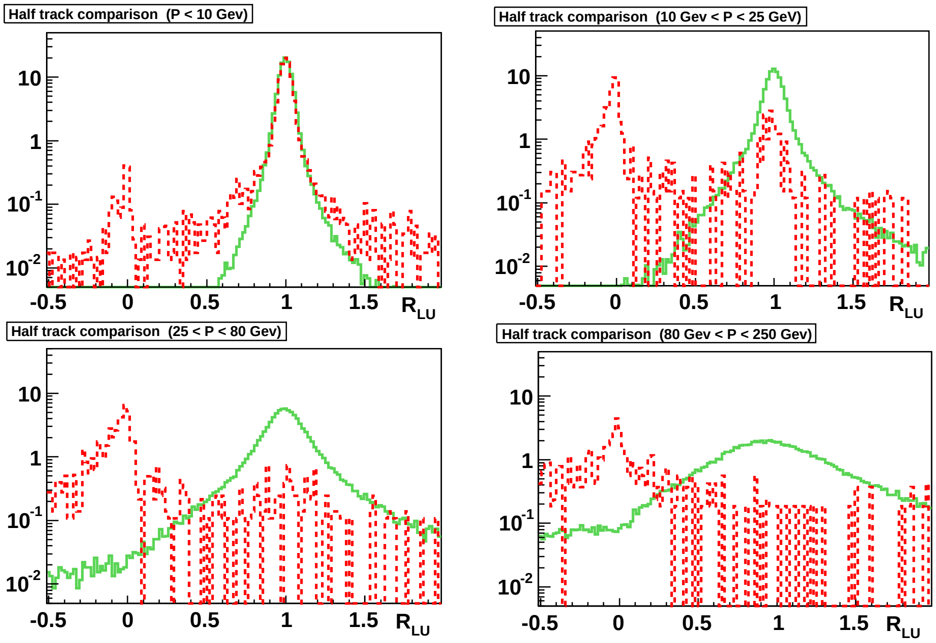

Figure 5.8: *Distributions of $\mathcal{R}_{LU} = \mathrm{R}_{Low}/\mathrm{R}_{Up}$ for Good and Neg particles in different intervals of reconstructed momentum; for the sake of figure legibility Bad particles are not shown here.*

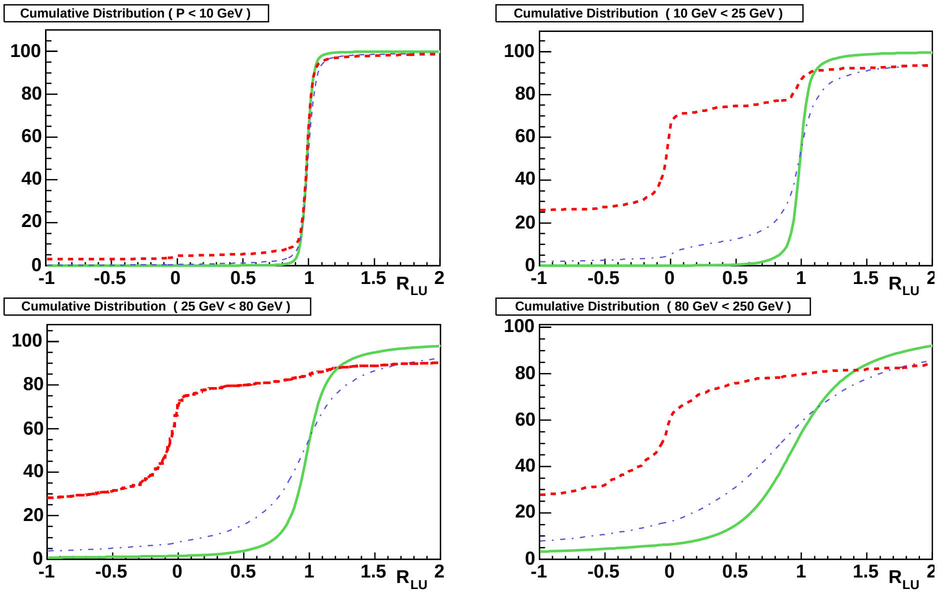

Figure 5.9: *Cumulative version of the distributions in figure 5.8; here we report Bad particles too.*

Range	Cut	*Good*	*Bad*	*Neg*
$1\ \mathrm{GeV} < P < 10\ \mathrm{GeV}$	$0.8 < \mathcal{R}_{LU} < 1.17$	1.1	6.7	15
$10\ \mathrm{GeV} < P < 25\ \mathrm{GeV}$	$0.69 < \mathcal{R}_{LU} < 1.39$	3.7	26	79.4
$25\ \mathrm{GeV} < P < 80\ \mathrm{GeV}$	$0.27 < \mathcal{R}_{LU} < 1.8$	5.4	21.4	88.1
$80\ \mathrm{GeV} < P < 250\ \mathrm{GeV}$	$0.20 < \mathcal{R}_{LU} < 2.0$	15.6	34.3	85.5
$250\ \mathrm{GeV} < P < 1000\ \mathrm{GeV}$	$0.00 < \mathcal{R}_{LU} < 2.0$	46.3	54.7	66.9

Table 5.1: *Values of the cut limits in different* P_{rec} *ranges: the last three columns report the percentage of discarded protons. The first cut was applied also below* $1\ \mathrm{GeV}$, *with negligible effects.*

below a given value of $\mathcal{R}_{LU}$ as a function of $\mathcal{R}_{LU}$ itself and give the effectiveness of imposing it as a lower bound. Similar curves have been studied to obtain the effectiveness for an upper bound cut.

As mentioned before, below $1\ \mathrm{GeV}$ even a very tight cut around 1 has little effect, but as soon as we move towards higher momenta the effectiveness of this quantity increases. In all the higher momentum ranges, setting the cut to about 0.3 already rejects 80% of *Neg* particles, however a fine tuning of the cut bounds allows a further cleaning of the sample from *Bad* protons.

We detail in table 5.1 the actual values of the cut parameters that select the allowed region, together with the percentage of discarded protons belonging to the three categories. Beyond $250\ \mathrm{GeV}$ the efficiency of this condition in term of *Good* particles deteriorates and only a loose condition has been imposed: we asked $0. < \mathcal{R}_{LU} < 2.$ for P above $250\ \mathrm{GeV}$ anyway.

5.2.4 Number of tracks

The track reconstruction algorithm described in section 4.3.1 is designed to allow for the identification of multiple tracks in the same event, as it is possible to have more than one particle crossing the detector, either because of an accidental coincidence of CR events or as the result of an interaction in the detector's structure (e.g. $\gamma \rightarrow \mathrm{e}^{-}\mathrm{e}^{+}$). Due to the presence of spurious hits or to the n-side readout ambiguity, also single particle events can contain more than one reconstructed track, as shown in figure 5.10, where the distribution of number of tracks per event is displayed separately for the three categories of particles. The distributions are all normalised to 100 and we report them for both the proton and electron samples.

The large majority of events has only one or two tracks, irrespective of the particle species and only differing between *Good*, *Bad* and *Neg* for the relative amount of one or two track events. It is quite interesting that about 61% of the *Neg* particles are grouped at one track per event and 37% has two tracks, while for *Good* particles the proportions are almost reversed (21% and 78% respectively); similar considerations apply to the electrons, whose distributions are also reported separately to evidence that it is a feature of the algorithm.

This behaviour hints that track reconstruction is more performing in the two track regime, even though only one particle is eventually reconstructed properly as imposed by the preselection. Since in the region with more than two tracks, are found less than 1 $^{0}\!/_{00}$ of *Good* protons and $\approx 1\%$ in the case of electrons, we considered only the configuration with a maximum of two reconstructed tracks.

A closer look at the structure of the two track events revealed that, in each TRACKER

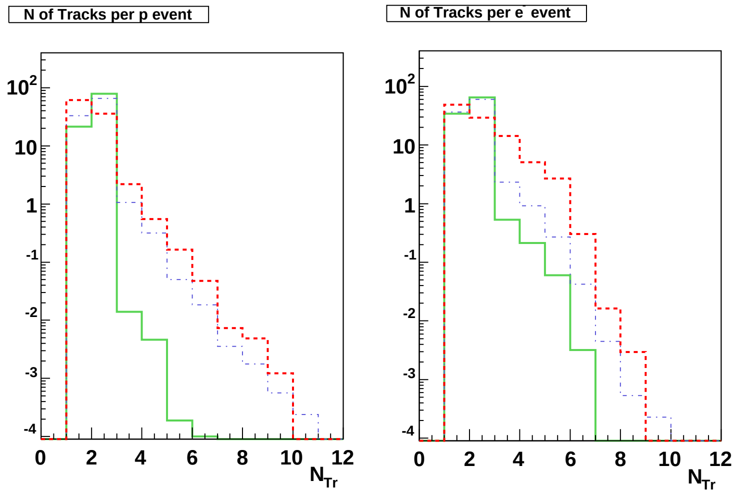

Figure 5.10: *Number of tracks per event distribution normalised to 100. The left panel shows proton data, the right one electron data. The usual convention on lines styles and colour is followed..*

plane, the hit used to build the track associated to the reconstructed particle, was not independent from its homologous belonging to the second track.

5.2.5 Two Track Comparison

As stated before, the TRACKER hits measured along the non bending direction, are not univocal and this forces the pattern recognition algorithm to consider all the allowed combinations of clusters from the two sides of the wafers. As a consequence, each crossed ladder, contains sets of hits that share the same p-side component cluster. The actual value of the bending coordinate for such hits is not bound to be exactly the same, due to the tolerance in the relative alignment of the individual Si wafers.

The ambiguity is resolved by cross-checks with the other sub-detector signals but at the pattern recognition level the only detector that enters into the business is the TOF system. The spatial resolution of the Time of Flight is often not enough to rule out all combinations, so we end up with more tracks than expected. On top of that, if the pattern recognition cannot find a fully satisfactory n-side companion for an p-side cluster, it is allowed to infer the x coordinate by interpolation of the TOF signals. This actually means to assign a fake n-cluster with reasonable coordinates and energy deposition to match the p-cluster. In a sense, the hits sharing the same p-cluster can be considered as overlapping. We checked the amount of overlap of the two tracks taking the fraction of hits in the first track that share their p-cluster with the corresponding constituents of the second. We used the fraction and not the absolute number to account for different track lengths.

The resulting distribution is presented in figure 5.11. It shows that in 87% of the cases, the overlap is complete: the two tracks are really built from the same data at least along the bending direction; we can somehow think of them as “parallel”.

If so, the rigidity determined using the second track (R_2) should be very close to the value associated to the particle and any significant difference would point to a

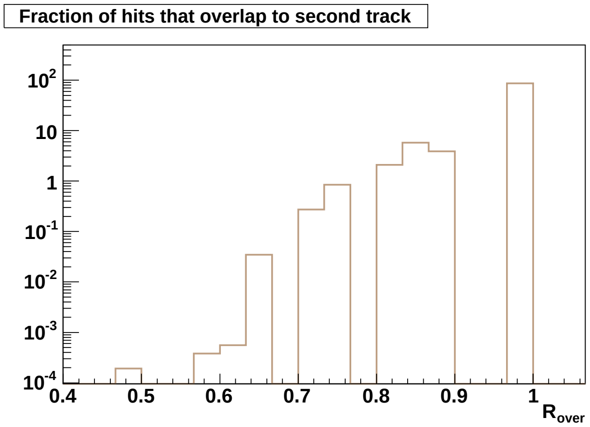

Figure 5.11: *Fraction of hits in the first track that overlap to hits in the second i.e. the two hits share the same p-cluster; the plot is for uncategorised protons. In $\approx$ 90% of the cases the 2 tracks are fully overlapping, hence "parallel" to each other.*

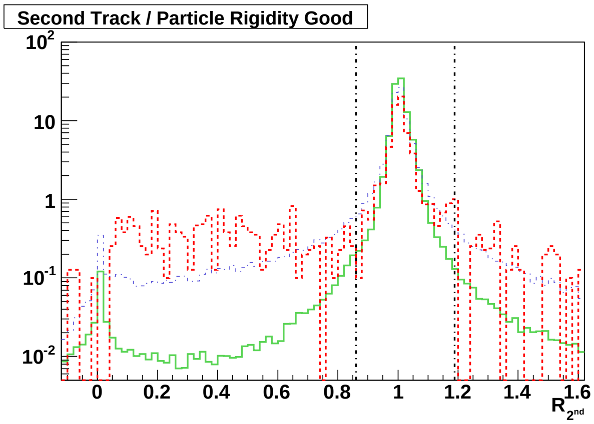

Figure 5.12: *Distributions normalised to 100 of the ratio between the rigidity of the second track and that of the one associated to the reconstructed particle ($\mathcal{R}_{2nd}$). The cut limits are displayed as vertical dashed lines.*

problem in the reconstruction.

The distribution of the ratio $\mathcal{R}_{2^{nd}} = \mathrm{R}_2/\mathrm{R}$, plotted in figure 5.12 puts in evidence how the *Good* protons are tightly clustered around 1, with a secondary peak at 0 coming from tracks with lesser overlap. Conversely the *Neg* and *Bad* particles feature large deviations that allow for an efficient cut that reduces charge confusion and improves the overall momentum resolution. The two vertical lines in figure 5.12 correspond to the values chosen to define the cut: $.86 < \mathcal{R}_{2^{nd}} < 1.19$. The effect of this condition is to cut out 2.6% of *Good*, 13.5% *Bad* and 61.7% *Neg* protons among the events with two reconstructed tracks.

5.2.6 Interacting particles: TRACKER activity

The possibility of particle production in the detector's structure has already been mentioned; now we are going to describe the cuts implemented in our study to remove this kind of events.

As an example, the event display of a proton interacting in the TRACKER material is shown in figure 5.13.

A possible signature for such kind of events, where the interaction happens in proximity of a TRACKER plane, is related to the number of hits found in the neighbourhood of the track. For the sake of conciseness, in the following we will refer to such hits as *near-hits* [1].

For *Good* and *Bad* tracks, only a small percentage of the hits used in the track has at least one *near-hit* associated in the same ladder. (1.7% and 4.4% respectively). In the *Neg* track sample, a larger fraction (15%) of the fitted hits has one or more *near-hit* companions.

To achieve a cleaner separation we constructed from the *near-hits* a variable associated to the track as a whole. For each track, we counted the number of TRACKER layers with associated *near-hits*: the resulting distribution is shown in figure 5.14 separately for *Good*, *Bad* and *Neg* tracks.

Just asking that the track has no associated *near-hits* at all, discards 10% of *Good* protons but at the same time rejects 18% and 45% of *Bad* and *Neg* respectively.

This does not exhaust the topic of secondary production; the interaction product are grouped together only in the first layer after production, and detector inefficiencies can conceal the bunch we are looking for. In addition, the interaction may well occur far from the Si layer, for instance in a structure outside the TRACKER itself.

As a further indicator of secondary production, we considered the total number of independent hits present in the TRACKER. The distribution shown in figure 5.15 reports the number of non-overlapping hits per event in the one-track regime; in fact this test was mainly designed for this case, since the discussion of section 5.2.5 is not applicable here.

From the plots we see that cutting out all events with more than 8 independent hits would be very effective, rejecting about 10%, 28% and 67% respectively of *Good*, *Bad* and *Neg* protons, but we chose relax the requirement and set the limit to 9 to allow for a possibly higher level of noise in the real detector. It is also worth to note that some of the cuts we will present in the following, are effective in reducing this kind of contamination too, partially compensating for the weakening of the present cut. The

---

[1] To actually exploit this signature, a special care had to be applied to avoid multiple hit counting in the *near-hits* estimate due to the presence of the overlapping hits discussed in the previous section.

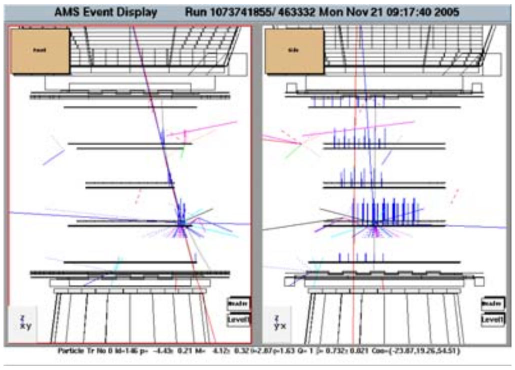

Figure 5.13: *Example of event with production of secondary particles in the structure of the detector (between* 6^{th} *and* 7^{th} *Si layer).*

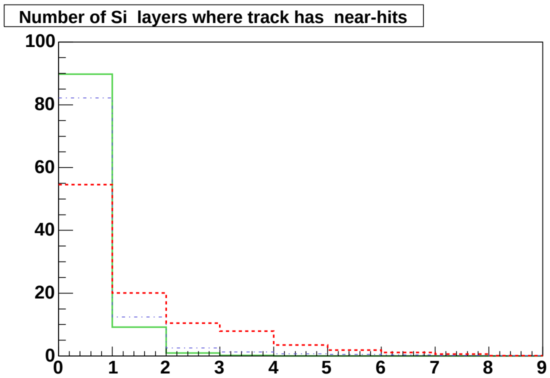

Figure 5.14: *Distribution of the number of Si* TRACKER *planes where the track associated to the reconstructed particle has near-hits (defined in the text). the distribution is normalised to 100.*

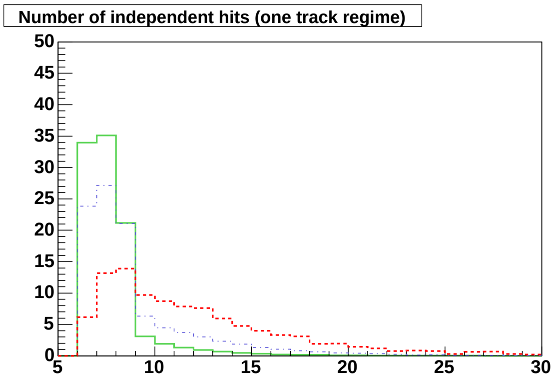

Figure 5.15: *Total number of independent (non-overlapping) hits in the event. The distributions, normalised to 100, are restricted to the one track regime.*

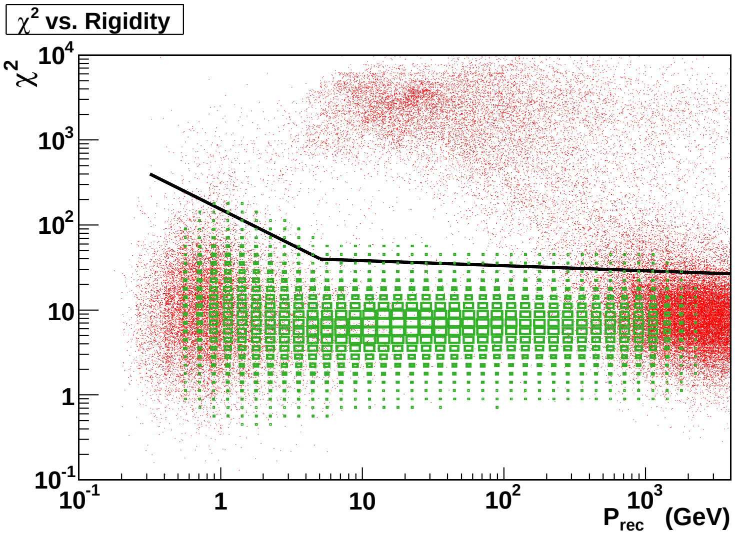

Figure 5.16: *Distribution of χ^2 from the fast fitting algorithm used in pattern recognition versus reconstructed momentum for Good and Neg protons (respectively green boxes and red points); entries above the black line are rejected. It should also be noticed that in the plot relative to Good protons we only showed the cells with more than 600 entries, while no restriction was put on the plot of the Neg ones.*

relaxed rejection at this stage is about 7%, 22% and 57% respectively for the *Good*, *Bad* and *Neg* particles.

5.2.7 The χ^2 cut

The last of our cuts that relies only on TRACKER information is based on the value of the χ^2 of the fit. As explained in section 5.2.1 the pattern recognition stage of event reconstruction involves several fits of increasing accuracy for the identification of tracks and the evaluation of the rigidity.

The conditions to accept the first fits results (namely the linear fit on the (x,z) plane and the circular fit on the (y,z) one), are quite loose, in order to retain as much track candidates as possible. The final and more accurate fits performed to compute the actual trajectory, hence the charge sign, do not necessarily yield a lower value of χ^2, than the previous ones, because now we are using a more stringent fitting model. In fact we find that huge values of χ^2 are possible at the last stages of event reconstruction, as shown in figure 5.16.

The high values are almost all in the range $1 \div 300\ \mathrm{GeV}$ and are primarily associated with *Neg* protons and clearly separated from the rest. *Neg* particles with low χ^2 concentrate in two areas at the edges of the momentum generation range. Below a few GeV, both the *Neg* and *Good* particles feature a wider distribution, with values of χ^2 up to about 100 due to the effect of Coulomb scattering for the *Good* population, while the *Neg* found in this region still contain a relevant contamination of particles produced in interactions with the detector. At the other end of the momentum interval, the two populations are more distinguishable, though a considerable amount of *Neg* protons are compatible with a proper reconstruction. The trajectory is so rigid (in the TeV region in fact) that even if the curvature is wrong, the reconstruction deviates of a small amount from the real one.

We implemented this cut defining a curve that borders the bulk of the *Good* protons distribution and rejected everything that lies above that level. The chosen curve is displayed in the bi-logarithmic scale of figure 5.16 as two black thick segments described by the following analytical equations:

$$\begin{aligned} 2\log\chi &= 2.6 - 0.83 \times (\log \mathrm{P}_{rec} + 0.5) \quad \mathrm{P}_{rec} < 5 \text{ GeV} \\ 2\log\chi &= 1.6 - 0.06 \times (\log \mathrm{P}_{rec} - 0.7) \quad \mathrm{P}_{rec} \geq 5 \text{ GeV} \end{aligned}$$

This condition rejects 36% *Neg* protons ad only 2.8% *Good* ones (*Bad* protons are reduced by $\sim 8\%$).

5.2.8 Anti Coincidence Counters

As described in section 4.2 the trigger algorithm implemented in the early stage of our simulation reflects as much as possible the general needs of the AMS experiment, and is not optimised to select a specific channel. the basic requests imposed for a realistic trigger must be in fact tight enough to guarantee an high live time in the acquisition, while keeping the acceptance as large as possible and flat in momentum for all the particle species.

One of the requests we kept loose on purpose when dealing with the trigger, was the one concerning the number of ACC hits either by particles crossing the TRACKER sideways or by secondaries produced in the interaction with the detector material, especially with the ECAL that is known to produce back-splash particles.

We expect such situations to be harder to reconstruct properly due to the additional particles that enter the scene, so we reconsider this subject to further reduce the charge confusion.

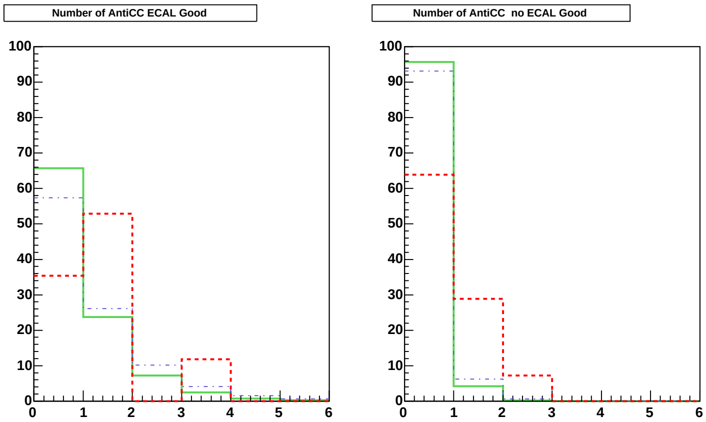

Figure 5.17: *Normalised distributions of the number of* ACC *hits per event for protons with signal in* ECAL *(left plot) and without signal in* ECAL *(right plot).*

In figure 5.17 the normalised distribution of the number of ACC hits per event are shown separately for protons with (left) and without (right) an associated signal in the

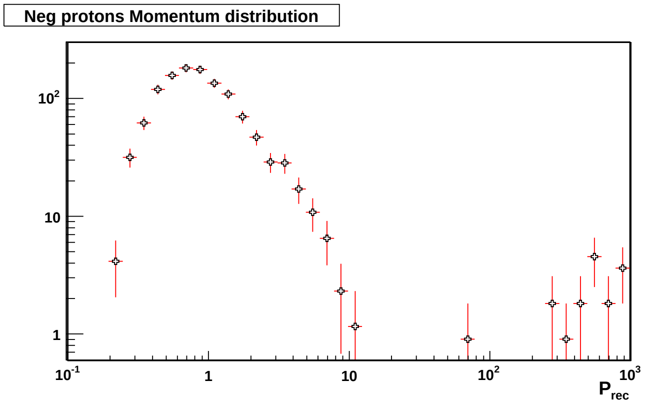

Figure 5.18: *Distribution of reconstructed momentum for the Neg protons after the cuts based only on information from the* TRACKER*. The bulk of the population is in the proximity of* 1 GeV*, and features a tail that extends towards* 10 GeV*; minor components are present above* ~ 70 GeV.

ECAL. From the latter distribution, it is evident that, when the proton did not pass through the ECAL, we can safely reject all events that contain ACC hits as this request rejects $\sim 40\%$ of *Neg* protons while keeping $\sim 96\%$ of *Good* ones . In the case where the ECAL signal is present, the same request on N_{ACC} results in a $\sim 65\%$ rejection of *Neg* protons and $\sim 34\%$ of *Good* ones. However, it should be noticed that this last figures are relevant only for a small fraction (5%) of the total sample. This is due both to the small geometrical acceptance of the calorimeter and to the fact that back-splash events are partially rejected also by the *near-hits* cut.

5.2.9 Velocity momentum consistency

As most of the *Neg* protons which survived the cuts described in the previous sections are mainly grouped at reconstructed momenta around 1 GeV, with tails up to 10 GeV (see figure 5.18), a simple and powerful criterion to reject them is provided by the relation that links the particle momentum to its mass and velocity.

$$\beta = \frac{\mathrm{P}}{\sqrt{\mathrm{P}^2 + m^2}} \ . \tag{5.2}$$

As soon as the mass m is chosen to be that of the proton, equation (5.2) becomes a constrain on the acceptable value of β for a proton of given P.

AMS measures both momentum and velocity of the particles: the first using information taken from the TRACKER alone and the second combining the track length with the TOF measurement. Since the TOF determination is nearly independent of the TRACKER data, we expect that a mis-reconstructed track will have an associated β that is not consistent with the reconstructed momentum.

The green points in figure 5.19 represent the distribution of β as a function of reconstructed momentum for the properly reconstructed protons, that closely follow the relation 5.2 within the experimental error. As expected the poorly reconstructed particles tend to populate a different region of the $(\mathrm{P}_{rec}, \beta)$ plane. In fact, for most of the *Neg* particles (red boxes) the reconstructed momentum is much lower than the real one: they are effectively measured as relativistic, with a $\beta \sim 1$.

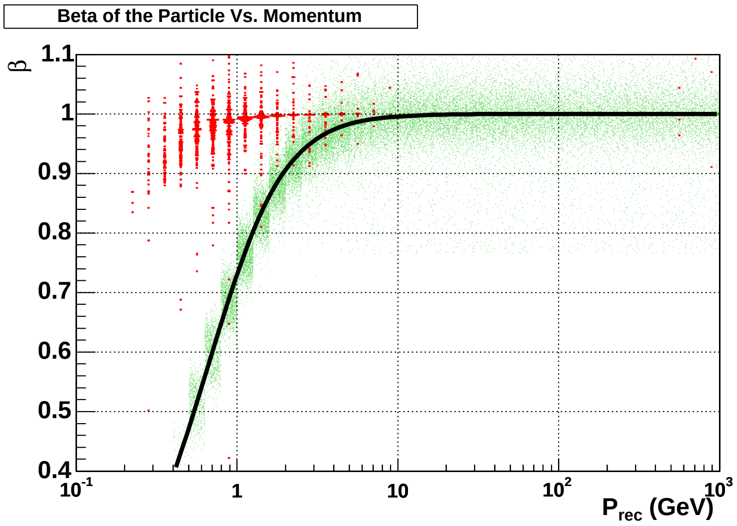

Figure 5.19: *Distribution of β as a function of reconstructed momentum for Good protons represented by the green points, and Neg protons represented by the red squares. The two populations are well separated up to about* 1.6 GeV*, as Negs tend to have a velocity determination quite near 1 while Goods closely follow the theoretical relation (also shown as a thick black line). It is possible to set up an acceptable cut criterion up to about* $3.16 \div 4$ GeV.

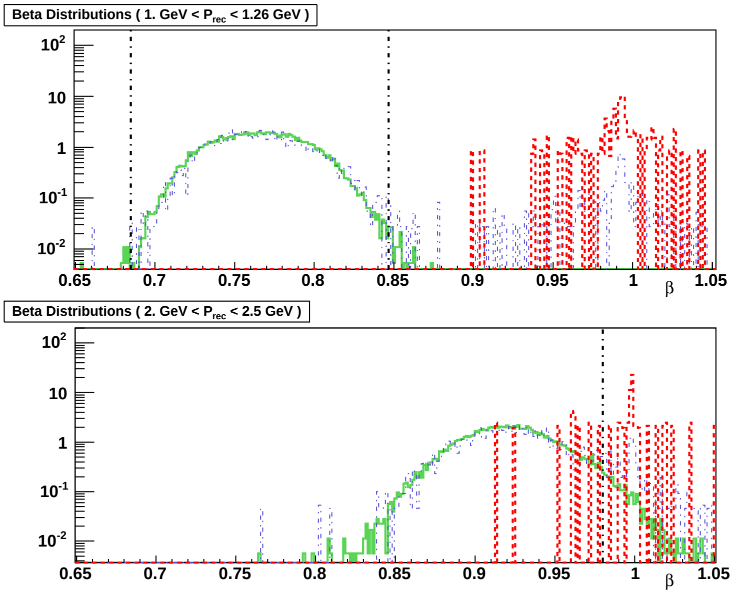

Figure 5.20: *On the upper panel is shown a slice of figure 5.19 corresponding to the momentum range* 1 GeV $< P_{rec} < 1.26$ GeV*: at lower momenta, the separation between Good and Neg is such that we can safely cut at the level of* $3\sigma_\beta$*, the two vertical lines show the limits used to cut Neg particles in this energy bin. On the lower panel the same distributions are reported for the range* 2 GeV $< P_{rec} <$ 2.5 GeV*: above* 1.58 GeV*, the Good and Neg populations are overlapping and the value of* β_{cut} *has to be determined bin by bin.*

P range	Cut level	Cut out fraction (%)		
		Good	*Bad*	*Neg*
1.58 GeV $< \mathrm{P} < 2.$ GeV	$0.8 < \beta < 0.9$	24.5	34.1	100
2.0 GeV $< \mathrm{P} < 2.5$ GeV	$0.83 < \beta < 0.945$	18.5	25.5	95.0
2.5 GeV $< \mathrm{P} < 3.16$ GeV	$0.4 < \beta < 0.98$	13.0	22.0	71.3
3.16 GeV $< \mathrm{P} < 4.$ GeV	$0.4 < \beta < 1.0$	12.2	16.6	18.8

Table 5.2: *Details for the cuts using the β from the* TOF.

The selection of *Good* and *Bad* particles on the basis of their distribution in the $(\mathrm{P}_{rec}, \beta)$ plane, is clearly momentum dependent: as the momentum increases, the protons tend to become relativistic and the finite momentum and velocity resolutions are not enough to test the mass hypothesis.

At low reconstructed momenta ($\mathrm{P}_{rec} < 1.58$ GeV) the β distribution obtained for protons in different P_{rec} intervals is approximately Gaussian as shown on the upper panel of figure 5.20. The *Neg* and *Good* populations are clearly separated by asking the velocity estimate from equation (5.2) to be compatible with the measured velocity. the cut applied is therefore $|\beta_{meas} - \beta_{ideal}| < 3\sigma_\beta$, resulting in a full rejection of all *Neg* protons.

Above the 1.58 GeV limit, the two populations overlap increasingly as exemplified on the lower panel of figure 5.20, so we tuned the cut bin by bin until above 4 GeV, this selection criterion cannot be used anymore. The actual values of the cut limits and rejected fractions are detailed in table 5.2.

It should be noticed, that also electrons have a velocity determination compatible with the speed of light, so this condition is also well suited to remove electron contamination. The reduction of the electron population after the application of this cut varies from total rejection below 0.1 GeV to 49% of surviving particles at about 4 GeV. Only a few permille electrons survive between 0.1 and 2 GeV.

5.3 Electron rejection

As stated before, electron events can mimic anti-protons in case the mass determination is wrong. We already implemented a cut that effectively rejects electron contamination at low momentum in section 5.2.9, as the same criterion also identifies protons reconstructed with the wrong charge sign. However the mentioned cut acts only on particles with reconstructed momentum up to about 3 GeV and much less effectively until P_{rec} reaches approximately the 4 GeV threshold and the aim of our analysis is the detection of a DM signal in the tens of GeV region. Other track selection cuts have of course an effect on the electrons population as for instance the consistency check between half tracks (see section 5.2.3), but the effect is only a reduction of a factor two or so, while we need it to be at least three orders of magnitude.

It is therefore necessary to find some other means to reduce the e^- contamination using information independent of the TRACKER, that can only measure the particle momentum and charge via the curvature in the magnetic field, and the energy deposited in the Si detectors.

Such means are provided by the external sub-detectors of AMS, namely the Transition Radiation Detector, the Ring Imaging Čerenkov and the Electromagnetic Calorimeter. The physics involved in the operation of each one of these detectors are different, but they share as a common denominator that they react to electrons and protons in quite distinguishable ways.

The acceptance of the mentioned detectors is a limiting factor to their utilisation, in particular for the ECAL, that features both a small area and a reduced FOV with respect to all other detectors. The signal that is most likely to be available is the one from the TRD, that is why the request of TRD signal was included in the preselection criterion in section 5.1. At the trigger simulation level, about 56.8% of electron events and 33.7% of proton ones produced a signal in the RICH, relative to the preselection, while in the case of ECAL the yield was about the same for both particles with a value around 18.5%.

5.3.1 Transition Radiation Detector

The key feature of transition radiation emission is that the amount of energy it releases in the form of photons, depends on the particle's energy. More precisely we have that a particle of charge eZ with energy γm releases

$$I = \alpha z^2 \gamma \hbar \omega_p / 3 \ , \tag{5.3}$$

where the plasma frequency ω_p and α are constants of the material being traversed. As the emission is $\propto \gamma$, the difference in mass between electrons and protons implies that the former releases in the TRD straw tubes much more energy than a proton with the same total energy.

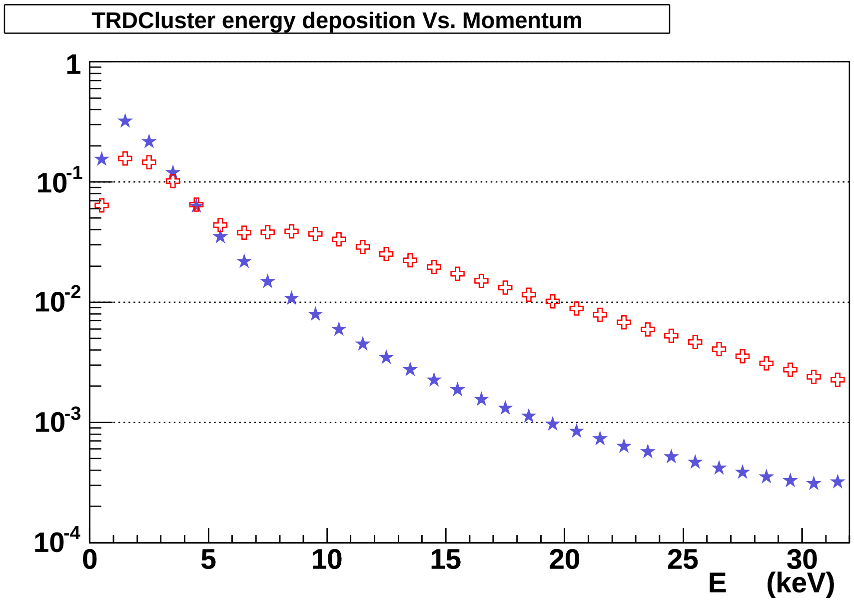

Figure 5.21: *Energy deposited in the straw tubes of* TRD*, restricted to the tracks associated to the reconstructed particle. The blue stars refer to protons, the red crosses to electrons. The peaks below* $5div6$ keV *are due to the normal* $\mathrm{d}E/\mathrm{d}x$*; above that threshold the transition radiation effect is evident for electrons, less so though present for protons.*

In figure 5.21 are plotted, both for e^- and p, the histograms of energy deposited in the single clusters used to build the TRD track associated to the reconstructed particle, which is essentially the same as the energy detected in a single straw tube, since about 96% of the clusters contains only one tube.

Both distributions are peaked at low values where the usual ionisation energy loss is dominant, but as expected about 50% of the electron signals are found above $\approx$6 keV, as opposed to only 13% of the proton ones. Since in principle all the clusters that belong to a track are produced by the same particle, and represent independent determinations of the γ parameter, we can use them to build a quantity that characterises the track (the particle) as a whole. Making use of several (up to 20) independent measures, the effectiveness in particle identification is much improved. Roughly speaking, if we consider an energy deposition $\mathrm{E}_{dep} > 6$ as an indication of electron event then after the binomial distribution, in a 20 hits TRD track we expect to find on average 10 such hits if the particle was actually an electron and only 2.6 if it was a proton instead. Actually the probability that a proton yields 8 high energy hits or more is only 2.4‰ opposed to the 8.7% of electron tracks.

Since the number of hits per TRD track is liable to vary from event to event, and we rely on having a significant number of them, we checked its distribution (see figure 5.22). In both the electron and proton sample, the distribution is peaked around 19 hits, while tracks with less than 16 represent about 10% of the total. In order to ensure an high degree of redundancy in the measurement of the energy deposition and achieve a better identification power, we decided to cut out this 10%.

Besides setting a basis for the subsequent analysis, this cut also affects the level of charge confusion in the protons sample, especially in the low momentum region ($\mathrm{P} < 20\,\mathrm{GeV}$), where 48.7% of *Neg* protons are rejected. This is to be expected on the consideration that setting the minimum number of hits of a track, automatically excludes the cases where the signals from the first layers are missing, as it happens when an impinging proton interacts after a few TRD layers, and produces secondary particles.

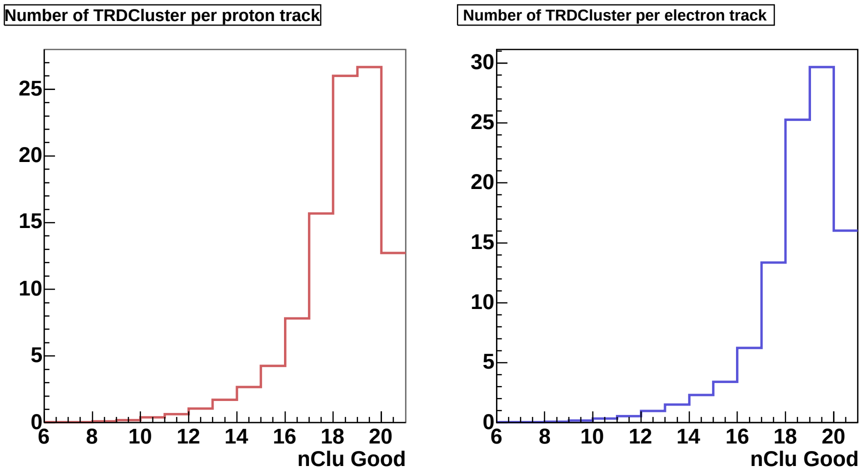

Figure 5.22: *Number of* TRD *hits per track for protons on the left and for electrons on the right. In both cases the tracks with less than 16 hits amounts to about 10% of the total.*

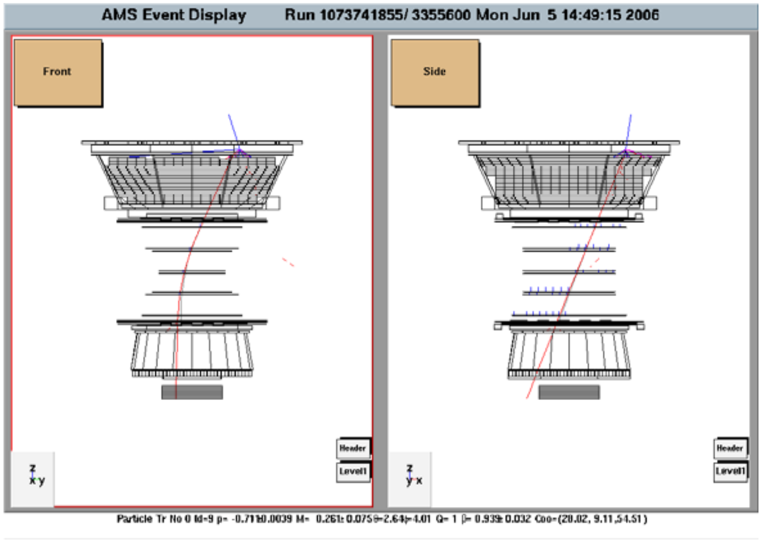

```
Particle Tr No 0 Id=9 p= -0.711±0.0039 M= 0.261±0.075θ=2.64φ=4.01 Q= 1 β= 0.939±0.032 Coo=(20.02, 9.11,54.51)
```

Figure 5.23: *Example of interaction events that escape the cuts discussed up to section 5.2.6 described cuts. The particle produced in the very first parts of the detector is an electron.*

These secondaries are less massive than the original proton and are therefore likely to emit transition radiation in the following layers. More generally, we can expect that the cuts we are going to implement for the reduction of electron contamination, will actually cut out events where only one of the secondary particles (mainly pions), go through the TRACKER surviving the cuts discussed in section 5.2.6, as is the case for the one displayed in figure 5.23.

5.3.2 Truncated mean

The option we considered for the actual implementation of the rejection criterion is to use the mean value of the energy deposition ($\langle \mathrm{E}_{dep} \rangle$) along the TRD-track. In the calculation of the average, the smallest an the biggest values of E_{dep} were discarded. The use of the truncated mean $\langle \mathrm{E}_{dep} \rangle_{tr}$ eliminates data that possibly come from the tails of the distributions, and allows to reduce the spread of the data used for the evaluation of the mean value itself.

In figure 5.24 the distributions of $\langle \mathrm{E}_{dep} \rangle_{tr}$ Vs. P_{rec} for both electrons an protons are displayed.

We notice that at lower momenta the electron population is almost entirely suppressed by the action of the cut on β discussed in section 5.2.9 for the rejection of *Neg* protons . For values of reconstructed momentum $\mathrm{P}_{\mathrm{rec}} > 2 \div 3\ \mathrm{GeV}$, the bulks of the two distributions are well separated, with only a slight overlap. With increasing momentum, also the protons radiate more and more, as testified by the progressive increase of $\langle \mathrm{E}_{dep} \rangle_{tr}$, until they become virtually indistinguishable from electrons around the TeV region, where the electron statistics are small anyway.

The cut level we set, follows as closely as possible the shape of the proton population bulk in order to reduce the electron sample as much as 3 orders of magnitude; the chosen levels are shown in the figure as a line and detailed in table 5.3.

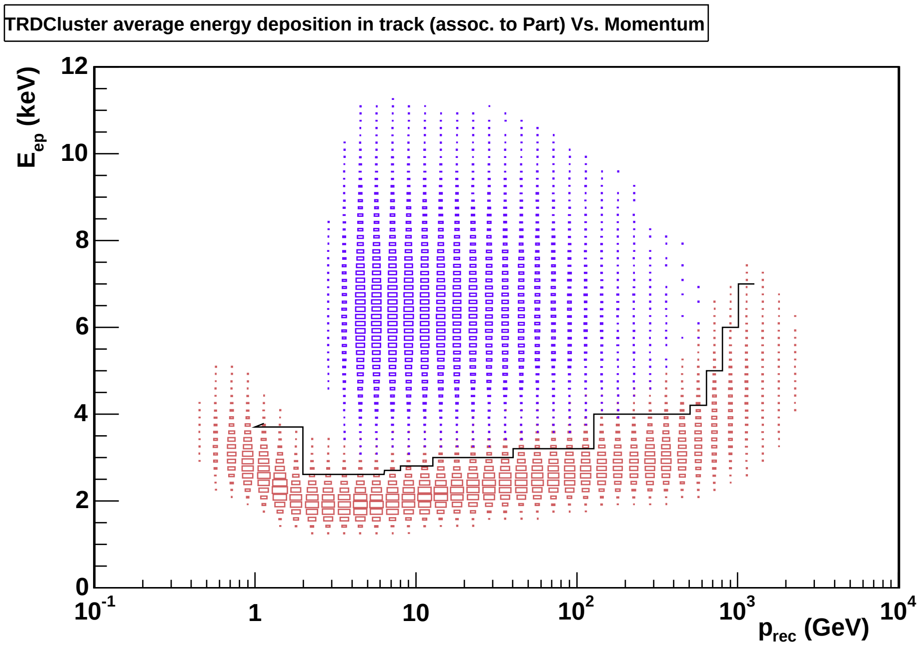

Figure 5.24: *Plot of energy deposition truncated mean* $\langle \mathrm{E}_{dep} \rangle_{tr}$ *Vs. reconstructed momentum for* p *(blue boxes) and electrons (blue boxes); the two distributions are normalised to 100.*

Momentum range (GeV)	Max. $\langle \mathrm{E}_{dep} \rangle_{tr}$ (keV)	Rejected e^{-} (%)	Rejected p (%)
… ÷ 1.		0.	0.
1.00 ÷ 2.0	3.7	97.1	6.30
2.00 ÷ 6.31	2.6	99.8	13.4
6.31 ÷ 7.94	2.7	99.8	15.6
7.94 ÷ 12.59	2.8	99.7	13.4
12.59 ÷ 39.81	3.0	99.5	16.2
39.81 ÷ 125.89	3.2	99.3	21.7
125.89 ÷ 501.19	4.0	96.2	11.0
501.19 ÷ 630.96	4.2	95.4	26.5
630.96 ÷ 794.33	5.0	85.4	20.6
794.33 ÷ 1000.0	6.0	63.4	14.0
1000.0 ÷ 1258.92	7.0	42.5	9.0
1258.92 ÷ …		0.	0.0

Table 5.3: *Implementation details of the* $\langle \mathrm{E}_{dep} \rangle_{tr}$ *cut. Up to* ~ 126 GeV *the cut reduces of a bout three orders of magnitude the number of electrons, at the cost of 20% of the protons. Above* 126 GeV *the cut loses efficiency, however this is not a concern as the electron spectrum is steeper than the proton one.*

5.3.3 Velocity consistency using the RICH

The electron rejection achieved so far ($\mathcal{O}(10^{-3})$) is not good enough to measure the anti-proton flux with such an accuracy that allows to discriminate the presence of SUSY signals that gives contributions at best of a few percent to the total, so we must consider other options to further reduce the electron contamination.

Among the other sub-detectors of AMS, namely the RICH and the ECAL, the former is the one whose acceptance is more close to that of the TRACKER. Roughly speaking,after the TRD cut has been applied, about 38% of proton events produces a signal in the RICH, while for electrons this figure rises to 66%. The difference of the two numbers is due to the fact that low momentum protons travel slower than same energy electrons and are less likely to produce a signal that is successfully reconstructed as a Čerenkov ring. In the event that the ring is reconstructed, the corresponding value of the velocity, would be different in case of electrons and protons, as we already pointed out in section 5.2.9.

The fact that we already imposed a similar condition, does not prevent from using it again because now we are dealing with a different method for the measurement of β that is completely independent from either TOF and TRACKER, so it is still possible to reject those few electrons that survived the cut on β_{ToF}; in addition, since the value of β_{RICH} is far more accurate than the one obtained with the TOF information it turns out that this criterion may be applied over a wider momentum range.

We treated the implementation of the cut in much the same way described in section 5.2.9: the main differences are that we were able to identify only two momentum intervals instead of the four found for the previous cut on the velocity and we could apply it up to ≈ 16 GeV. The projected β distributions for protons ad electrons in the two intervals are shown in figure 5.25. In the lower range ($\mathrm{P}_{rec} \leq 10$ GeV) the cut was

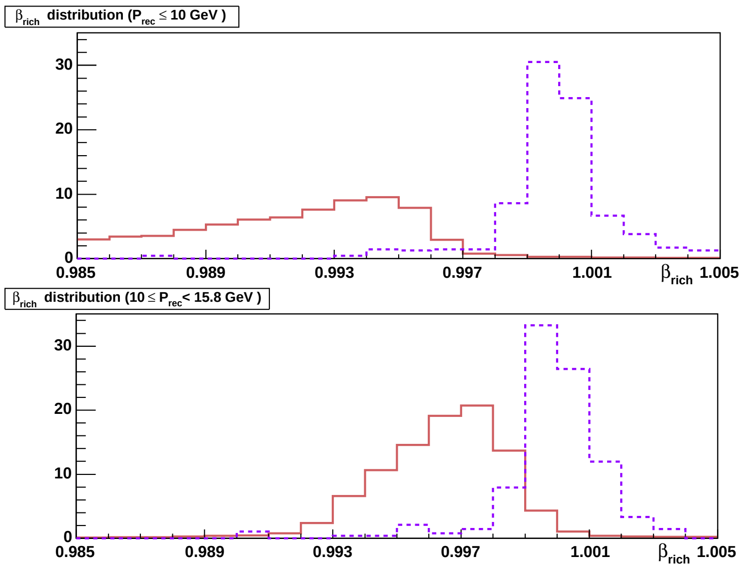

Figure 5.25: *Distributions of* β_{RICH} *for protons (red solid line) and electrons (blue dashed line) in the two regions* $\mathrm{P}_{rec} \leq 10$ GeV *(upper panel) and* $\mathrm{P}_{rec} \leq 10 \div 16$ GeV *(lower panel). The distributions are normalised to 100.*

put at $\beta_{cut} = .997$ rejecting 30.8% of the protons with RICH signal and 80.2% of electrons. In the range $\mathrm{P}_{rec} \leq 10 \div 16$ GeV the two distributions are closer to each other, but it is still possible to set $\beta_{RICH} = 0.999$ as the cut-out level: the rejection percentages are 10% and 81.7% for protons and electrons respectively. At higher momenta – not displayed in figure 5.25 – the distributions overlap more and more and the cut can hardly be applied.

Actually the rejection percentages given above refer to the fraction of events with signal in the RICH, so the discarded particles over all events correspond to lesser fractions. In particular, to account for the lower acceptance of the detector, the rejection fractions found for electrons must be reduced by about two thirds and those for protons by one third .

5.3.4 ECAL energy TRACKER momentum consistency

The last sub-detector of AMS we can use to discriminate electrons and protons is the ECAL. By the very nature of the detector, an electron impinging in it is very likely to begin an electro-magnetic shower that quickly releases (almost) all the particle energy, whereas a proton traversing the ECAL, will typically behave as a Minimum Ionising Particle (MIP). At the energies we are considering electrons are ultra relativistic, so if we take the ratio $\mathcal{R}_{\mathrm{EP}} = \mathrm{E}_{\mathrm{ECAL}}/\mathrm{P}_{trk}$ between the energy measured in ECAL and the momentum determined using the TRACKER, we expect to find a peak around one (in fact $\mathcal{R}_{\mathrm{EP}} = 1/\beta$ in the case of electrons). Since protons release only a minimal fraction of their energy in the ECAL, the relation $\mathcal{R}_{\mathrm{EP}} = 1/\beta$ does not hold and we expect in general low values for the ratio, except perhaps at lower energies, where the protons cease to be MIPs. The distributions of $\mathcal{R}_{\mathrm{EP}}$ for both electrons and protons are reported in figure 5.26 as a function of P_{rec}.

The few electrons surviving the previously discussed cuts (blue markers) are scattered around $\mathcal{R}_{\mathrm{EP}} = 1$, with a spread that is prevalently determined by uncertainties in the measurement of momentum due to the Bremsstrahlung of electrons in the bending field of the spectrometer and to the fact that the ECAL may not contain all of the EM shower. As expected the bulk of the proton distribution (red points) is confined below $\mathcal{R}_{\mathrm{EP}} < 0.1$ for all momenta higher than 10 GeV; below that value we observe the anticipated effect due to the rise of energy release in the fibres.

Since the condition on β implemented in 5.2.9 already removed for the greater part of low energy electrons, it is still possible to implement a cut that follows the shape of the proton distribution bulk as shown by the black line in 5.26.

The effect of this cut is to remove 98% of electrons and 27% of protons however, as for the previously discussed one, the small acceptance of the calorimeter limits the application of this condition to just 14% of protons and 6% of electrons. Requiring the presence of ECAL signal in the event these rejection figures would be effective, but at the price of a drastic acceptance reduction (about a factor ten), so we actually considered two selections: a “loose” one, where the cut displayed in 5.26 is used whenever the event has signal in the ECAL, and a “tight” one, obtained adding as last cut the request that the ECAL signal is present in the event.

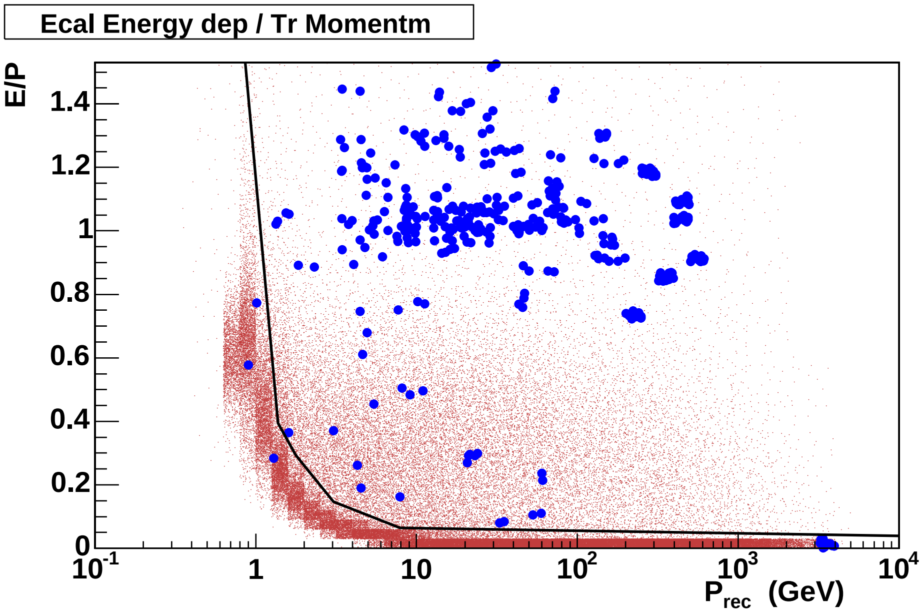

Figure 5.26: *Distribution for* $\mathrm{P}_{rec} > 1\ \mathrm{GeV}$ *of the quantity* $\mathcal{R}_{\mathrm{EP}} = \mathrm{E}_{\mathrm{ECAL}}/\mathrm{P}_{trk}$ *i.e. the ratio between the energy measured in* ECAL *and the momentum determined using the* TRACKER*. Electrons(blue dashed line) cluster around the value 1, as in their case the* $\mathcal{R}_{\mathrm{EP}}$ *equals the inverse of velocity. For protons this is not true since they and in fact nearly 40% of them is found in the first bin i.e. near zero.*

5.4 Residual backgrounds

After the application of all the discussed cuts, we managed to reject the vast majority of *Neg* particles from the proton sample. What is left dwells primarily in the region above $300\ \mathrm{GeV}$, well outside the range where SUSY signals may be expected, however there are still a few events that abide between $1 \div 16\ \mathrm{GeV}$ as shown in 5.27.

A careful analysis showed that in all of these events, the impinging proton underwent an interaction inside the TRD and generated one or more secondaries. One of these secondaries went through the TRACKER and was subsequently reconstructed as a negative particle. In a substantial number of cases the reconstructed interaction product is actually a negative particle and is correctly identified as such, as it happened in the event that is displayed in figure 5.28 as an example.

We notice that in these events, the TRD registers more clusters than those actually used in the TRD-track associated to the reconstructed particle, so we decided to use the ratio between the number of TRD-clusters used in the associated TRD-track (N_u) and the total number of TRD-clusters found in the event (N_{tot}) to distinguish such cases.

The normalised distributions of $\mathcal{R}_U = N_u/N_{tot}$ for *Good*, *Bad* and *Neg* protons are reported in figure 5.29; as expected good protons are packed towards one while *Neg* ones are spread at lower values. Setting the cut-out level at $\mathcal{R}_U = 0.9$ we can reject up to 93% of *Neg* protons though at the expense of 40% of *Good* ones .

We also noticed that the distribution of the square of the mass for the mentioned particles had a large spread, so we considered the possibility to implement a mass cut as a mean to reject the last *Neg* particles. When evaluating m^2 from P and β, we took

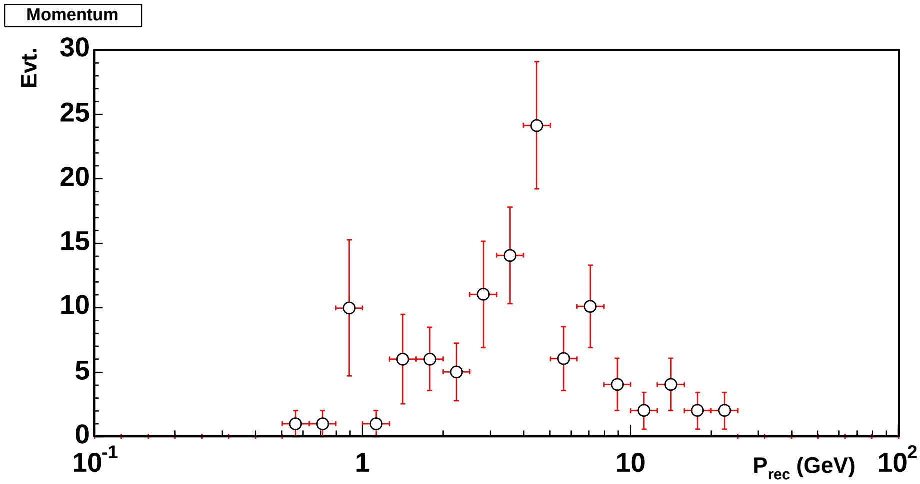

Figure 5.27: *In this plot is shown the* $\mathrm{P}_{rec} < 100$ GeV *distribution for Neg protons after all the previous cuts were applied. A residual population of Neg protons is present.*

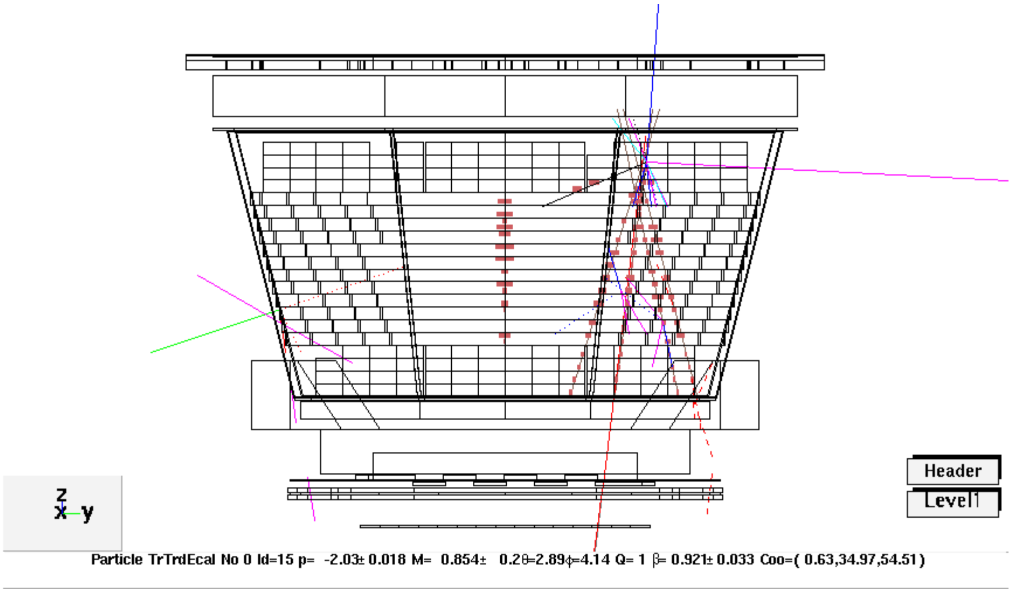

Particle TrTrdEcal No 0 Id=15 p= -2.03± 0.018 M= 0.854± 0.2θ=2.89ϕ=4.14 Q= 1 β= 0.921± 0.033 Coo=(0.63,34.97,54.51)

Figure 5.28: *Event display of a typical event from the population of figure 5.29; we notice the intense activity inside the* TRD *due to the produced secondaries.*

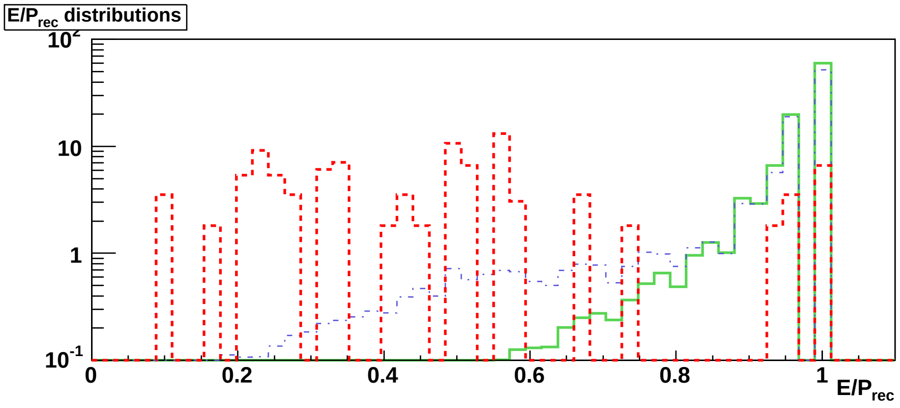

Figure 5.29: *The present plot shows the distributions normalised to 100 of the quantity $\mathcal{R}_U = N_u/N_{tot}$ defined in the text. It is possible to achieve a good separation between Good and Neg particles setting the cut out level at about 0.88 or even .9 if we tolerate an heavier loss of Good protons.*

into account that the velocity of a particle cannot exceed the speed of light by using the value $\beta\prime = 1 - \beta$ instead of the measured β whenever it exceeded one. The distribution of the squared mass is shown in figure 5.30 .

A substantial fraction of the residual background protons has a value of m^2 that exceeds $2\ \mathrm{GeV}^2$ and there is also a tail of low m^2 values in the momentum range $2 \div 6\ \mathrm{GeV}$. We decided to implement a cut based on this distribution that selects only particles whose mass corresponds to the proton one within the spread of the *Good* particles bulk. Since the distribution is asymmetric, so it is the cut implementation that is momentum dependent up to $2.2(2.4)\ \mathrm{GeV}$ for the lower(upper) limit; for higher momenta, up to about $16\ \mathrm{GeV}$, rejecting 50.5% of *Neg* protons and 21% of the signal.

These last two cuts applied together in the relevant range, completely remove the *Neg* contamination in almost all the involved bins.

5.5 Acceptances of the selection

We have described throughout this chapter the various cuts that have been implemented with the goal to reduce the contamination level of the signal that we are interested to measure: namely the CR anti-proton flux, that is liable to include contributions from SUSY Dark Matter annihilation. We now conclude showing the actual performance of the whole set of the discussed cuts when applied to the MC data sample. The relevant quantity we show is the acceptance, that characterises the detector response to the impinging particles, for every given momentum, irrespective of the actual shape of their spectrum.

The acceptances for signal and backgrounds are presented as functions of the generated momentum in figure 5.31 both at the trigger level (black lines) and after the analysis was applied. In particular, the blue lines on the left plots are related to what we obtain without the explicit request of signal in the ECAL (loose selection); the result we obtain if the latter request is also applied (tight selection) is shown on the right part of the figure with a green line. The ECAL request reduces the signal acceptance

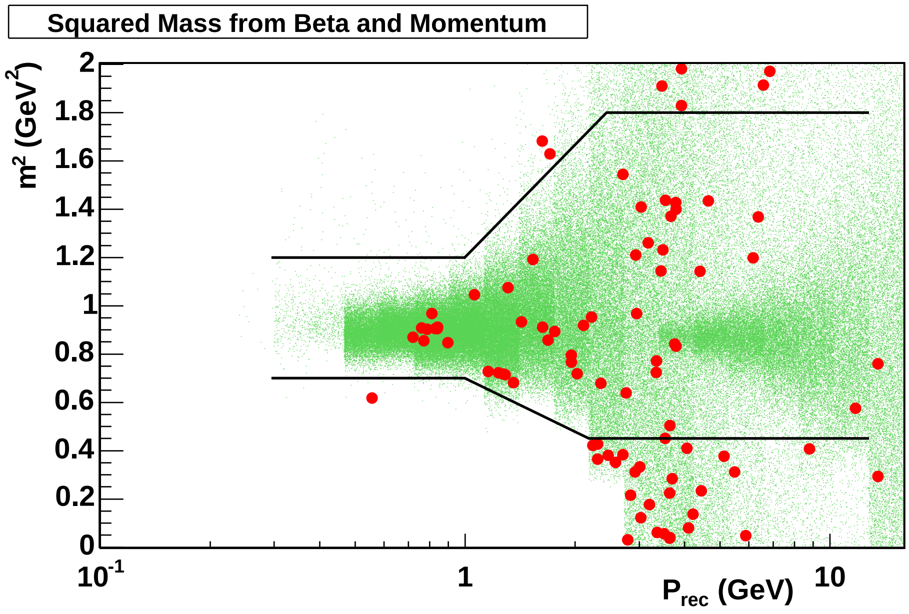

Figure 5.30: *Distribution of m^2 for Good and Neg protons as a function of reconstructed momentum. The m^2 was evaluated from P and β, substituting $\beta\prime = 1 - \beta$ whenever the measured β exceeded one; events outside the band delimited by the black lines were rejected.*

by about a factor ten, but also brings the background ones to zero over a wide momentum range for both *Neg* protons and electrons. In the parts of the spectrum where no background events survived the selection, we report the corresponding 95% C.L. upper limit, that is shown by the upside-down triangles in figure 5.31.

These acceptances are the basis for the discussion of AMS detection capabilities that is the subject treated in the next chapter.

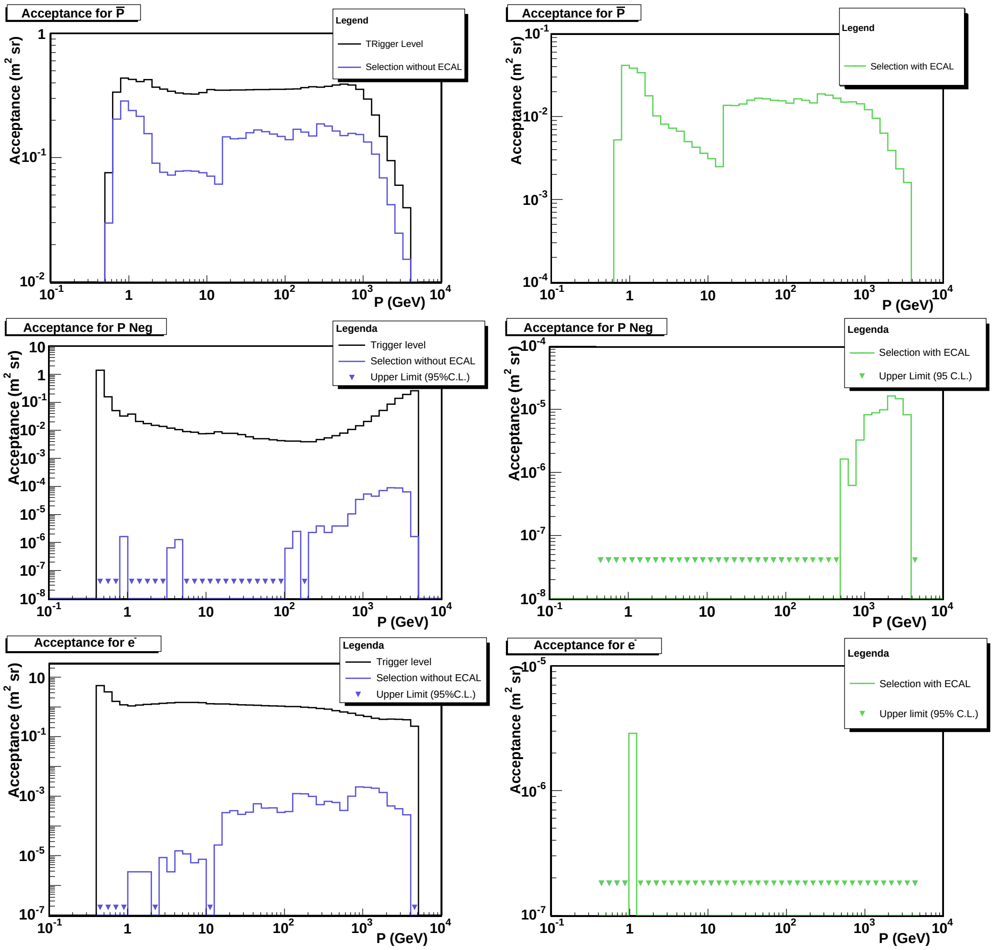

Figure 5.31: In this figure the acceptances of AMS *with our analysis are reported for signal and backgrounds. From top to bottom the plots refer to the anti-proton signal, the proton background and the electron one. The plots on the left show the acceptance at trigger level (black line) and after the application of our analysis without the explicit request of signal in* ECAL*. The green plots on the right refer to the tight analysis where the* ECAL *request is also applied: in all the plots the upside-down triangles show the 95% C.L. upper limit on the acceptance for those bins where the estimated background is zero. The* ECAL *request would virtually bring to zero the backgrounds over most of the observable momentum range though decreasing by a factor ten the signal acceptance.*

Chapter 6

Anti-proton flux measurement

The statistical accuracy that can be reached by AMS in measuring a CR spectrum, depends directly on the number of events collected for that particular species. This number is a function of the time of exposure, the AMS acceptance and the intensity of the flux for each species.

In fact, to a given flux of particles going through AMS, corresponds a counting rate in the detector, that is in general a function of the particle momentum. Multiplying the rate by the exposure time of the experiment, we can estimate the statistics the detector will collect for each momentum bin during its operation, thus determining the accuracy of the measurement; the first step in our discussion of AMS detection capabilities is, therefore, to estimate anti-proton counting rates that are expected using the analysis that we applied to the AMS Monte Carlo data in the previous chapter.

This analysis allows to extract the anti-proton signal from the huge background coming from mis-reconstructed protons and electrons; we will see how, for the purpose to perform an accurate measure of the anti-proton spectrum, it is sufficient to consider the loose version of the analysis (see section 5.5), while for the more challenging task to identify DM signals it will be necessary to use the tight version, where the additional request that the particle leaves a signal in the ECAL is added.

To evaluate the AMS capability to distinguish in the anti-proton spectrum a deformation induced by a neutralino dominated DM, we consider the anti-proton signals resulting from neutralino annihilation as evaluated in reference [84], for three different kinds of SUSY models in the specific case of $m_\chi = 300$ GeV.

In the last section of the chapter, following the prescription also proposed in [84], we have extended our evaluation to the wider range of neutralino masses $m_\chi = [100 \div 600 \text{ GeV}]$.

6.1 The expected rates

In section 5.5 we presented the AMS acceptances for an analysis aimed to select a clean $\bar{\mathrm{p}}$ sample: in order to evaluate the anti-proton counting rate that AMS will observe, these acceptances must be convolved with a realistic anti-proton spectrum.

This convolution must account for the finite momentum resolution of the detector, that allows particles of generated momentum P_{gen} to be measured with different values of reconstructed momentum P_{rec}.

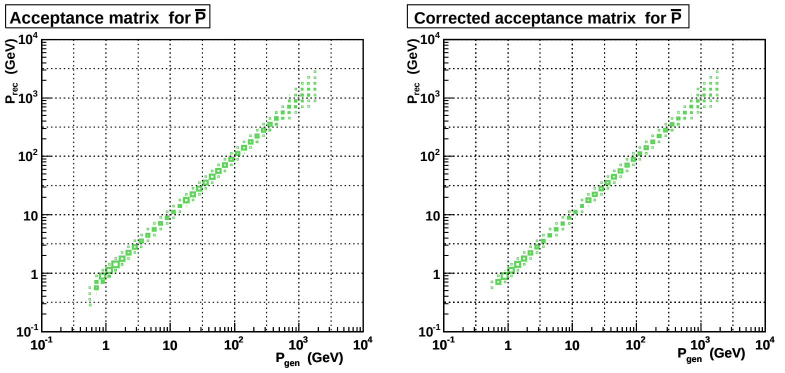

Figure 6.1: Histograms representing the acceptance matrices for $\bar{\mathrm{p}}$ *before (left panel) and after (right panel) the correction for the higher energy loss at low momenta was applied; bins on the* x *axis correspond to rows of the matrix, bins on the* y *axis to columns.*

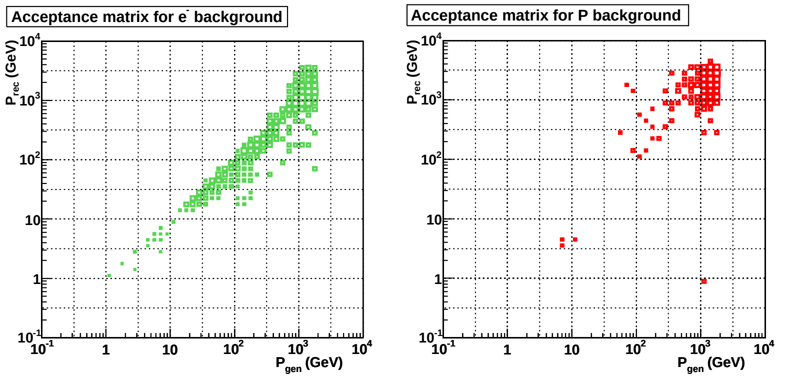

Figure 6.2: Histograms representing the acceptance matrices for the e^- *(left) and* p *(right) backgrounds.*

The relation between P_{rec} and P_{gen} has been represented with a matrix which is filled with the events passing our analysis, so that each cell contains the C_{ij} particles generated with momentum $(\mathrm{P}_{gen})_i$ and reconstructed with momentum $(\mathrm{P}_{rec})_j$; the cells limits have been chosen to have a uniform spacing in logarithmic scale, thus matching the binning of the distributions presented throughout chapter 5.

Scaling the rows of this matrix according to the prescription applied in section 4.1.2 to evaluate the acceptance, we obtain what we call the acceptance matrix, whose elements are defined as:

$$\mathrm{A}_{ij} = \mathrm{A}_{gen} \times \frac{\mathrm{C}_{ij}}{N_{gen}\frac{\Delta\mathrm{P}_i}{\Delta\mathrm{P}_{gen}}} \ , \tag{6.1}$$

where $N_{gen} \cdot (\Delta\mathrm{P}_i/\Delta\mathrm{P}_{gen}) \equiv n_{gen}$ is the number of particles generated in the i-th bin.

The result of our analysis is summarised by the three acceptance matrices corresponding to the anti-proton signal (figure 6.1 on the left) and to the proton and electron backgrounds (figure 6.2 on the right and left respectively). Since our aim is to select well reconstructed anti-protons, we expect the signal acceptance matrix to be almost

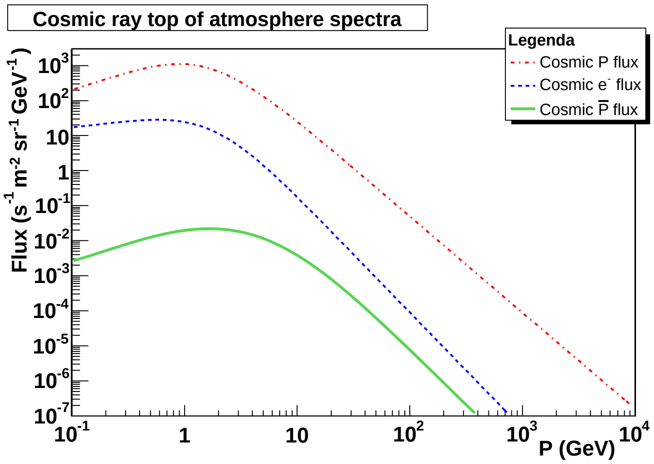

Figure 6.3: *TOA spectra for protons (dash-dotted red line), electrons (dashed blue line) and anti-protons (solid green line). The electron and proton spectra are fitted on the data of AMS-01, the anti-proton one is taken from reference [84].*

diagonal, however, low momentum protons are systematically reconstructed with an underestimated momentum. This feature is a consequence of the energy loss they undergo through the detector (see section 5.2.1). We corrected for this effect all the events with $\mathrm{P}_{gen} < 2$ GeV: the right part of figure 6.1 shows the effect of this correction.

The cosmic fluxes of anti-protons, protons and electrons, must be combined with the corresponding acceptance matrices to obtain the estimated rates in the AMS detector. The fluxes we used for the background components are calculated from a fit to the AMS-01 data collected in the STS-91 precursor flight [149, 150]. The flux of anti-protons must necessarily be a theoretical prediction, since existing experimental measures are affected by large uncertainties and are limited to the low energy region (see section 2.4.2). The $\bar{\mathrm{p}}$ flux we chose is the one calculated in reference [84], which is shown in figure 6.3 along with the p and e^- ones. The choice is motivated by the need to have a coherent picture of all the $\bar{\mathrm{p}}$ flux components involved in the discussion on the SUSY DM signals presented later in this chapter.

To properly evaluate the rate for a given CR species, we apply the relevant acceptance matrix to a vector $\overrightarrow{\Phi}$ which contains the integrals of the species flux evaluated in each P_{gen} bin, according to:

$$\overrightarrow{\mathrm{R}} = \widehat{\mathrm{A}} \cdot \overrightarrow{\Phi} \ . \tag{6.2}$$

In figure 6.4 the calculated rates for the anti-proton signal and the backgrounds coming from mis-reconstructed electrons and protons are shown at trigger level (upper panel) and after the application of the loose analysis (lower panel).

At trigger level the two background rates, marked by the empty red and solid green triangles, overwhelm the signal. After our analysis has been applied, the backgrounds are significantly reduced, representing no more than a few percent of the anti-protons flux over most of the observable momentum range; in particular they are negligible for momenta below 100 GeV, while above this threshold they tend to approach the signal level and must therefore be subtracted.

Considering three years of data taking, which corresponds to about 10^8 s, AMS

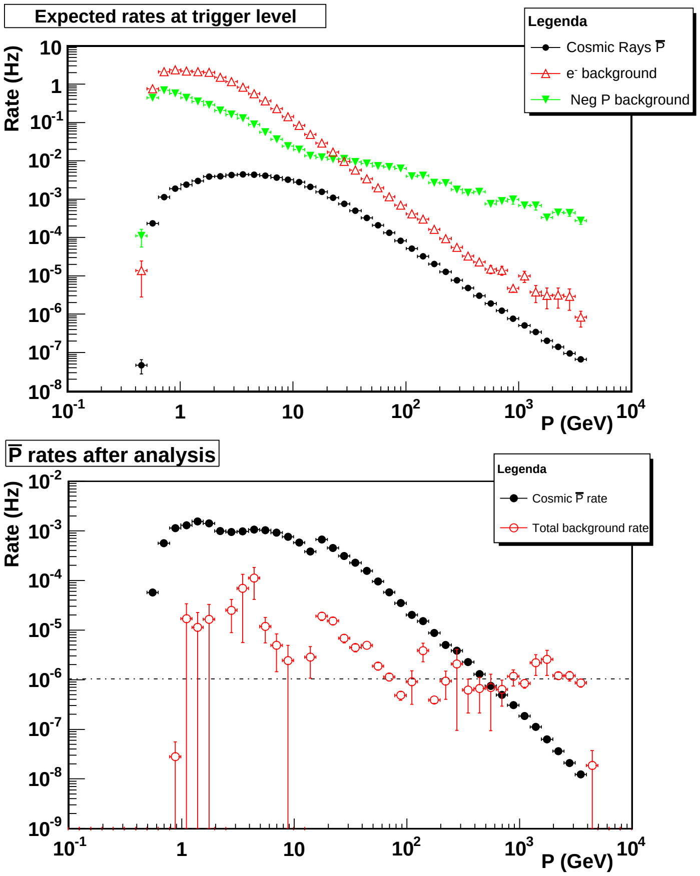

Figure 6.4: *On the upper panel the expected rates for the anti-proton signal (black circles) and the electron and proton backgrounds (empty red and solid green triangles respectively) at trigger level: both backgrounds are much higher than the signal. On the lower panel are reported, with solid black circles, the* $\bar{p}$ *rates obtained applying our analysis without imposing the* ECAL *condition; the total background is also reported with the corresponding empty marker. The dash dotted line marks the rate that would yield a 100 particles count in a given momentum bin over the three years of operation of* AMS.

will perform an accurate measurement of the anti-proton spectrum up to momenta $\sim 500\,\mathrm{GeV}$, where the statistical error will be $\sim 10\%$.

6.2 The anti-proton flux

The evaluated rates describe the response of AMS to the impinging anti-proton flux, however, they are specific to the detector and cannot be directly compared to other experimental and theoretical results. It is then preferable to express the measured rates in terms of the originating flux.

To unfold the AMS rates from the dependence on the experimental apparatus and transport them into the flux domain, it is necessary to invert the calculation of equation (6.2): this is in general a non trivial task that can be approached in several possible ways [151].

The natural choice would be to simply invert the acceptance matrix and apply it to the vector of rates:

$$\overrightarrow{\Phi} = \widehat{\mathrm{A}}^{-1} \cdot \overrightarrow{\mathrm{R}} \ . \tag{6.3}$$

This approach has the advantage to produce an unbiased result, but it has also some defects: it can only be applied to a square matrix and the variance of the results depends critically on the binning of the matrix itself. As discussed in [151], among the unbiased methods, the matrix inversion is the one which introduces the smaller variance, since it is equivalent to the maximum likelihood.

To reduce the variance a biased method must be applied, one possibility is to alter the log-likelihood function with the addition of a “regularisation function” $S(\mu)$:

$$\Lambda(\mu) = \alpha \ln L(\mu) + S(\mu) \tag{6.4}$$

where μ stands for the array of expected values for the theoretical integral flux and α sets the relative weight of the data with respect to $S(\mu)$ [152]. The regularisation function must be carefully chosen to keep the value of $\Lambda(\mu)$ within a small interval around the unperturbed maximum likelihood value. The choice of the regularisation parameter is important too: a low value of α introduces a larger bias, while a too large one would reproduce the behaviour of the matrix inversion method.

A different approach is based on an iterative method described in reference [153]. This method uses Bayes theorem to evaluate the probability that a momentum measured in the i-th bin (the effect ε_j) is due to a particle whose true momentum is in the j-th bin (the cause C_i). The formula to apply is:

$$P(C_i|\varepsilon_j) = \frac{P(\varepsilon_j|C_i)P_0(C_i)}{\sum_{\ell=1}^{n_C} P(\varepsilon_j|C_\ell)P_0(C_\ell)} \ , \tag{6.5}$$

where $P(\varepsilon_j|C_i)$ is the probability for the cause C_i to produce the effect ε_j and the $P_0(C_i)$ term represents the probability for the i-th cause to happen.

$P(\varepsilon_j|C_i)$ is proportional to the element A_{ij} of the acceptance matrix from the MC analysis, and the $P_0(C_i)$ term is proportional to the true spectrum that must be reconstructed. If, given the current knowledge on the subject, there exist guess about the shape of the unfolded spectrum, the probabilities $P_0(C_i)$ may be set accordingly, otherwise they should be set according to a uniform spectrum. $P(C_i|\varepsilon_j)$ define the unfolding matrix $\widehat{M}$ through which the flux can be recovered from the rate:

$$\overrightarrow{\Phi} = \widehat{M}^{-1} \cdot \overrightarrow{\mathrm{R}} \ . \tag{6.6}$$

The just evaluated flux is then used to update the values of $P_0(C_i)$ and the whole process is repeated until the unfolded spectrum does not change anymore within a tolerance or a maximum number of iterations is reached[1].

Since we are dealing with MC, where the input spectra are exactly known, the application of any unfolding procedure to the estimated rates has the only purpose to verify the bias introduced by the finite detector resolution.

To this end we simulated a measure of the reference TOA fluxes described in the previous section. We applied the acceptance matrix from the loose analysis and we

---

[1] If the number of iterations grows too much, this method too tends to reproduce the results of the matrix inversion one.

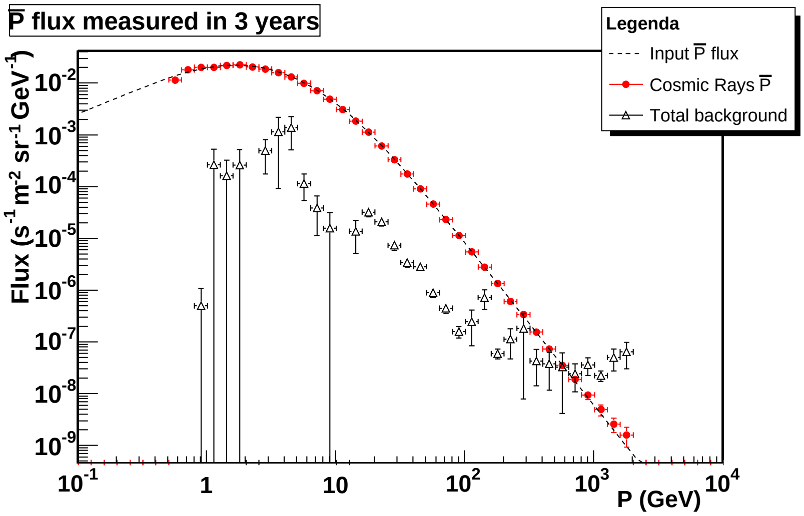

Figure 6.5: *In this figure the input anti-proton flux (dashed line) is compared to its measure as performed by* AMS *in absence of backgrounds (solid circles); the sum of the electron and proton backgrounds contributions is also reported (empty triangles).*

unfolded the corresponding expected rates using a simplified approach. We assumed that the acceptance matrices form our analysis are actually diagonal, which is almost the case as noted in the previous section.

The unfolding algorithm is reduced to the division of the rate by the corresponding element of the matrix diagonal: $\Phi_i = \mathrm{R}_i/\mathrm{A}_{ii}$, which are used as correction factors. This simple unfolding method can yield a smaller variance with respect to the matrix inversion one, however it is known to introduce a bias that tends to reproduce the probe spectrum of the MC simulation used to estimate the corrections themselves [151].

Since the errors on the acceptance matrix are known from the MC analysis, the value of the statistical error on the resulting flux is determined by the number of observed anti-proton events in each bin, that is easily estimated multiplying the rate by the exposure time of three years ($\sim 10^8$ s). The result of the procedure is shown in figure 6.5, where the "measured" $\bar{\mathrm{p}}$ flux is represented by the solid circles, while the empty triangles are used for the total background (e^- and p); we also report the input anti-proton flux (dashed line).

The recovered anti-proton flux shows a quite good agreement with the input spectrum; the bias introduced by the simplified unfolding approach is about 2÷3% over most of the generation range of particle momentum, increasing at high and low momenta. The discrepancy at high momenta is expected, since in that region the MC probe spectrum is much greater than the realistic one, thus yielding a more pronounced bias: moreover at high momenta our assumption that the acceptance matrix is diagonal does not hold, due to the deterioration of the detector momentum resolution. At low momenta the problem is instead represented by the binning that is way too large to adequately sample the steep acceptance decrease caused by the magnetic field cut-off.

6.3 Sensitivity to SUSY DM signals

Now that we have assessed the capacity of AMS to measure the anti-proton flux, it is time to address the issue of the detector sensitivity to DM signals in this channel. Actually the possibility to observe an excess in the $\bar{\mathrm{p}}$ flux depends strongly on three aspects: the kind of SUSY model that is being considered, the DM density profile, which influences the annihilation rate, and the particular choice of the CR propagation model.

As discussed in section 2.4.2, in order to perform a coherent comparison it is necessary that the ordinary anti-proton flux and the SUSY DM contributions are propagated in the same conditions . In reference [84], three signal hypotheses are considered to discuss their respective visibility by means of indirect search experiments. The three proposed SUSY scenarios, labelled by the authors as AMSB, *Funnel* and NUGM, are characterised by different Super Symmetry breaking mechanisms that in turn lead to different weights of the bino ($\widetilde{\mathrm{B}}$), wino ($\widetilde{\mathrm{W}}$) and higgsino ($\widetilde{\mathrm{H}}^0$) components of the LSP (neutralino), as explained in section 2.4.2.

The choice of these schemes is also motivated by the fact that the linear combinations of $\widetilde{\mathrm{B}}$, $\widetilde{\mathrm{W}}$ and $\widetilde{\mathrm{H}}^0$, that define the respective neutralinos, are almost pure states of one among the constituent sparticles, as shown in table 2.1. Since these models describe “extreme” SUSY scenarios, they represent useful benchmark models to test the sensitivity of AMS to DM signals.

The anti-protons from a $300\,\mathrm{GeV}$ neutralino annihilation, that features a typical spectrum for each model, have been propagated through the ISM to reach the Top of Atmosphere. The resulting fluxes are shown in figure 6.6 together with the estimation of the cosmic anti-proton flux we used so far.

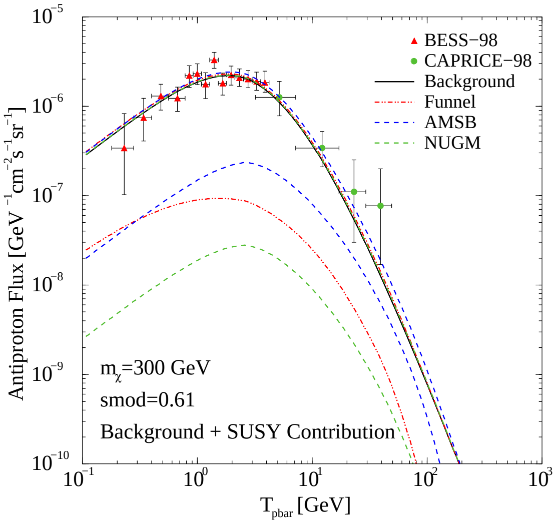

Figure 6.6: *The Solar modulated anti-proton flux, as a function of kinetic energy. The black line corresponds to the calculated background, while the three coloured thick lines to the total signal for the three* SUSY *models at mass* $m_\chi = 300\,\mathrm{GeV}$. *The thin lines correspond to the* SUSY *contributions alone. The data from* BESS *[104] and* CAPRICE-98 *[107] are also shown.*

On the same plot are also reported the available experimental data from BESS [104]

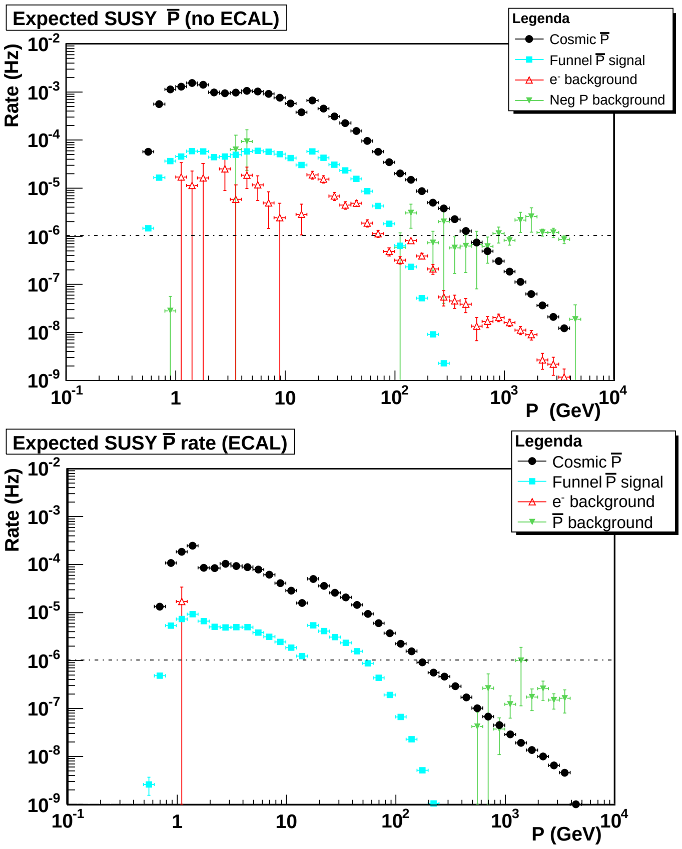

Figure 6.7: *Expected rate for the* Funnel *model compared to the anti-proton one and to the backgrounds. Lower (upper) panel with (without) the* ECAL *request applied.*

and CAPRICE-98 [107]: we notice how the wide error bars do not allow to discriminate the background (secondary) anti-proton spectrum from the SUSY contributions, even in the region around the maximum that is measured somewhat more accurately. AMS on the other hand will have a much smaller statistical error as shown in the previous section and the signals in question could be observable.

In figure 6.7 (upper panel) the rate expected from the *Funnel* signal alone is compared to the cosmic anti-proton rates, as calculated in section 6.1. Since the rate of the *Funnel* model is of the same order of the electron and proton contaminations, it will not be possible to distinguish its contribution to the anti-proton spectrum. However, considering only the events within the ECAL acceptance (i.e. applying the tight analysis), the e^- and p contaminations practically vanish.

As discussed in section 5.5, applying the tight analysis reduces the total acceptance by an order of magnitude; nevertheless, due to the long exposure time of AMS, this reduced value is still acceptable. In figure 6.7 (lower panel) are shown the rates that result from the application of the tight analysis; we notice that an accurate measurement of the anti-proton flux is possible up to $\sim 200\,\mathrm{GeV}$ virtually without any contamination. Furthermore, in the high momentum region, the *Funnel* signal is so faint to be

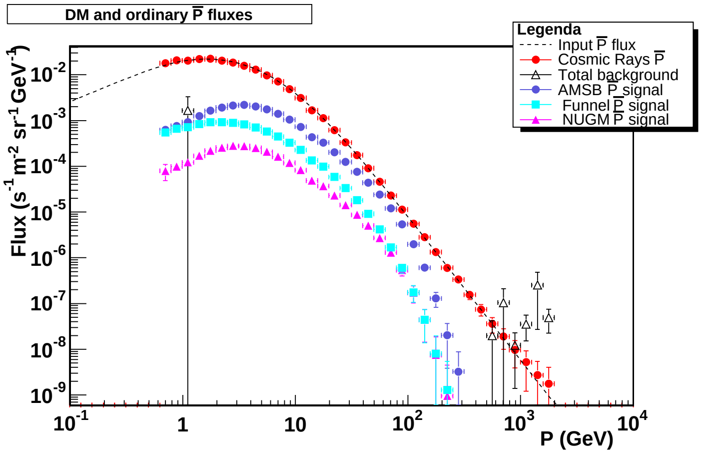

Figure 6.8: *In this figure, the secondary anti-proton spectrum and its electron and proton spurious components, already shown in figure 6.5, are compared to the fluxes that the* AMSB, Funnel *and* NUGM *models would yield by themselves.*

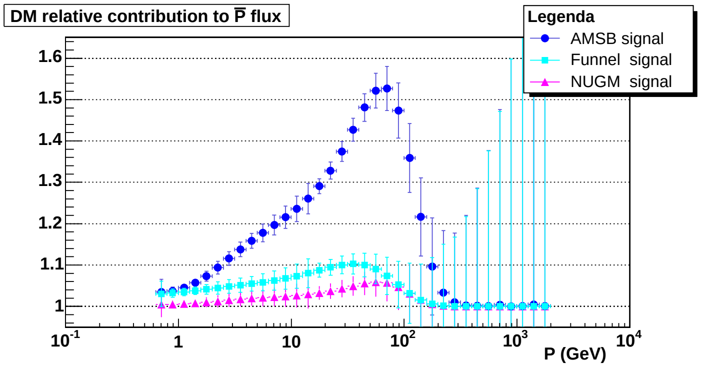

Figure 6.9: *This figure reports for the three considered models the total $\bar{\mathrm{p}}$ flux (ordinary +* SUSY *components) divided by the ordinary signal alone in the case of $m_\chi = 300\ \mathrm{GeV}$.*

hardly observable.

Figure 6.8 reports the fluxes of the three proposed SUSY signals as they will be measured by the AMS detector considering our tight analysis and three years of data taking. These fluxes have been evaluated with the same procedure used in the previous section for the cosmic anti-proton flux, also shown for comparison.

The relative contribution to the anti-proton flux from the DM signals can be appreciated in figure 6.9, where we show the ratio between the total $\bar{\mathrm{p}}$ flux (cosmic + SUSY) and the cosmic component alone.

The AMSB and *Funnel* signals feature a distinct signature, exhibiting a deformation of the spectrum in the momentum range $2 \div 200\ \mathrm{GeV}$. The NUGM signal too introduces some distortion, which is however of the same order of the statistical error at the single bin level.

In order to quantify the significance of these excesses in the $\bar{\mathrm{p}}$ spectrum, we performed a statistical analysis based on a chi square test. Considering three years of data taking and our usual binning of data the $\widetilde{\chi}^2$ is defined as:

$$\widetilde{\chi}^2 = \frac{1}{n_{dof}} \sum_j \frac{\left(\mathrm{C}_j^{\bar{\mathrm{p}}+\mathrm{DM}} - \mathrm{C}_j^{\bar{\mathrm{p}}}\right)^2}{\sigma_j^2} = \frac{1}{n_{dof}} \sum_j \frac{\left(\mathrm{C}_j^{\mathrm{DM}}\right)^2}{\mathrm{C}_j^{\bar{\mathrm{p}}}} \; . \tag{6.7}$$

where $\mathrm{C}_j^{\bar{\mathrm{p}}}$ is the number of events that AMS will collect in the hypothesis of no DM signal, $\mathrm{C}_j^{\bar{\mathrm{p}}+\mathrm{DM}}$ represents those collected if a DM signal is present and $\sigma_j^2 = \mathrm{C}_j^{\bar{\mathrm{p}}}$ is the statistical error on the cosmic anti-proton flux. Defining the integral flux in a bin as:

$$\Phi_j = \int_{\Delta \mathrm{P}_j} \phi(\mathrm{P}) \; \mathrm{dP} \tag{6.8}$$

and using the relation

$$\mathrm{C}_j = \Phi_j \cdot \mathrm{A}_j \cdot t \; , \tag{6.9}$$

we wrote equation (6.7) as:

$$\widetilde{\chi}^2 = \frac{1}{n_{dof}} \sum_j \frac{\left(\Phi_j^{\mathrm{DM}}\right)^2}{\Phi_j^{\bar{\mathrm{p}}}} \left(\mathrm{A}_j \, t\right) \; , \tag{6.10}$$

where the dependence of the $\widetilde{\chi}^2$ on the detector acceptance and exposure time has been made explicit.

We used equation (6.10) to perform the $\widetilde{\chi}^2$ test over the range $1 \div 126$ GeV which corresponds to the region where AMS accuracy is better than 10% applying the tight analysis. The number of degrees of freedom n_{dof} for this test is 21, after the number of bins covering the considered momentum range: for the AMS acceptance we substituted the one evaluated applying our tight analysis and considered an exposure time of three years. The $\widetilde{\chi}^2$ values obtained for the three signal hypotheses are:

$$\widetilde{\chi}^2_{\mathrm{AMSB}} = 197, \quad \widetilde{\chi}^2_{Funnel} = 19.6, \quad \widetilde{\chi}^2_{\mathrm{NUGM}} = 2.7.$$

The values we found for the AMSB and *Funnel* hypotheses are quite large and allow to cleanly identify the respective signatures in the cosmic anti-proton flux, as well as to distinguish between the two kinds of SUSY model. As expected, in the NUGM scenario the signature significance is lower, however, the evaluated $\widetilde{\chi}^2 = 2.5$ sets a C.L. of $\sim 99.99\%$.

6.4 Extension to other χ masses

The results obtained in the previous section indicate AMS excellent capability to identify DM contributions to the anti-proton spectrum in different SUSY scenarios, however the parameters of each model are not univocally determined. In order to have comparable results from the three proposed models, the respective parameter sets were tuned to produce LSPs of the same mass (300 GeV).

Since there is no compelling reason for the neutralino to have precisely this mass, it is of prime interest to extend our considerations to other allowed values of m_χ. This task would require, for each SUSY breaking mechanism, a whole set of coherent predictions for various mass hypotheses; no such parametrisation of the signals was available so we resorted to the alternative approach proposed in reference [84].

As pointed out in equation (6.10), the value of the $\widetilde{\chi}^2$ depends on the detector characteristics through the acceptance and the exposure time, it is however a reasonable approximation to substitute it with its average over the observed momentum range so that:

$$\widetilde{\chi}^2 = \frac{1}{n_{dof}} \sum_j \frac{\left(\Phi_j^{\text{DM}}\right)^2}{\Phi_j^{\bar{\text{p}}}} \cdot \left[\langle \text{A}^{\bar{\text{p}}} \rangle \; t\right] \; . \tag{6.11}$$

In equation (6.11) the terms accounting for the actual experimental setup, namely the acceptance and exposure time, as well as on the binning used for the analysis, can now be factored out of the summation sign, whose argument only depends on the features of the DM signal and cosmic anti-proton predicted spectra.

Assuming that the total number of bins in equation (6.11) is large, with respect to the width of the explored momentum range, and remembering the definition (6.8) of Φ, the summation sign can be satisfactorily approximated with an integral on the theoretical fluxes for ordinary and DM produced $\bar{\text{p}}$, so we can introduce a discrimination parameter defined as:

$$I_\phi = \int_{\text{P}_{min}}^{\text{P}_{max}} \frac{\left(\phi^{\text{DM}}\right)^2}{\phi^{\bar{\text{p}}}} \; \text{dP} \; . \tag{6.12}$$

The discrimination parameter I_ϕ only depends on the parametrisation of signal and background: it estimates the intrinsic degree of discrepancy between the DM signal and the cosmic anti-protons flux, that for a specific experiment would correspond to an observed $\widetilde{\chi}^2$:

$$\widetilde{\chi}^2 = I_\phi \; \cdot \frac{\left[\langle \text{A}^{\bar{\text{p}}} \rangle \; t\right]}{n_{dof}} \; . \tag{6.13}$$

The authors of reference [84], evaluated the I_ϕ parameter curve as a function of the neutralino mass in the three scenarios already discussed: their results are shown in figure 6.10 for both the anti-proton (dashed curve) and positron (dot-dashed curve) signals.

Using equation (6.13) the other way around, we can define the quantity:

$$I_\phi^{x\%} = \frac{(\chi^2)_{n_{dof}}^{X\%}}{\langle \text{A}^{\bar{\text{p}}} \rangle \cdot t} : \qquad \left[(\chi^2)_{n_{dof}}^{X\%} = (\widetilde{\chi}^2)_{n_{dof}}^{X\%} \cdot n_{dof}\right] , \tag{6.14}$$

where $(\chi^2)_{n_{dof}}^{X\%}$ is the chi square value required to discriminate the DM signal at the $X\%$ C.L. with a given number of degrees of freedom n_{dof}. $I_\phi^{x\%}$ represents the value of I_ϕ that allows to obtain the required $X\%$ C.L. using a particular experiment of average acceptance $\langle \text{A} \rangle$ and exposure time t.

The value of $I_\phi^{x\%}$ can be directly compared to the I_ϕ curves of figure 6.10: whenever the relation $I_\phi > I_\phi^{X\%}$ is met, the considered experiment is capable to discriminate the signal with a significance better than the chosen $X\%$.

The couples of horizontal dashed lines in figure 6.10 represent the estimates of $I_\phi^{95\%}$, evaluated in reference [84] for the PAMELA satellite after an operating time of one and three years, assuming for the average acceptance the value of the geometrical one.

We performed this calculation for the three operating years of AMS, using a conservative estimate of $0.01 \text{ m}^2\text{sr}$ for the average acceptance of our tight analysis. Considering the energy range $1 \div 126$ GeV and a 95% C.L. we find:

$$I_{\phi \;\; \text{AMS}}^{95\%} \simeq 3.6 \cdot 10^{-9} \text{ cm}^{-2}\text{sr}^{-1}\text{s}^{-1} \; . \tag{6.15}$$

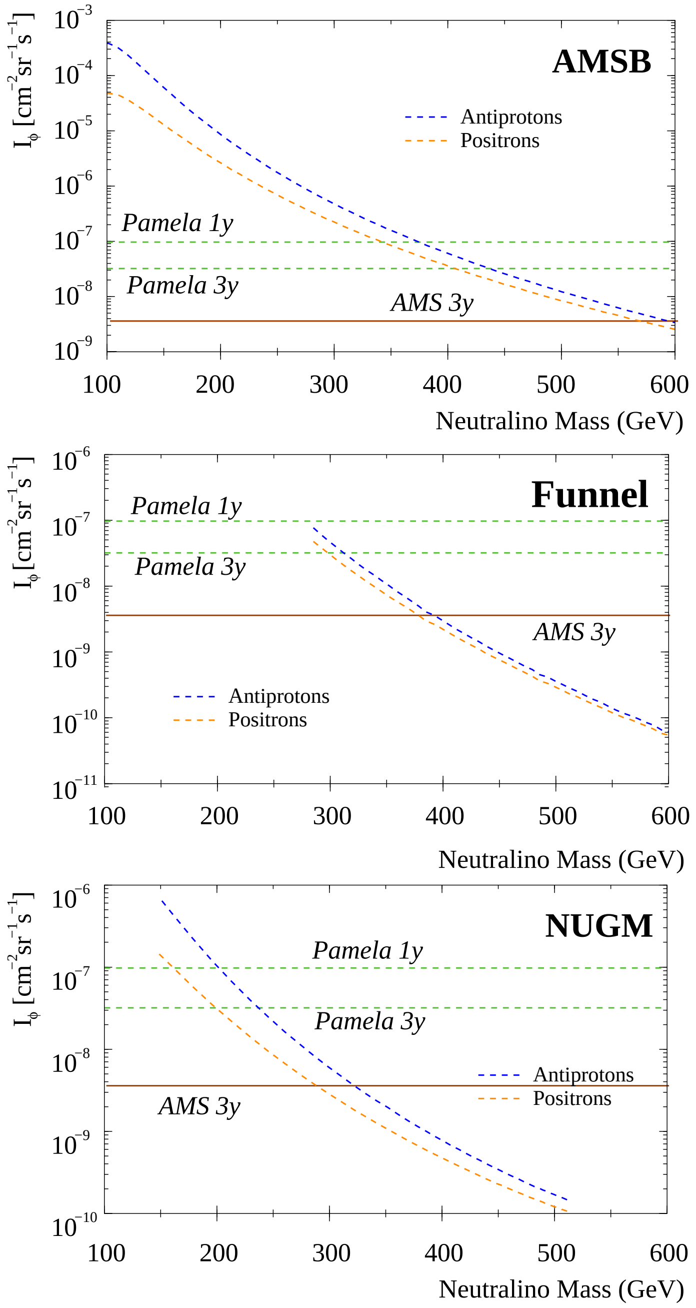

Figure 6.10: *In these plots from reference [84], the I_ϕ parameter is reported as a function of the neutralino mass in each of the discussed* SUSY *scenarios for both the anti-proton (dashed curve) and positron (dot-dashed curve) signals. The pairs of horizontal dashed lines in figure 6.10 represent the estimates of $I_\phi^{95\%}$ for the* PAMELA *satellite after an operating time of one and three years, assuming for the average acceptance the value of the geometrical one. We added to the plots our estimate for the 95% C.L. discrimination parameter of* AMS *in three years of data taking ($I_{\phi\ \mathrm{AMS}}^{95\%} \simeq 3.6 \cdot 10^{-9}$ cm^{-2}sr^{-1}s^{-1}), shown as a solid horizontal line.*

This value is reported in figure 6.10 with solid horizontal lines.

From this estimate we see that AMS will be able to discriminate the corresponding signals over a wide range of allowed neutralino masses, in particular for the case of the AMSB model the whole mass range $100 \div 600$ GeV is accessible. Even in the most unfavourable scenario (NUGM), the explored region corresponds to about the lower two thirds of the above mentioned range.

In our study we focused on the anti-proton channel, however, AMS will actually perform a multi-channel search, probing the presence of DM signals in the cosmic spectra of other charged (e^+,$\bar{D}$) as well as neutral species (γ) discussed in section 2.4.2. The possibility to cross-check the results from all the measured spectra will significantly increase the overall sensitivity to neutralino annihilation signals of the AMS detector.

Conclusions

The design goal of the AMS experiment is to search for anti-nuclei of primordial origin and to measure, with unprecedented accuracy, the abundances and energy spectra of the faintest components of CR, such as anti-protons and positrons.

The relevance of an accurate measurement of such components is twofold: it can be used both to constraint CR propagation models, which describe anti-particles as secondary products of CR nuclei with the Inter Stellar Medium, and to indirectly study the nature of the non baryonic Dark Matter, as a possible source of primary $\bar{\mathrm{p}}$ and e^+.

In this work, we performed a Monte Carlo study to assess the AMS detector performances in what concerns the anti-proton flux measurement, investigating on the resulting sensitivity of this measurement, for Dark Matter searches.

The experimental challenge for such a measurement is related to the faintness of the signal, which requires an efficient detection based on a minimum of selection criteria, and the overwhelming size of the physical and instrumental backgrounds, which would naturally lead to tight quality cuts in the event reconstruction.

Based on a detailed simulation of the AMS response to the passage of $\sim 87 \cdot 10^6$ protons and $\sim 10 \cdot 10^6$ electrons, we developed two sets of selection criteria optimised either for a maximum efficiency in the detection of anti-protons or for a minimum acceptance of the backgrounds

In our work, we fully exploited the redundant and complementary measurements of the particle kinematics performed by the various AMS sub-detectors, achieving for the looser(tighter) selection criteria a signal/background acceptance ratio of 10^2(10^5) up to ~ 100 GeV.

Convoluting the acceptances obtained with our analysis to the expected cosmic anti-proton, electron and proton fluxes, we obtained the rates for both the signal and the backgrounds that AMS is expected to observe in absence of DM signal, as well as the projected accuracy of the $\bar{\mathrm{p}}$ flux measurement in three years of data taking. AMS will determine the anti-proton spectrum wit a maximum error of 10% for momenta below ~ 100 GeV: this limit can be raised to ~ 500 GeV applying the looser selection criteria with a level of $2 \div 3\%$ of background.

Finally, we considered a set of proposed DM signals, corresponding to different SUSY breaking scenarios (AMSB, *Funnel* and NUGM), to evaluate the actual detection capability of the AMS experiment using a $\widetilde{\chi}^2$ concordance test.

The values of $\widetilde{\chi}^2$ we found applying our analysis are quite large for the first two hypotheses (AMSB, *Funnel*) and allow to cleanly identify the respective signatures in the cosmic anti-proton flux, as well as to distinguish between the two kinds of SUSY model. The signature significance for the third scenario (NUGM) is lower, however, the evaluated $\widetilde{\chi}^2$ sets a C.L. of $\sim 99.99\%$ anyway.

The concordance test was performed assuming a neutralino mass $m_\chi = 300$ GeV.

Our consideration was then extended to the cases of other neutralino masses using an approximate approach: it turns out that AMS should be able to discriminate the corresponding signals over a wide range of allowed neutralino masses, in particular for the case of the AMSB model the whole mass range $100 \div 600$ GeV is accessible. Even in the most unfavourable scenario (NUGM), the explored region corresponds to about the lower two thirds of the above mentioned range.

The quoted AMS sensitivity was evaluated assuming a specific theoretical prediction for the ordinary anti-proton flux: such estimates are generally affected by a variability of order 10% due to the large uncertainties of the currently available cosmic anti-proton flux measurements, so the actual AMS sensitivity may be slightly different, however, it should be noticed that AMS will actually perform a multi-channel search, probing the presence of DM signals in the cosmic spectra of other charged (e^+,$\bar{\mathrm{D}}$) as well as neutral species (γ).

The possibility to cross-check the results from all the measured spectra will significantly increase the overall DM detection potential of the AMS detector.

Acknowledgements

I would like to express my gratitude to the persons that gave me help in one way or another, contributing to the accomplishing of my PhD thesis work.

First of all I thank Prof. Roberto Battiston for the opportunity he gave me to undertake this interesting study, that represented for me a valuable source of intellectual growth as well as of personal satisfaction.

I am deeply indebted to all the members of the Perugia AMS group, who never hesitated to sacrifice their spare time to help me with clarifying discussions and friendship. In particular I want to thank my PhD tutors, Dott.sa Bruna Bertucci and Dott. Paolo Zuccon, who where my principal sources of stimulus and advice.

A special thought goes to my friend, Dott. Flavio Travasso, who shared with me the office and many ours of nightly work. I am grateful to him for the fruitful discussions on technical issues as well as for the infectious gaiety he retains whatever the circumstances.

Finally I want to thank the members of my family, who encouraged me with their affectionate encouragement, and my beloved Laura whose though never fails to give me joy.

Bibliography

[1] Albert Einstein. Cosmological Considerations in the General Theory of Relativity. *Sitzungsber. Preuss. Akad. Wiss. Berlin (Math. Phys.)*, 1917:142–152, 1917.

[2] H. P. Robertson. On the Foundations of Relativistic Cosmology. *Proc. Nat. Acad. Sci. (U.S.A.)*, 15(11):822–829, 1929.

[3] H. P. Robertson. Kinematics and World-Structure. *ApJ*, 82:284–+, nov 1935.

[4] A. G. Walker. On Milne's Theory of World-Structure. *Proc. London Math. Soc.*, 42:90–127, 1936.

[5] E. Hubble. A relation between distance and radial velocity among extra-galactic nebulae. *Proc. Nat. Acad. o Sci.*, 15(3):168, 1929.

[6] S. Eidelman et al. Review of Particle Physics. *Physics Letters B*, 592:1+, 2004.

[7] A. Friedmann. Über die Krümmung des Raumes. *Zeitschrifts für Physics*, 10:377–386, 1922.

[8] A. Friedmann. Über die Möglichkeit einer Welt mit kostanter negativer Krümmung des Raumes. *Zeitschrifts für Physics*, 21:326–332, 1924.

[9] G. Lemaitre. Un univers homogène de masse constante et de rayon croissant rendant compte de la vitesse radiale des nébuleuses extragalactiques. *Annnales de la Societé Scientifique de Bruxelles*, A47:49–59, 1927.

[10] Ralph A. Alpher and Robert C. Herman. Theory of the Origin and Relative Abundance Distribution of the Elements. *Rev. Mod. Phys.*, 22(2):153–212, apr 1950.

[11] Ralph A. Alpher and Robert C. Herman. Remarks on the Evolution of the Expanding Universe. *Phys. Rev.*, 75(7), apr 1949.

[12] Arno A. Penzias and Robert Woodrow Wilson. A measurement of excess antenna temperature at 4080-mc/s. *Astrophys. J.*, 142:419–421, 1965.

[13] Robert V. Wagoner, William A. Fowler, and Fred Hoyle. On the Synthesis of elements at very high temperatures. *Astrophys. J.*, 148:3–49, 1967.

[14] L. Kawano. Let's go: Early universe 2. Primordial nucleosynthesis the computer way. *NASA STI/Recon Technical Report N*, 92:25163–+, jan 1992.

[15] S. Esposito, G. Miele, S. Pastor, M. Peloso, and O. Pisanti. Non equilibrium spectra of degenerate relic neutrinos. *Nucl. Phys.*, B590:539–561, 2000.

[16] Scott Dodelson and Michael S. Turner. Nonequilibrium neutrino statistical mechanics in the expanding universe. *Phys. Rev.*, D46:3372–3387, 1992.

[17] David Seckel. Nucleon mass corrections to the p <—> n rates during Big Bang Nucleosynthesis. *hep-ph/9305311*, 1993.

[18] Keith A. Olive. Inflation. *Phys. Rept.*, 190:307–403, 1990.

[19] David H. Lyth and Antonio Riotto. Particle physics models of inflation and the cosmological density perturbation. *Phys. Rept.*, 314:1–146, 1999.

[20] R. K. Sachs and A. M. Wolfe. Perturbations of a cosmological model and angular variations of the microwave background. *Astrophys. J.*, 147:73–90, 1967.

[21] P. J. E. Peebles. *Principles of Physical Cosmology*. Princeton U.P., 1993.

[22] T. Padmanabhan. *Structure formation in the universe*. Cambridge U.P., 1993.

[23] F. Zwicky. Spectral displacement of extra galactic nebulae. *Helv. Phys. Acta*, 6:110, 1933.

[24] Rubin V.C. Ford W.K.Jr. Rotation of the Andromeda nebula from a spectroscopic survey of emission regions. *Astrophysical Journal (USA)*, 159(2):379–404, Feb. 1970.

[25] Rubin V.C. Thonnard N. Ford K.W.Jr. Extended rotation curves of high-luminosity spiral galaxies. I. the angle between the rotation axis of the nucleus and the outer disk of NGC 3672. *Astrophysical Journal Letters to the Editor (USA)*, 217(1):L1–4, Oct. 1977.

[26] Massimo Persic, Paolo Salucci, and Fulvio Stel. The Universal rotation curve of spiral galaxies: 1. The Dark matter connection. *Mon. Not. Roy. Astron. Soc.*, 281:27, 1996.

[27] Massimo Persic and Paolo Salucci. Rotation curves of 967 spiral galaxies. *astro-ph/9502091*, 1995.

[28] David M. Wittman, J. Anthony Tyson, David Kirkman, Ian Dell'Antonio, and Gary Bernstein. Detection of weak gravitational lensing distortions of distant galaxies by cosmic dark matter at large scales. *Nature*, 405:143–149, 5 2000.

[29] Y. Mellier. Cosmological applications of gravitational lensing. *astro-ph/9901116*, 1999.

[30] Alexei V. Filippenko. Evidence from Type Ia Supernovae for an Accelerating Universe and Dark Energy. *astro-ph/0307139*, 2003.

[31] 2dGFRS. 2-degree Field (2dF) Galaxy Redshift Survey. http://harris.roe.ac.uk/wjp/2dFGRS/2dF_intro.html.

[32] Will J. Percival et al. The 2dF Galaxy Redshift Survey: The power spectrum and the matter content of the Universe. *Mon. Not. Roy. Astron. Soc.*, 327:1297, 2001.

[33] P. J. E. Peebles and J. T. Yu. Primeval adiabatic perturbation in an expanding universe. *Astrophys. J.*, 162:815–836, 1970.

[34] Ya. B. Zeldovich and R. A. Sunyaev. The interaction of matter and radiation in a hot-model universe. *Astrophys. Space Sci.*, 4:301, 1969.

[35] E. Komatsu et al. First year wilkinson microwave anisotropy probe (wmap) observations: Tests of gaussianity. *Astrophys. J. Suppl.*, 148:119–134, 2003.

[36] Eric Gawiser and Joseph Silk. The cosmic microwave background radiation. *Phys. Rept.*, 333:245–267, 2000.

[37] G. F. Smoot et al. Structure in the cobe dmr first year maps. *Astrophys. J.*, 396:L1–L5, 1992.

[38] J. E. Ruhl et al. Improved measurement of the angular power spectrum of temperature anisotropy in the cmb from two new analyses of boomerang observations. *Astrophys. J.*, 599:786–805, 2003.

[39] A. T. Lee et al. A high spatial resolution analysis of the maxima-1 cosmic microwave background anisotropy data. *Astrophys. J.*, 561:L1–L6, 2001.

[40] A. Benoit et al. The cosmic microwave background anisotropy power spectrum measured by archeops. *Astron. Astrophys.*, 399:L19–L23, 2003.

[41] T. J. Pearson et al. The anisotropy of the microwave background to l = 3500: Mosaic observations with the cosmic background imager. *Astrophys. J.*, 591:556–574, 2003.

[42] Chao-lin Kuo et al. High resolution observations of the cmb power spectrum with acbar. *Astrophys. J.*, 600:32–51, 2004.

[43] N. W. Halverson et al. DASI first results: A measurement of the cosmic microwave background angular power spectrum. *Astrophys. J.*, 568:38–45, 2002.

[44] Robert A. Watson et al. First results from the very small array — i. observational methods. *Mon. Not. Roy. Astron. Soc.*, 341:1057, 2003.

[45] D. N. Spergel et al. First Year Wilkinson Microwave Anisotropy Probe (WMAP) Observations: Determination of Cosmological Parameters. *Astrophys. J. Suppl.*, 148:175, 2003.

[46] J. M. Lamarre et al. The planck high frequency instrument, a 3rd generation cmb experiment, and a full sky submillimeter survey. *astro-ph/0308075*, 2003.

[47] Keith A. Olive. Tasi lectures on dark matter. *astro-ph/0301505*, 2003.

[48] C. Alcock et al. First detection of a gravitational microlensing candidate towards the small magellanic cloud. *Astrophys. J.*, 491:L11, 1997.

[49] C. Renault et al. Observational limits on machos in the galactic halo. *astro-ph/9612102*, 1996.

[50] A. Udalski. Optical gravitational lensing experiment. the distance scale: Galactic bulge - lmc - smc. *Acta Astron.*, 48:113, 1998.

[51] C. Alcock et al. The macho project: Microlensing results from 5.7 years of lmc observations. *Astrophys. J.*, 542:281–307, 2000.

[52] B. J. Carr. Primordial black holes. Prepared for Workshop on Conference on the Future of Theoretical Physics and Cosmology in Honor of Steven Hawking's 60th Birthday, Cambridge, England, 7-10 Jan 2002.

[53] S. Fukuda et al. Tau neutrinos favored over sterile neutrinos in atmospheric muon neutrino oscillations. *Phys. Rev. Lett.*, 85:3999–4003, 2000.

[54] Q. R. Ahmad et al. Measurement of the charged current interactions produced by b-8 solar neutrinos at the sudbury neutrino observatory. *Phys. Rev. Lett.*, 87:071301, 2001.

[55] Aaron Pierce and Hitoshi Murayama. WMAPping out neutrino masses. *hep-ph/0302131*, 2003.

[56] R. D. Peccei and Helen R. Quinn. CP conservation in the presence of instantons. *Phys. Rev. Lett.*, 38:1440–1443, 1977.

[57] C. Hagmann et al. Results from a high-sensitivity search for cosmic axions. *Phys. Rev. Lett.*, 80:2043–2046, 1998.

[58] S. Asztalos et al. Large-scale microwave cavity search for dark-matter axions. *Phys. Rev.*, D64:092003, 2001.

[59] I. Ogawa, S. Matsuki, and K. Yamamoto. Interactions of cosmic axions with rydberg atoms in resonant cavities via the primakoff process. *Phys. Rev.*, D53:1740–1744, 1996.

[60] K. Yamamoto et al. The rydberg-atom-cavity axion search. *hep-ph/0101200*, 2000.

[61] E. W. Kolb and M.S. Turner. *The Early Universe*. Addison Wesley, 1990.

[62] Keith A. Olive. Introduction to supersymmetry: Astrophysical and phenomenological constraints. *hep-ph/9911307*, 1999.

[63] John R. Ellis, J. S. Hagelin, D. V. Nanopoulos, Keith A. Olive, and M. Srednicki. Supersymmetric relics from the big bang. *Nucl. Phys.*, B238:453–476, 1984.

[64] T. K. Hemmick et al. A search for anomalously heavy isotopes of low z nuclei. *Phys. Rev.*, D41:2074–2080, 1990.

[65] A. Bottino, F. Donato, N. Fornengo, and S. Scopel. Supersymmetric Dark Matter. *Nuclear Physics B (Proc. Suppl.)*, 113:50–59, 12 2002.

[66] B. Moore et al. Dark matter substructure in galactic halos. *astro-ph/9907411*, 1999.

[67] P. Belli et al. Extending the dama annual-modulation region by inclusion of the uncertainties in astrophysical velocities. *Phys. Rev.*, D61:023512, 2000.

[68] Angel Morales. Direct detection of wimps with conventional (non-cryogenic) detectors: Experimental review. *Nucl. Phys. Proc. Suppl.*, 114:39–57, 2003.

[69] R. Bernabei et al. Dark matter search. *Riv. Nuovo Cim.*, 26N1:1–73, 2003.

[70] Joseph Silk, Keith A. Olive, and Mark Srednicki. The photino, the sun, and high-energy neutrinos. *Phys. Rev. Lett.*, 55:257–259, 1985.

[71] N. J. T. Smith. Low energy particles from the universe. Prepared for 30th International Conference on High-Energy Physics (ICHEP 2000), Osaka, Japan, 27 Jul - 2 Aug 2000.

[72] S. Desai et al. Search for dark matter wimps using upward through-going muons in super-kamiokande. *hep-ex/0404025*, 2004.

[73] Lars Bergström. Non-baryonic dark matter: Observational evidence and detection methods. *Rept. Prog. Phys.*, 63(5):793, May 2000.

[74] Lars Bergström, Joakim Edsjö, and Piero Ullio. Spectral gamma-ray signatures of cosmological dark matter annihilations. *Phys. Rev. Lett.*, 87:251301, 2001.

[75] P. Sreekumar et al. Egret observations of the extragalactic gamma ray emission. *Astrophys. J.*, 494:523–534, 1998.

[76] Gary L. Godfrey. Gamma Large Area Silicon Telescope (GLAST). Presented at 2nd Workshop: Towards a Major Atmospheric Cerenkov Detector, Calgary, Canada, 17-18 Jul 1993.

[77] R. A. Ong et al. The VERITAS project. 2003.

[78] Fiorenza Donato, Nicolao Fornengo, and Pierre Salati. Antideuterons as a signature of supersymmetric dark matter. *Phys. Rev.*, D62:043003, 2000.

[79] M. S. Longair. Introduction to high energy astrophysics. Prepared for International School of Space Science: 2001 course on Astroparticle and Gamma Ray Physics in Space (ISSS 2001), L'Aquila, Italy, 30 Aug - 7 Sep 2001.

[80] G. Hartmann, D. Mueller, and T. Prince. High-energy cosmic ray electrons: A new measurement using transition radiation detectors. *Phys. Rev. Lett.*, 38:1368–1372, 1977.

[81] J. Nishimura et al. Emulsion chamber observations of primary cosmic ray electrons in the energy range 30-gev - 1000-gev. *Astrophys. J.*, 238:394–409, 1980.

[82] K. K. Tang. The energy spectrum of electrons and cosmic ray confinement: A new measurement and its interpretation. *Astrophys. J.*, 278:881–892, 1984.

[83] H. Wilczynski et al. Interpreting anomalous electron pairs as new particle decays. Prepared for 26th International Cosmic Ray Conference (ICRC 99), Salt Lake City, Utah, 17-25 Aug 1999.

[84] Stefano Profumo and Piero Ullio. The role of antimatter searches in the hunt for supersymmetric dark matter. *JCAP*, 0407:006, 2004.

[85] C. Grimani et al. Measurements of the absolute energy spectra of cosmic-ray positrons and electrons above 7 GeV. *Astron. & Astroph.*, 392:287–294, September 2002.

[86] M. A. DuVernois et al. Cosmic ray electrons and positrons from 1-gev to 100-gev: Measurements with heat and their interpretation. *Astrophys. J.*, 559:296–303, 2001.

[87] M. Boezio et al. The Cosmic-Ray Electron and Positron Spectra Measured at 1 AU during Solar Minimum Activity. *Astrophys. J.*, 532:635–666699, 2000.

[88] Edward A. Baltz and Joakim Edsjo. Positron propagation and fluxes from neutralino annihilation in the halo. *Phys. Rev.*, D59:023511, 1999.

[89] R. L. Golden et al. Measurement of the positron to electron ratio in the cosmic rays above 5-gev. *Astrophys. J.*, 457:L103–L106, 1996.

[90] S. W. Barwick et al. The energy spectra and relative abundances of electrons and positrons in the galactic cosmic radiation. *Astrophys. J.*, 498:779–789, 1998.

[91] S. W. Barwick et al. Measurements of the cosmic-ray positron fraction from 1-gev to 50-gev. *Astrophys. J.*, 482:L191–L194, 1997.

[92] Thomas Gaisser. *Cosmic Rays and Particle Phisics*. University Press, Cambridge, 1990.

[93] R. L. Golden et al. Evidence for the existence of cosmic ray anti-protons. *Phys. Rev. Lett.*, 43:1196–1199, 1979.

[94] N. D. and Romanov Bogomolov, E. A. and Lubyanaya, , and M. S. Stepanov, S. V. and Shulakova. A Stratospheric Magnetic Spectrometer Investigation of the Singly Charged Component Spectra and Composition of the Primary and Secondary Cosmic Radiation (talk). In *16th International Cosmic Ray Conference in Kyoto*, volume 1, pages 330–335, 1979.

[95] A. Buffington and S. M. Schindler. Recent cosmic ray anti-proton measurements and astrophysical implications. *Astrophys. J.*, 247:L105–L109, 1981.

[96] A. Buffington, S. M. Schindler, and C. R. Pennypacker. A measurement of the cosmic-ray antiproton flux and a search for antihelium. *Astrophys. J.*, 248:1179–1193, sep 1981.

[97] M. H. Salamon et al. Limits on the antiproton / proton ratio in the cosmic radiation from 100 mev to 1580 mev. *Astrophys. J.*, 349:78–90, 1990.

[98] S. P. Ahlen et al. New limit on the low-energy antiproton / proton ratio in the galactic cosmic radiation. *Phys. Rev. Lett.*, 61:145–148, 1988.

[99] R. E. Streitmatter et al. Experimental limit on low-energy anti-protons in the cosmic radiation. *AdSR*, 9:65–69, 1989.

[100] S.A. Stephens. Secondary production of antiprotons in cosmic radiation. *Astrophysics and Space Science*, 76(1):87–103, may 1981.

[101] F. Taccetti et al. The pamela silicon tracker. *Nuovo Cim.*, A112:153–158, 1999.

[102] R. Battiston. The alpha magnetic spectrometer for the search for dark matter and antimatter in space and its first flight on the shuttle. Prepared for 2nd International Conference on Dark Matter in Astro and Particle Physics (DARK98), Heidelberg, Germany, 20-25 Jul 1998.

[103] K. Yoshimura et al. Observation of cosmic ray anti-protons at energies below 500-mev. *Phys. Rev. Lett.*, 75:3792–3795, 1995.

[104] S. Orito et al. Precision measurement of cosmic-ray antiproton spectrum. *Phys. Rev. Lett.*, 84:1078–1081, 2000.

[105] Y. Asaoka et al. Measurements of cosmic-ray low-energy antiproton and proton spectra in a transient period of the solar field reversal. *Phys. Rev. Lett.*, 88:051101, 2002.

[106] M. Boezio et al. The cosmic-ray antiproton flux between 0.62-gev and 3.19- gev measured near solar minimum activity. *Astrophys. J.*, 487:415–423, 1997.

[107] M. Boezio et al. The cosmic-ray anti-proton flux between 3-gev and 49-gev. *Astrophys. J.*, 561:787–799, 2001.

[108] F.Donato et al. Antiprotons from Spallations of Cosmic Rays on Interstellar Matter. *The Astrophysical Journal*, 563(1):172–184, 2001.

[109] T. Sanuki et al. Precise measurement of cosmic-ray proton and helium spectra with the bess spectrometer. *Astrophys. J.*, 545:1135, 2000.

[110] Lars Bergström, Joakim Edsjö, and Piero Ullio. Cosmic antiprotons as a probe for supersymmetric dark matter? *Astrophys. J.*, 526(1):215–235, 1999.

[111] F. Donato, Nicolao Fornengo, D. Maurin, and P. Salati. Antiprotons in cosmic rays from neutralino annihilation. *Phys. Rev.*, D69:063501, 2004.

[112] F. Donato et al. Anti-protons from spallations of cosmic rays on interstellar matter. *Astrophys. J.*, 563:172–184, 2001.

[113] David Maurin et al. Galactic cosmic ray nuclei as a tool for astroparticle physics. 2002.

[114] T. Maeno et al. Successive measurements of cosmic-ray antiproton spectrum in a positive phase of the solar cycle. *Astropart. Phys.*, 16:121–128, 2001.

[115] M. Aguilar et al. The Alpha Magnetic Spectrometer (AMS) on the International Space Station. I: Results from the test flight on the space shuttle. *Phys. Rept.*, 366:331–405, 2002.

[116] John R. Ellis, K. Enqvist, D. V. Nanopoulos, and K. Tamvakis. Gaugino masses and grand unification. *Phys. Lett.*, B155:381, 1985.

[117] Utpal Chattopadhyay and D. P. Roy. Higgsino dark matter in a sugra model with nonuniversal gaugino masses. *Phys. Rev.*, D68:033010, 2003.

[118] Tony Gherghetta, Gian F. Giudice, and James D. Wells. Phenomenological consequences of supersymmetry with anomaly-induced masses. *Nucl. Phys.*, B559:27–47, 1999.

[119] Lisa Randall and Raman Sundrum. Out of this world supersymmetry breaking. *Nucl. Phys.*, B557:79–118, 1999.

[120] Torbjorn Sjostrand. `Pythia` 5.7 and `JETSET` 7.4: Physics and manual. 1995.

[121] P. Ruiz-Lapuente, A. Burkert, and R. Canal. Type ia supernova scenarios and the hubble sequence. *Astrophys. J.*, 447:L69, 1995.

[122] `Galprop` numerical package. http://www.mpe.mpg.de/ãws/propagate.html.

[123] L. J. Gleeson and W. I. Axford. *Astrophys. J.*, 149:L115, 1967.

[124] Ming-Huey A. Huang. Physics results from alpha magnetic spectrometer 1998 shuttle flight. 2001.

[125] B. Blau et al. The AMS02 superconducting magnet for astrophysical researches. *Grav. Cosmol. Suppl.*, 8N1:101–111, 2002.

[126] B. Blau et al. The superconducting magnet system of AMS-02 - a particle physics detector to be operated on the international space station. *IEEE Trans. Appl. Supercond.*, 12:349, 2002.

[127] A. Nekano, D. Petrac, and C. Paine. He II liquid/vapour phase separator for large dynamic range operation. *Cryogenics*, 36:823–827.

[128] I. Frank and V. Ginzburg. *J. Phys.*, 9:353.

[129] Performance of the AMS-02 Transition Radiation Detector. to be submitted to NIM A.

[130] D. Alvisi et al. A high resolution, low power time-of-flight system for the space experiment AMS. *Nucl. Instrum. Meth.*, A437:212–221, 1999.

[131] D. Casadei. Design and test results of the AMS RICH detector. *Nucl. Phys. Proc. Suppl.*, 125:303–307, 2003.

[132] M. Buenerd. The RICH counter of the AMS experiment. *Nucl. Instrum. Meth.*, A502:158–162, 2003.

[133] C Delgado. The AMS-RICH prototype: Test beam results. AMS Internal Note, 09 2003. Available at: http://ams.cern.ch/AMS/Reports/AMSnotes2003-/AMSnote-2003_08_03.ps.

[134] F. Cervelli et al. A reduced scale e.m. calorimeter prototype for the AMS-02 experiment. *Nucl. Instrum. Meth.*, A490:132–139, 2002.

[135] F. Cadoux et al. The AMS-02 electromagnetic calorimeter. *Nucl. Phys. Proc. Suppl.*, 113:159–165, 2002.

[136] R. Battiston. A silicon tracker for the antimatter spectrometer on the international space station alpha. *Nucl. Phys. Proc. Suppl.*, 44:274–281, 1995.

[137] J. Alcaraz et al. A silicon microstrip tracker in space: Experience with the AMS silicon tracker on sts-91. *Nuovo Cim.*, 112A:1325–1343, 1999.

[138] W. J. Burger. The AMS silicon tracker. *Nucl. Phys. Proc. Suppl.*, 113:139–146, 2002.

[139] M. Acciarri et al. The l3 silicon microvertex detector. *Nucl. Instrum. Meth.*, A351:300–312, 1994.

[140] G. F. Dalla Betta et al. Feasibility study for double-sided silicon microstrip detector fabrication at irst. *Nucl. Instrum. Meth.*, A431:83–91, 1999.

[141] O. Toker, S. Masciocchi, E. Nygard, A. Rudge, and P. Weilhammer. Viking: A cmos low noise monolithic 128-channel front end for si strip detector readout. *Nucl. Instrum. Meth.*, A340:572–579, 1994.

[142] R.Brun et al. GEANT 3. CERN DD / EE / 84-1 revised 87.

[143] R. Brun and F. Rademakers. ROOT: An object oriented data analysis framework. *Nucl. Instrum. Meth.*, A389:81–86, 1997. Proceedings AIHENP'96 Workshop, Lausanne, Sep. 1996. See also http: / / root.cern.ch / .

[144] E. Choumilov. Mc simulation of AMS02 level–1 trigger. AMS02 internal report, 28 2001.

[145] V. Choutko. AMS02 Charged Particles LVL1 Trigger Simulation. Presentation at AMS TIM, 9 2002. Available at: http: / / ams.cern.ch / AMS / Analysis / hpl3itp1- / ams02_lvl1.ps.

[146] V. Choutko. Selected AMS Reconstruction Software Issues. Presentation at AMS TIM, 01 2003. Available at: http: / / ams.cern.ch / AMS / Analysis- / hpl3itp1 / ams_rec_sel.ps.

[147] V. Innocente, M. Maire, and E. Nagy. Geane: Average tracking and error propagation package. In *Amsterdam 1991, Proceedings, MC91: Detector and event simulation in high energy physics* 58-78. (see HIGH ENERGY PHYSICS INDEX 30 (1992) No. 3237).

[148] J. Alcaraz. The alternative track fitting method for AMS. AMS Internal Note, 03 2003. Available at: http: / / ams.cern.ch / AMS / Analysis- / hpl3itp1 / ams_rec_sel.ps.

[149] J. Alcaraz et al. Cosmic protons. *Phys. Lett.*, B490:27–35, 2000.

[150] J. Alcaraz et al. Leptons in near Earth orbit. *Phys. Lett.*, B484:10–22, 2000.

[151] G. Cowan. A survey of unfolding methods for particle physics. Prepared for Conference on Advanced Statistical Techniques in Particle Physics, Durham, England, 18-22 Mar 2002.

[152] Volker Blobel. An unfolding method for high energy physics experiments. 2002.

[153] G. D'Agostini. A multidimensional unfolding method based on bayes' theorem. *Nucl. Instrum. Meth.*, A362:487–498, 1995.